Geometric and Plasmonic Effects in Radiative Heat Transfer

by

Audrey-Rose Gutierrez

A dissertation submitted in partial fulfillment
of the requirements for the degree of
Doctor of Philosophy
(Electrical and Computer Engineering)
in the University of Michigan
2024

Doctoral Committee:

Professor Pramod Sangi-Reddy, Chair
Professor Parag Deotare
Professor Edgar Meyhöfer
Professor Zhaohui Zhong

AudreyRose M Gutierrez

audreyro@umich.edu

ORCID iD: 0000-0001-6671-7109

Dedication

To my spouse.

Carlos: I do not know how long it will take me to pursue this knowledge, but I do know two things.

Cecil: What is that?

Carlos: I love you.

Cecil: I love you, too. What's the other thing?

Carlos: You just said it.

Welcome to Nightvale, Joseph Fink and Jeffery Cranor

Acknowledgements

I am grateful to my co-advisors Pramod Reddy and Edgar Meyhöfer, for taking in a senior graduate student in need of a new research group and supporting me in my development as a scientist. It is refreshing to find PI's who are so actively involved in the lab work in their group, and who can bring the best out of their students so well. Thank you for encouraging and helping me as I took on a new research area; I learned so much in our time working together.

Many thanks also to Zhaohui Zhong. You gave me the best start in research that any student could hope for. I will always remember leaving our meetings with a refreshed passion for our projects together, and I carry that persistent optimism to this day. To my committee member, Professor Parag Deotare, thank you for kindly lending your advice on such short notice. While we did not have a collaboration history together, I was honored to have the support of someone whose research work I have followed.

I owe much to the collaborators in my lab, who aided in many essential pieces of the research work and broadened my understanding of mechanical engineering fundamentals and computations. For this, I thank Zhongyong Wang, Ju Won Lim, Rohith Mittapally, Yuxuan Luan, Ayan Majumder, and Kanishka Panda. Thank you also to Gabriel Jaffe, who has contributed greatly in conversation without direct collaboration. From my previous lab, I would not be so comfortable in working with two-dimensional materials without the mentorship of Minmin Zhou and Wenzhe Zang. I am grateful also to the kind and supportive peer mentorship I always enjoyed from Dehui Zhang and Zhe Liu; I so greatly enjoyed our time together.

This work would also have been impossible without the support of previous and current members of the Lurie Nanofabrication Facility staff. I would like to especially thank Pilar Herrera-Fiero, who helped me to find my current research group, and Sandrine Martin, who has cultivated such a supportive community here. A special thanks to Rob Hower, who taught me so much in my first year of microfabrication. Many thanks also Tony Sebastian, Nadine Wang, Brian Armstrong, Matt Oonk, Rob Nidetz, Vishva Ray, Katherine Beach, and Jorge Barrera, not only their good work but also for pausing for a quick chat and a kind word so often. You all make the LNF feel like such a nice place to do work. I hope that Kevin, Michelle, Shawn, and Casey all already know how much I appreciate not only working together but also knowing you as friends. Itzayana, you will always be my favorite staff member, but it isn't a fair competition.

I was incredibly fortunate to begin my PhD journey with an amazing cohort, and to continue to meet kind and supportive people along the way. Thank you to Zumrad, Chris, Baran, and later Kishwar for the lunchtime support and so many study sessions together. You all made those first years so much better. Thank you also to Tanya, Nate, Marion, and Ben, for being friends with me in these last few years. I never imagined that I would get to know such great people with the amount of time I had left here. To Hannah, by your dad's rules you must have earned a second PhD just by the amount of discussion we've had for mine. Few people in this world are so fortunate as to have an incredible friend like you, thank you.

To my family, who have always valued education and encouraged me in my pursuit of science, thank you. I would like to especially thank my parents, Patrick and Andrea, for believing in me when I did not. And finally, to my greatest supporter, thank you Itzy. An excellent writer could tell you how much you mean to me. I can only try to do for you as you have done for me, knowing and loving that it may take a lifetime.

Table of Contents

List of Tables

List of Figures

Abstract

Radiative heat transfer rates between a hot and a cold body can experience a significant increase when the distance between the objects is well below the Wien's wavelength (~10 μm at 300 K). Recent advancements in nanofabrication have expanded the possibilities for exploring radiative heat transfer in nanoscale gaps towards real-world applications of near-field radiative heat transfer (NFRHT). Until now, studies on NFRHT have primarily concentrated on nanoscale gap measurements between two plane parallel surfaces or between a sphere and a plane. However, practical applications may necessitate the consideration of different designs, including curved surfaces. Further, it is also important to understand how NFRHT can be dynamically modulated using external stimuli such as electric fields.

This dissertation presents an experiment that systematically explores NFRHT between two spherical surfaces. To perform the desired experiments, smooth silica spheres (~40 μm diameter) were integrated into custom-fabricated calorimetric probes to create a "receiver" device. Further, a second "emitter" device was also created, a planar silicon device onto which a smooth silica sphere was integrated.

NFRHT between the two silica spheres was probed by integrating the emitter and receiver devices into a custom-built nanopositioner that enables both relative alignment of the two spheres as well as control of the gap size between them. In a first series of studies reported in Chapter 3 of this dissertation heat flow between the two spheres was measured when the Si surface was heated by ~10-30 K above the ambient temperature and the gap size between the

spheres was systematically reduced from ~5 μm to 10s of nm. During this process a significant enhancement in radiative heat transfer was observed, increasing ~15-times. The peak measured thermal conductance, at the minimum gap size (80 nm),was 3.82 nW/K. This measured value is approximately two orders of magnitude lower than the predicted value for plate-plate heat transfer between two circular silica plates with a diameter of 40 μm, and about half of what was measured for heat transfer using the same receiver sphere and an effectively infinite silica plate. The measured, lower sphere-sphere near-field thermal conductances are expected and in excellent agreement with numerical simulations performed using fluctuational electrodynamics.

In addition to the work described above, this dissertation explores if NFRHT can be actively controlled by electrostatically tuning the dielectric properties of a material (Chapter 4 of the dissertation). Specifically, experiments were performed to explore if graphene could be employed for tuning NFRHT. Towards this goal, an experiment was designed by combining the calorimetric probe described above with a planar, three-terminal graphene device, with back gate-tunable dielectric properties. These experiments characterized NFRHT between the sphere embedded in the calorimetric probe and the planar sample as a function of the applied gate voltage. Upon sweeping the back gate voltage, these preliminary experiments revealed a distinct, nanowatt-scale increase in the radiative thermal conductance. While these preliminary results are promising for tuning NFRHT, additional experiments showing a decrease with opposite back gate tuning are required to confirm these findings, as the current observations are potentially confounded by the increased capacitive force on the probe.

Finally, I conclude the dissertation by describing possible approaches for mitigating some of the challenges encountered in this work and opportunities for future work.

Chapter 1 Geometric and Plasmonic Effects on NFRHT

1.1 Sources of Propagating and Evanescent Radiation from a Hot Body

Temperature is a measure of the average kinetic energy of the atoms comprising a system. For all atomic matter above 0 K, this energy represents the thermally driven motion of the atoms within the material. These excitations of matter are described via quasiparticles such as plasmons and phonons, which represent quantized excitations of the free electrons and the lattice, respectively[1]. On a microscopic level, the motion of atoms in a solid is confined by its bonds (ionic or covalent).

The random fluctuations of ions and charges provide an intuitive picture of the origin of thermal emissions that comprise of the spectrum of a blackbody. Specifically, these fluctuation charges represent charges in acceleration that lead to electromagnetic emissions as expected from classical electromagnetism[2]. We would also be correct to deduce that, as this radiative emission results from thermal motion, the object is cooled as photons are emitted. When two objects are at the same temperature, there can be no net exchange of heat, however, a heated body can cool as it transfers heat to a cooler body via radiative heat transfer.

A comprehensive quantitative description of the energy density and spectral characteristics of blackbody emission came about when Max Planck built upon the classical approach employed in deriving the Rayleigh-Jeans expression for blackbody spectrum, which was known to fail in describing the blackbody spectrum for high energy photons [3]. In his derivation, Planck made the radical assumption that that the electromagnetic field can be treated

as a collection of harmonic oscillators who energies are quantized[4]. This leap to a new vision for the behavior of light, produced a quantitative expression for the spectral energy density ($u(v)$) of the blackbody radiation:

$$u(v) = \frac{8\pi}{c^3}\frac{hv^3}{\exp\left(\frac{hv}{k_B T}\right)-1} \quad \text{Eq. 1}$$

Where h is Planck's constant, v is the frequency of light, c is the speed of light, and k_B is Boltzmann's constant. As a consequence of the above law, one can show that the maximum heat transfer flux (Q) between a hot body blackbody at temperature T_{H} and a cold blackbody at temperature T_{C} is given by the blackbody limit (q_{BB}):

$$q_{BB} = \sigma(T_H^4 - T_C^4) \quad \text{Eq.2}$$

This above expression captures the heat transfer associated with the propagating modes of thermal radiation as the cavity considered in obtaining the analytical expression for $u(v)$ is macroscopic in dimension (i.e., the size of the cavity is much larger than the characteristic thermal wavelength called the Wien's wavelength, which is ~10 μm at room temperature) and the gap size between the blackbodies is assumed to be large (i.e., orders of magnitude larger than the wavelength of thermal photons). Therefore, the effects of surface modes (e.g., surface plasmons or surface phonon polaritons) and evanescent modes is not considered in the analysis performed in obtaining $u(v)$. It should also be noted that the expression for $u(v)$ and q_{BB} is likely inadequate when the sizes of the objects[5] or the gap size between the objects becomes comparable to the wavelength of thermal radiation. It is in one or both of these situations that we may anticipate radiative heat transfer beyond the Planck's Law prediction, called super-Planckian heat transfer.

1.2 Studies in Super-Planckian Radiative Heat Transfer

When a system is cooled to cryogenic temperatures, the necessary distance to achieve a cavity smaller than the Wien's wavelength becomes much larger. Using this relaxed condition, heat transfer rates exceeding the blackbody limit was first demonstrated a few decades ago[6]. Further, it was correctly postulated that this excess heat transfer may be caused by contributions from evanescent waves to radiative heat transfer.

In 1953, Rytov[7] constructed a general framework of fluctuational electrodynamics that can correctly describe near-field thermal radiation by combining Maxwell's equations and the fluctuation-dissipation theorem (FDT)[8]. The FDT was an essential component as it proved both for classical and quantum mechanical systems that there is a predictable relationship between thermodynamic fluctuations and impedance. Subsequently, Polder and van Hove successfully composed a full description[9] of near-field radiative heat transfer (NFRHT) in 1971. They began with the fluctuational electrodynamics formalism that was developed by Rytov but chose as the source term stochastic currents caused by the random thermal motion of atoms and consequent dipoles. In their study, they considered two parallel semi-infinite bodies separated by a vacuum gap of varying distance. Chromium was used as a specific example, but their formalism is applicable to all isotropic and nonmagnetic media. Their key result, i.e., the heat flux (q) between two half spaces of the same material can be expressed as[10]:

$$q(T_h, T_c, d) = \int_0^\infty \frac{d\omega}{4\pi^2} [\Theta(\omega, T_h) - \Theta(\omega, T_c) \int_0^\infty dkk[\tau_s(\omega, k) + \tau_p(\omega, k)] \quad \text{Eq. 3}$$

Where $\Theta(\omega, T) = \frac{h\omega}{\exp\left(\frac{h\omega}{k_B T}\right)-1}$ is the average energy of an oscillating dipole and provides the rapidly decreasing component at higher frequencies. T_h and T_c are the temperatures of the hot and cold body, respectively. Commonly a small temperature differential (~1 K) is used to predict

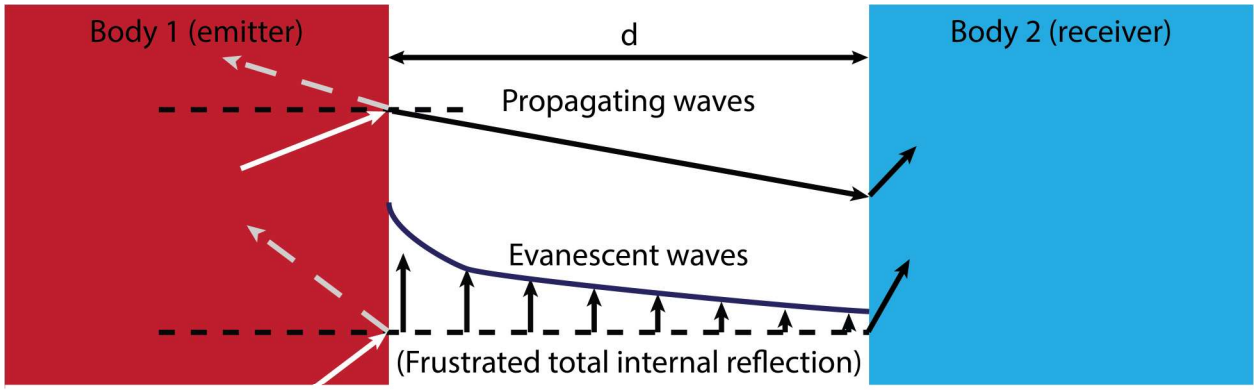

Figure 1: Two half-spaces with a vacuum gap of width *d* between them.

the thermal conductance using the above stated expression, however, care should be used when extrapolating this result to high temperature differentials, as the heated body may have non-negligible changes in dielectric function with significant changes in temperature. τ_s and τ_p are the transmission probabilities for s (TE) and p (TM) modes and will be considered further below. k is the wavevector parallel to the plane and must be doubly integrated as there are two vector components within the plane which can be arbitrarily chosen for full consideration.

A depiction of the model for the following discussion is in Figure 1. The analytical expressions for τ_s and τ_p for two half spaces (labelled body 1 and body 2, separated by a vacuum gap of size *d*) are given below. Note that expressions for the transmission coefficients are different for propagating and evanescent waves and are given by[11]:

$$\tau_{\alpha=s,p}^{12} = \frac{\left(1-|r_\alpha^{01}|^2\right)\left(1-|r_\alpha^{02}|^2\right)}{|D_\alpha|^2}, \text{ if } k \leq \frac{\omega}{c} \rightarrow \text{propagating waves} \qquad \text{Eq. 4}$$

$$\tau_{\alpha=s,p}^{12} = \frac{4Im\{r_\alpha^{01}\}Im\{r_\alpha^{02}\}e^{-2Im\{k_{z2}\}d}}{|D_\alpha|^2}, \text{ if } k > \frac{\omega}{c} \rightarrow \text{evanescent waves.} \qquad \text{Eq. 5}$$

Here, the vacuum space is indicated by the subscript 0, with either half-space being 1 or 2. τ_α^{12} represents the transmission probability for s or p waves, depending on whether the chosen Fresnel reflection coefficient (r_α) corresponds to that of s or p waves as listed below in Eqs. 8

and 9, between body 1 and body 2 across the vacuum gap. Further, r_α^{ij} is the vacuum coefficient between media i and j, for s or p waves. k_z is the perpendicular component of the wavevector, $k_z = \sqrt{\epsilon_i(\omega) \cdot \frac{\omega^2}{c^2} - k^2}$. $D_\alpha = 1 - r_\alpha^{01} r_\alpha^{02} e^{i2k_{z2}d}$ and is called the Fabry-Pérot-like denominator due to its similarity in form and function to the denominator derived for transmission of light in a Fabry-Pérot cavity[12]:

$\frac{E_{trans}}{E_{inc}} = \frac{-t_\alpha^{01} t_\alpha^{02} e^{-i\phi}}{1 - r_\alpha^{01} r_\alpha^{02} e^{-i2\phi}}$, where ϕ is the incident angle and *t* is the transmission coefficient at that boundary.

For circumstances in which the two bodies are planar but cannot be described with two half-spaces, but rather must be considered as layered objects, a recursive calculation can be considered for each body to compose its total reflection coefficient, R_α^{0j}, for replacement of the original r_α^{0j}. As an example, for an object with 3 layers, beginning with *i* as the vacuum gap[13]:

$$r_{il} = \frac{r_{ij} + r_{jl} e^{2ik_{zj}t_j}}{1 - r_{ij} r_{lj} e^{2ik_{zj}t_j}}, \text{ where } \begin{matrix} j = i + 1 \\ l = i + 2 \end{matrix} \quad \text{Eq. 6}$$

$$r_{im} = \frac{r_{il} + r_{lm} e^{2ik_{zl}t_l}}{1 - r_{il} r_{ml} e^{2ik_{zl}t_l}}, \text{where } m = i + 3. \quad \text{Eq.7}$$

The reflection coefficients are different for s and p-polarized light, and are calculated as[11]:

$$s: r_{ij} = \frac{k_{zi} - k_{zj}}{k_{zi} + k_{zj}} \quad \text{Eq. 8}$$

$$p: r_{ij} = \frac{k_{zi} * \epsilon_j - k_{zj} \cdot \epsilon_i}{k_{zi} * \epsilon_j + k_{zj} \cdot \epsilon_i} \quad \text{Eq. 9}$$

ϵ is the dielectric function for the layer signified by the subscript. This method was used to calculate the predicted NFRHT between a silica and gold object, with varying thicknesses of silica deposited on top of the gold[11]. Predictions of NFRHT between two bulk bodies of SiO_2 and Au from reference [14] are shown in Figure 2.

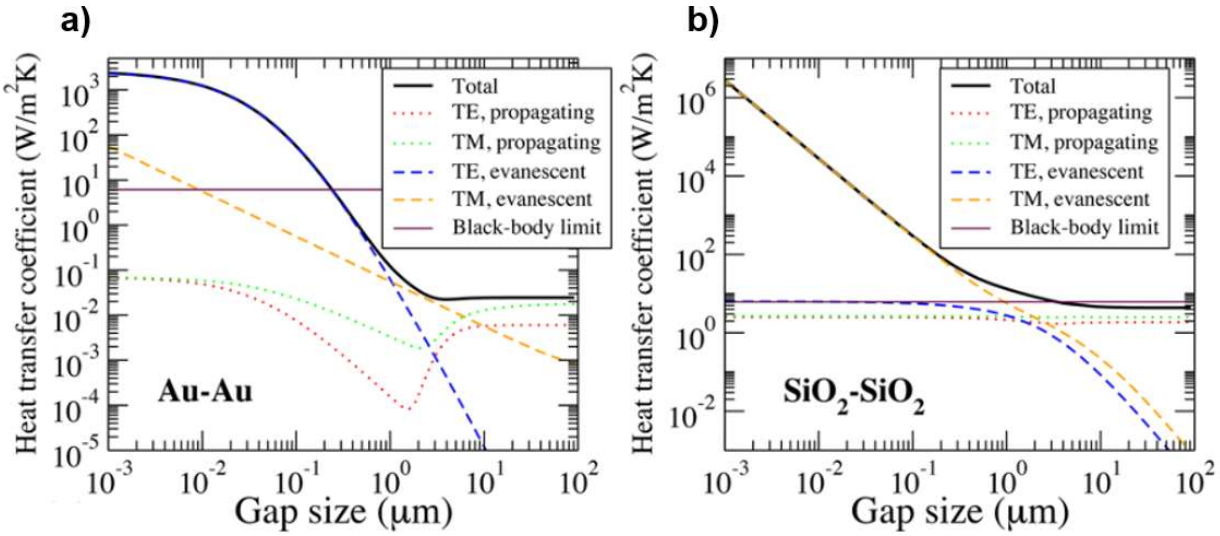

Figure 2: Bulk material dependence of NFRHT, copied with permission from reference 14.
Predictions of NFRHT between two bulk bodies of gold (a) and silicon dioxide (b).

The two most critical predictions from this analysis concern the distance dependence of the radiative heat transfer and the dominance of different radiation types in distinct distance regimes. At distances below the Wien peak wavelength, heat transfer increases by orders of magnitude, a phenomenon dominated by evanescent transverse magnetic (TM) waves rather than propagating waves. In materials such as gold, in which the heat transfer is dominated by evanescent transverse electric (TE) waves, the heat transfer levels off in the nanometric regime as proven in experimental results later[15]. Figure 3 shows results from an experimental study of two-plane silicon dioxide compared with this prediction, taken myself on our own nanopositioner setup. The prediction is also my own work.

A recent surge of investigation into NFRHT can be attributed in part to the formalism developed by Rytov and in part to an increasing understanding of the possible applications of the technology. Modern fabrication techniques also enable extremely clean and planarized surfaces to facilitate exploring this effect at lower distances at room temperature and higher. This may yield interesting results for a variety of applications. Potential applications of NFRHT include near-field thermophotovoltaics for renewable energy storage[16–19], heat flux modulation for thermal transistors[20], and the modeling and management of heat transfer in devices with nanoscale spacing that are already in use, such as transistors on chips[21,22].

1.3 Geometric Effects in NFRHT

While the semi-analytical expression for two parallel planar bodies discussed above is useful for analyzing material relationships in NFRHT, it represents a very small segment of real-world

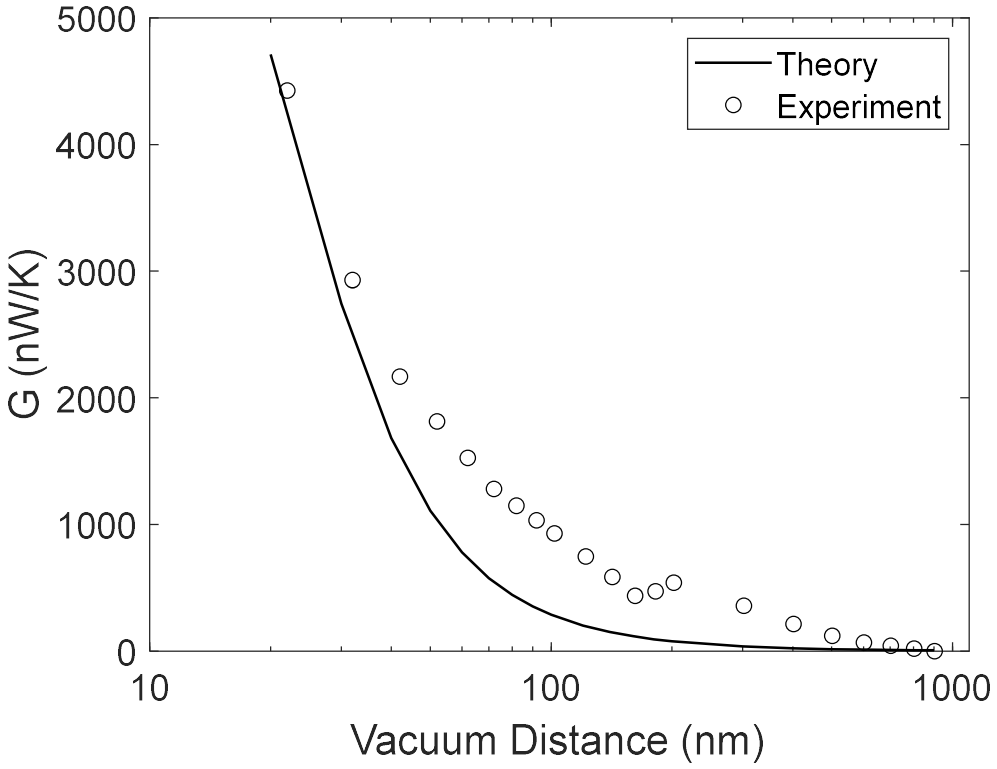

Figure 3: Green's function formalism prediction of NFRHT for two silica half-spaces with experimental result for two 2 μm SiO_2/Si samples.

geometries. Experiments with two planes require strict parallelization for accuracy which adds complexity, and a higher stiffness of the measurement devices is needed for planar geometries to avoid premature snap-in due to an increase in the area-dependent Casimir force. A variety of computational techniques have been proposed for the prediction of NFRHT for configurations in which one or both of the bodies are not planar[23–31].

Thus far, experiments in non-planar geometric configurations are somewhat limited in variety, making comparison with predictions more difficult. The majority of non-planar experimental studies consists of sphere-plane[11,32–36] and tip-plane[37–44] configurations. An experiment between two highly-curved surfaces would be useful for comparison with computational techniques designed for arbitrary surfaces and the specific use case.

We have chosen for such an experiment to use two spheres, and in doing so seek to provide experimental data for comparisons with predictions for both two-sphere geometries and arbitrary geometries. The choice of size is also significant, as a previous predictions has shown high agreement between their computational result and the dipole approximation, when sphere radii are quite small compared with the vacuum gap distance, and the proximity-force approximation, when sphere radii are large compared with the vacuum gap distance[28].

Therefore, spheres that may be most difficult to compute without approximation have radii similar to the largest expected gap distance of 10 μm. To that end, two spheres of radii ~20 μm were chosen, which was anticipated to satisfy the desired range, while still being large enough to obtain an accurate, surface-area dependent, heat flux measurement.

1.4 Two-Dimensional Materials and Plasmonics in NFRHT

In a work by Lang Zhang and Owen Miller, both real and idealized examples of material types are considered for reaching the limits of near field radiative heat transfer. An ideal 2D plasmonic material with a single, low frequency conductivity pole and a tunable carrier concentration is the optimal material for all distances examined[45], potentially representing a realistic limit for practical heat transfer materials. Graphene is compared at a fixed Fermi level of 0.4eV and is the closest material studied to meeting this limit (Figure 4).

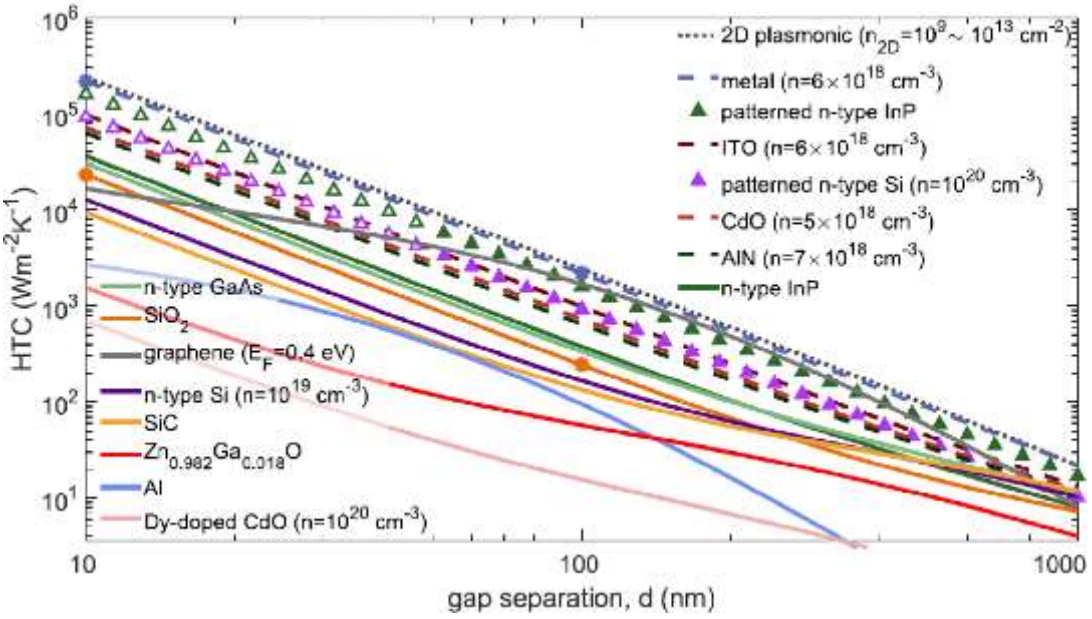

Figure 4: Physical limits of NFRHT. Figure and caption excerpt copied with permission from reference 27. HTC values at 300 K of the plane−plane configuration at different gap separations d for ideal bulk materials (dashed lines) and 2D materials (dotted lines), materials with experimentally measured permittivity or conductivity data available (solid lines), and materials with periodic-cylindrical-hole patterning (triangles). Optimal 2D conductivities range from n_{2D} =9e9 cm^{-2} for d =10 nm to n_{2D} =9e13 cm^{-2} for d = 1000 nm, assuming linear Dirac electronic dispersion, as exhibited by graphene. We note that graphene exhibits the highest predicted HTC of any real material near 100 nm and may be improved at other distances by Fermi level tuning and/or patterning.

In addition to potentially high peak NFRHT, two-dimensional material systems are predicted to exhibit high tunability through controlling a range of external mechanisms: mechanical, magnetic, and electric-field[29,46–54]. In the field of NFRHT with layered hyperbolic materials for anisotropic heat transfer, two-dimensional materials offer atomic-level distinction

between layers[55]. Additionally, two-dimensional materials can be used to facilitate heat transfer between dissimilar materials and enhance the total NFRHT beyond either material alone[52,56]. Despite the many hopeful predictions of two-dimensional material applications in NFRHT, there are few experimental studies available[57–61].

Towards closing this knowledge gap, we have conducted an experiment investigating the electric-field tunability of a sphere-plane silicon dioxide system mediated on one side by graphene. We have chosen this system to explore the realistic ability of graphene to significantly alter the NFRHT between two polar materials, using plasmonic tuning via a backgate.

1.5 Structure of This Dissertation

For a complete understanding of super-Planckian heat transfer, experimental investigations must be conducted on a diverse range of materials and geometries. To date, the majority of NFRHT studies have focused on tip-plane[37–44], sphere-plane[11,32–36] and plane-plane[21,62–64] geometries. There is not, to our knowledge, an existing experimental study between two curved surfaces. Additionally, despite promising attributes for tunable NFRHT[29,46–54], facilitating heat transfer between dissimilar materials[52,56], and potentially NFRHT approaching the physical limitations[45], existing studies on two-dimensional material systems are limited in scope[57–61].

For both of the experiments explored, a vertical configuration of the probe tip used for measuring heat transfer was needed. For the two-sphere configuration, this allowed optimal alignment of the spheres, and in the graphene-SiO_2 experiment, a highly sensitive probe was needed without sacrificing stiffness, and the vertical configuration served to largely circumvent that tradeoff.

In this thesis, I will begin by discussing the experimental and data analysis techniques used in both studies to enable acquisition of these results in Chapter 2. Next, I will discuss the

first experimental study of NFRHT between two spheres as a foray into thermal transfer between two curved surfaces in Chapter 3. In Chapter 4 I will discuss the first experimental investigation of graphene as a tunable mediator of NFRHT between two silica bodies for a range of distances and levels of electrical doping. Finally, in Chapter 5, I will summarize these conclusions and consider potential future works based on these findings.

Chapter 2 Novel Experimental Scheme to Probe NFRHT in the Sphere-Sphere and Sphere-Plane Configuration

2.1 Introduction

Probing NFRHT requires the development of novel experimental approaches as it is necessary to measure small heat fluxes while maintaining nanoscale gaps. In fact, measurement configurations in the sphere-plane configuration need enhanced sensitivity to heat flows as the fact that the near-field thermal conductance for a sphere-plane configuration is smaller than that in the plane-plane configuration[11]. This decrease in conductance is due to the reduced surface area of the hot and cold bodies that are within the near field distance. This introduces a need for high-resolution in our sensing device. An additional constraint is that high-stiffness is required for both experiments described to enable the minimum gap for final contact. Casimir forces increase exponentially at 10s of nanometer-scale gaps and can cause a phenomenon called "snap-in"[65]. This occurs when Casimir forces overcome the stiffness of a compliant device, bending it to close the gap prematurely. For the graphene-mediated experiment, an additional strong attractive force exists due to the back gate voltage tuning. This mismatch of voltage between the emitter and the receiver contributes to capacitive forces between the two devices.

Due to these needs, a measurement scheme was needed that was both sensitive to nanowatt-scale temperature changes in the receiver body and low-compliance mechanically for both devices. A vertical alignment for the probe was chosen to eliminate the tradeoff between thin and thus low thermal conductance probe beams, ideal for high sensitivity, and the decrease

in stiffness caused by this thinning. This alignment configuration introduced additional design decisions, as we worked to prototype strong electrical connections around a 90° angle.

Additionally, limitations on the travel of the coarse Z stage in the nanopositioner used and the working distance of the microscope objective used led to size restrictions. A full view of the receiver sphere was also necessary for accurate alignment of the two-sphere experiment. This chapter explains the choice of critical parameters for these measurements, including the heating and sensing scheme (2.2),the receiver and emitter details (2.3), and the calculation of the radiative heat transfer versus distance from the raw data gathered (2.4).

2.2 Heating and Sensing Scheme

In most basic terms, for a radiative heat transfer measurement, there must be a heater to generate a hot body (emitter), and there must be a sensor to register temperature changes as heat flows to the cold body (receiver). This sensor can be placed on the emitter to measure cooling or on the receiver to measure heating. It is imperative to know the total heat applied to the heated body for calculation of the differential and to maintain a constant temperature on the cold body for consistency.

In our experiments, the device opposite the calorimetric probe consists of a large thermal mass with significant thermal conductance and is therefore not ideal for sensing small temperature changes. In our first attempt, the calorimetric probe was used as both a heater and a sensor, but we determined that this was not best for accurate sensing (2.2.2). A modified approach, utilizing the probe as the sensor and the large-area device as the emitter, is discussed in 2.2.3.

2.2.1 Schemes for heating and sensing

General relations that hold true for different schemes at temperatures near room temperature are the following:

$$Q = I_Q^2 \cdot R_Q \quad \text{Eq. 10}$$

$$T_{tot} = \frac{\Delta Q}{G} \quad \text{Eq. 11}$$

$$\Delta V = I_s \cdot \alpha \cdot R_0 \cdot \Delta T_{tot} \quad \text{Eq. 12}$$

Where Q is the heat flux into the emitter by resistive heating. I_Q is the current causing heating, and R_Q is the heating resistor. I_s is the current input to the sensing device, and $R_0$is the room temperature resistance of the platinum thermistor. T_{tot} is the total change in temperature and G is the thermal conductance. ΔV is the voltage change on the lock-in, which can select for multiples of an input AC frequency. α is the temperature coefficient of resistance.

2.2.2 Previously used scheme

It was not considered feasible to suspend the bottom device with an embedded thermistor due to the unnecessary difficulty of attaching the sphere or transferring and patterning graphene to a small area. The first attempted measurement set used the top device as the emitter (DC heating) and the AC sensing instrument allowing an unsuspended bottom device to be held at room temperature without sensing. This can be done well for devices that have separate heating and sensing elements, but the results (not shown) were low for a sphere-plane measurement using AC sensing with a DC offset. We calculated the relationship between the voltage and the input current and recognized that measurement of the heating is not straightforward. For this example, $I_{tot} = I_Q = I_s \; and \; R_0 = R_Q$:

$$I_{tot} = I_{DC} + I_f \sin(\omega t) \quad \text{Eq. 13}$$

$$\Delta V = I_{tot} \cdot \alpha \cdot R_0 \cdot \Delta T_{tot} = I_{tot}^3 \cdot \alpha \cdot \frac{R_0^2}{G} \quad \text{Eq. 14}$$

$$I_{tot}^3 = I_{DC}^3 + 2I_{DC}^2 I_f \sin(\omega t) + 2I_{DC} I_f^2 \sin^2(\omega t) + I_f^3 \sin^3(\omega t) \quad \text{Eq. 15}$$

Relationships used to consider this equation in terms of frequency multiples:

$$\sin^2(x) = \frac{1}{2}[1 - \cos(2x)], \sin^3(x) = \frac{1}{4}[3\sin(x) - \sin(3x)] \quad \text{Eq. 16}$$

$$I_{tot}^3 = I_{DC}^3 + 2I_{DC}^2 I_f \sin(\omega t) + I_{DC} I_f^2 [1 - \cos(2\omega t)] + \frac{1}{4} I_f^3 [3\sin(\omega t) - \sin(3\omega t)] \quad \text{Eq. 17}$$

$$\Delta V = \alpha \cdot \frac{R_0^2}{G} \left(I_{DC}^3 + 2I_{DC}^2 I_f \sin(\omega t) + I_{DC} I_f^2 [1 - \cos(2\omega t)] + \frac{1}{4} I_f^3 [3\sin(\omega t) - \sin(3\omega t)] \right)$$

Eq. 18

The added DC offset causes us to be unable to lock-in to the whole signal. For this reason, we adopted a better strategy for the following measurements.

2.2.3 Current scheme

The current scheme has DC heating on the bottom device and AC sensing on the top device. The large-area emitter device is mounted on glass capillary tubes to permit some thermal isolation, and the temperature becomes quite stable within ~two hours.

Under this configuration, on the receiver:

$$I_s = I_f \sin(\omega t) \quad \text{Eq. 19}$$

$$\Delta V = \Delta T \cdot \alpha \cdot R_0 \cdot I_f \sin(\omega t) \rightarrow \Delta V_{1\omega} = \Delta T \cdot \alpha \cdot R_0 \cdot I_f \quad \text{Eq. 20}$$

On the emitter:

$$T_{tot} = \frac{\Delta Q}{G} = \frac{I_{DC}^2 \cdot R_Q}{G_{DC}} \quad \text{Eq. 21}$$

Because the emitter heating is purely DC, the temperature change can be calculated by the lock-in as:

$$\Delta T = \frac{\Delta V_{1\omega} \cdot I_f}{\alpha \cdot G_{DC}} \quad \text{Eq. 22}$$

This configuration allows for a relationship between ΔT and a locked-in frequency of ΔV. To derive the thermal conductance, the total temperature differential between the two devices is also needed. To that end, the emitter temperature is carefully measured (2.3.1), the self-heating of the receiver is characterized (2.3.2.3), and the ambient temperature of the chamber is enforced by a programmable temperature controller and noted.

It is to be noted as well that the frequency used for the measurements was also characterized to mitigate the effects of parasitic capacitance in the measurement system, as discussed below.

2.2.3.1 Frequency dependence of AC sensing

The measurement setup inherently has parasitic capacitances that cause loss. At low frequencies, this loss is low. At higher frequencies, capacitance leans toward being a short circuit and the losses increase. One way to be sure to measure the correct signal is to calculate the anticipated

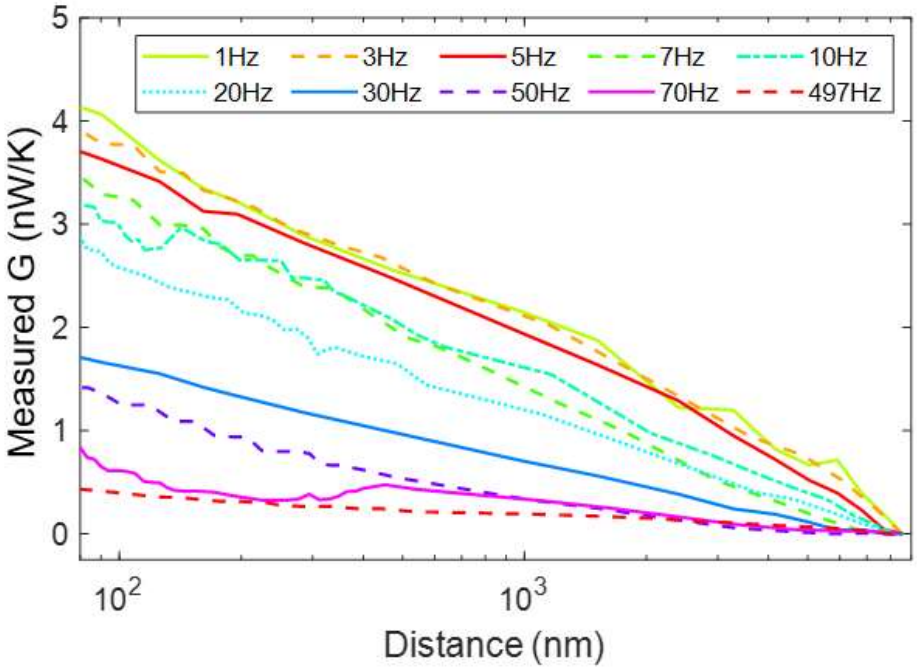

Figure 5: Frequency dependence of measured signal for sphere-sphere experiment (40 µm-70 µm silica). Increasing frequency for the AC sensing current causes increases losses in the parasitic capacitances of the measurement system.

capacitance of the setup and subsequent loss percentage at different frequencies. The easier way, and the route we chose, is to measure the signal with decreasing frequency until multiple curves converge. The results of this study are shown in Figure 5. We found that experiments conducted at 1, 3, and 5 Hz AC sensing frequency had high agreement between curves when measuring sphere-plane NFRHT. We chose 1 Hz to be sure of low loss in our measurements. The tradeoff for this choice is that lower frequencies are more susceptible to 1/f noise, however this was found to be of little or no impact

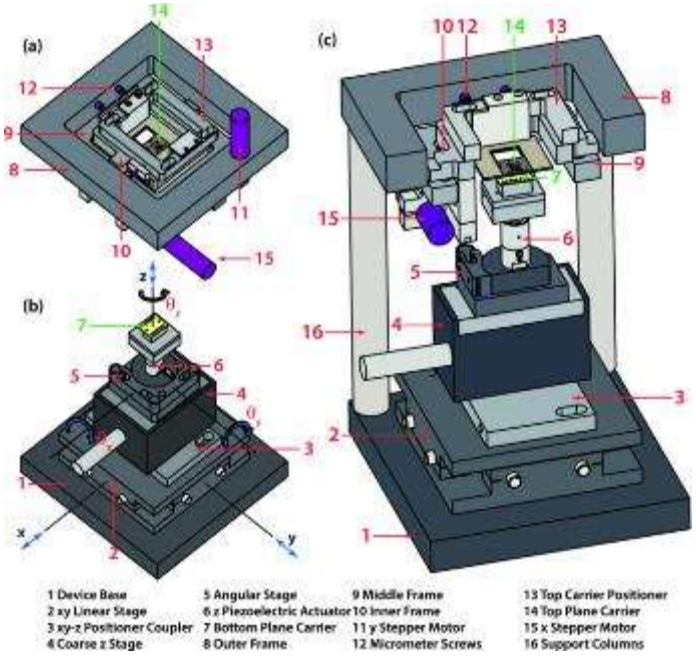

Figure 6: Nanopositioner schematic. Figure and caption copied with permission from reference 65. Schematic design of the nanopositioner with the major parts labeled: (a) the top subassembly is used to control the relative angular alignments θ_x, θ_y as well as to enable control of the relative alignment of the two planes along the x, y directions, (b) the bottom subassembly controls the relative alignment of the bottom plane along the x, y directions as well as the angular rotations about x, y, and z directions. The spatial separation is controlled using a z-linear stage and a piezoelectric actuator to control the position in z direction. (c) Sectional view of the top and bottom subassemblies assembled together by four columns (two of the columns are not shown for visual clarity).

2.3 Experimental Configuration

The heated and cold bodies are aligned and brought together with a custom-built nanopositioner platform[66] used primarily for NFRHT studies. An overview of the nanopositioner is shown in

Figure 6. Along with the experimental constraints on the devices used, the nanopositioner also provided constraints on the total size of the devices in all dimensions. It also permitted planarization of the bottom device, highly accurate alignment in the directions perpendicular to the vacuum gap, and predictable, nanometer-scale steps for closing the vacuum gap.

For the two-sphere experiment, the device constraints were as follows. First, it must be possible to heat one body predictably and measure the heat flux accurately. In many experimental studies performed in this group, the heater for the emitter is included on the device area of the emitter, which is isolated from the body of the emitter by beams to provide thermal isolation. This is because the vacuum chamber is temperature controlled to remain constantly at 23.7°C during measurements for reproducibility, and therefore maintaining consistent heating requires thermal isolation from the chamber body. In both of the experiments described, isolating the device body using microfabrication techniques added unnecessary complications in mounting the sphere or in transferring the graphene to the small, suspended area. Instead, both emitters are thermally isolated by placing small chips on a capillary tube, which has mounted thermistive heating and sensing.

The first constraint placed on the sensing device proved to be that it must be a separate device than that used for heating, as discussed in 2.2.2. For our purposes, that logically placed the heating responsibilities on the bottom device, and sensing on the top device. Next we considered that for a sphere-plane configuration, the heat flux is reduced by a few orders of magnitude as compared with the two-plane configuration, and a two-sphere configuration is reduced further by half (see 3.2.2 for a comparison of the proximity for approximation prediction for these geometries). The total predicted heat flux for a 10K temperature differential between two silicon dioxide spheres of radius 20 μm is only about 58 nW.

In the case of the graphene-mediated study, the sphere-plane configuration also decreases the total anticipated heat flux by orders of magnitude as compared with NFRHT between two planes separated by nanometer-scale gaps. Additionally, the predicted difference brought about by adjusting the backgate voltage is on the nanowatt level for most of the distance range (see section 4.2.3.2 for a prediction of SiO_2-graphene/SiO_2 heat transfer). For these reasons, the sensing device and scheme used for both measurements must have a sensitivity on the order of nanowatts. Because one factor in the sensitivity is high thermal isolation, this implies a need for beams isolating the device area that have a significant length to thickness ratio.

Second, the bottom device must be visible along the same focal axis as the top device, for alignment purposes. For the graphene-mediated study, this constraint is quite relaxed, as it has been for similar studies in which one device is significantly larger than the other. The graphene device area on the emitter was chosen to be 150 μm, while the silicon dioxide sphere is only ~40 μm in diameter. A rough alignment is therefore sufficient, and any device that permits an estimate of the expected center of the receiver could work. However, for the two-sphere experiment, a misalignment by only a few tens of micrometers could have caused the two-spheres to miss each other entirely, and it was important for the data analysis to have an estimate of the exact misalignment between them.

Therefore, for the two-sphere experiment, we had the constraint that the receiver sphere should be directly visible for best alignment. This changed our usual configuration expectation, in which the receiver device area is typically fully covered along the focal axis, by the idea that the receiver device area (the sphere) must be at most 50% covered.

Third, a low snap-in distance is desired for both experiments. The snap-in event is the moment when the stiffness of one or both of the two devices is overcome by the attractive forces

between them. This was not as significant a concern in the two-sphere case, as the Casimir force change for different geometries can quite well be predicted by the proximity force approximation[67], and we may therefore anticipate that in this case also the Casimir force is reduced by half for the two-sphere rather than the sphere-plane configuration. In the graphene-mediated study case, however, an additional force must be considered due to the significant voltage biasing used to tune the Fermi level of the graphene. This added capacitive force was calculated to be quite large, and the high length to width ratio anticipated for the receiver beams for sensitivity is therefore at odds with our goals for stiffness. The solution is to take the receiver probe and mount it such that the beam length is parallel to the direction of travel and the direction of least distance between the devices. Along this axis, even a device designed for high sensitivity can be extremely stiff. This configuration also exposes the receiver sphere to view, allowing accurate alignment for the two-sphere configuration.

Figure 7 shows an example configuration of devices for a two-sphere experiment. In the case of a sphere-plane experiment, such as for the silicon dioxide and graphene setup, the bottom sphere on a substrate is replaced by a planar substrate.

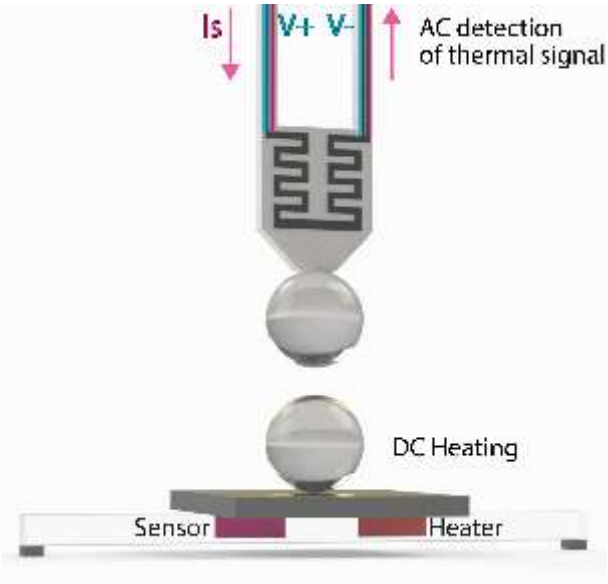

Figure 7: Example experimental configuration, two-sphere.

2.3.1 Bottom Device (Emitter)

As mentioned previously, thermal isolation beams and a platinum resistive serpentine, similar to the design of the receiver, would make an ideal structure for quick and uniform heating of the emitter device. However, this would have caused significant complications. For the graphene-mediated structure, microfabricating a suspended device with a usable backgate for tuning was inherently a challenge. Additionally, due to the extreme heat that wafers undergo during the through-etching required for suspension and the protective layer of photoresist used, the graphene layer would need to be deposited after the suspension or suffer severe baked-on photoresist contamination.

While a wet transfer of graphene is possible onto an arbitrary surface, the graphene, then on a micrometer-scale suspended structure, would need to be patterned to avoid shorting the heater serpentine. Deposition of photoresist on an object of that size requires technology our cleanroom does not currently have. A successful platinum serpentine pattern and a high yield on through-etched devices is already a series of characterizations that can be costly in terms of time

and cleanroom expenditure. However, should this be attempted, an additional characterization is recommended for successfully achieving this device configuration: if a silicon dioxide etch, wet or dry, is well-characterized, one could cover the serpentine with a deposited LPCVD silicon dioxide layer and then carefully etch it back to prevent an excessively thick graphene backgate. This would adequately prepare the device for a through-etch and subsequent, unpatterned, graphene transfer.

For the two-sphere experiment, the focused-ion beam (FIB) process used to attach spheres to their substrates is involved, but particularly time-intensive for aligned and suspended pieces such as the receiver. It was deemed unnecessary to repeat this complexity for the emitter as well.

2.3.2 Top Device (Receiver)

The receiver, as discussed previously, is vertically mounted to the top of the nanopositioner, and consists of a repurposed atomic force microscopy (AFM) probe with an FIB-attached sphere at the tip. A scanning electron microscope (SEM) image of the probe before addition of the tip is shown in Figure 8. An image of the tip with the sphere added is shown in sections 3.3 and 4.3.

2.3.2.1 Receiver Fabrication

The steps involved in the fabrication of the probe are as follows, using the process described in reference [68]. A trench was first etched into a bare silicon wafer through deep reactive ion etching (DRIE). A T-beam was then deposited using wet oxidation of the silicon and low pressure chemical vapor deposition (LPCVD) of 600nm of silicon nitride. The T-beams improve the stiffness of the probe cantilever. While the vertical configuration is meant to decrease the need for stiffness, this prevents it from drooping during the release step. The area of silicon nitride needed for the beams was then patterned on the backside of the wafer by reactive ion etching

(RIE). This layer of silicon nitride on the bottom serves as a hard mask for the final wet etch to release the devices. Afterwards, the tip was coated by a 150 nm chrome layer using a shadow mask. Next, a 50 nm thick serpentine Pt line was deposited using standard photolithography for creating a heater-thermometer for resistive heating and thermometry. Thicker gold is deposited for electrical contacts. Then, the front side of the wafer was covered by a 50 nm thick plasma enhanced chemical vapor deposition (PECVD) silicon nitride layer to hinder the etching rate of the deposited metals on the front side. Finally, the probe was released by KOH etching of Si.

2.3.2.2 Receiver Holder

The vertical mounting of the probe introduced additional challenges for the experiment compared with the horizontal mounting method typically used in this nanopositioner. First, the mounting stage is horizontal, and the electrical connections used for soldering are positioned above the mounting stage with only a small window for the top device. Therefore, the mounting device used for the receiver probe necessarily must create an “L”-shape, to thermally bond to the probe body and physically secure the device to the horizontal mounting stage. Additionally, soldering the electrical connections for the receiver device directly to the same plane as the receiver would require a width that could not fit, or they would need to be positioned vertically above the receiver, which would block microscope view and also proved to not fit in the range available for the coarse Z stage. Finally, there must be minimal height added to the receiver device by its mount, otherwise the large, but limited, working distance of the objective used would not be able to view the emitter device without crashing into the receiver above it.

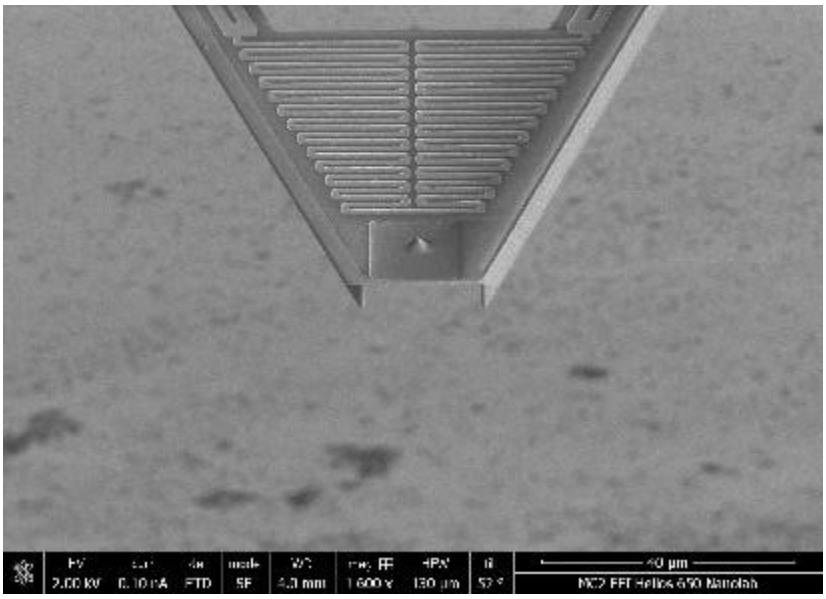

Figure 8: SEM image of AFM tip used for the receiver probe.

These constraints on the holder generate a logical picture of a straightforward design. It should be L-shaped, with a thermally conductive material connecting the probe to the nanopositioner for heat sinking purposes. There should be contact pads on the same plane as the probe, for convenient wirebonding, and there must be solder pads on the plane with the nanopositioner electrical contacts. Conductive stripes in a dielectric covering, for separation of the four contacts needed, on a metal L-shaped holder would be convenient for use.

An exact reproduction was not possible with available materials and an attempt is shown in Figure 9. With this version it was discovered just how limited the vertical size of the holder could be for the microscope to be able to view the bottom substrate without crashing into the top device, and that essentially there could be no overhead dedicated to the holder, even so much as the thickness of the holder itself in the microscope area.

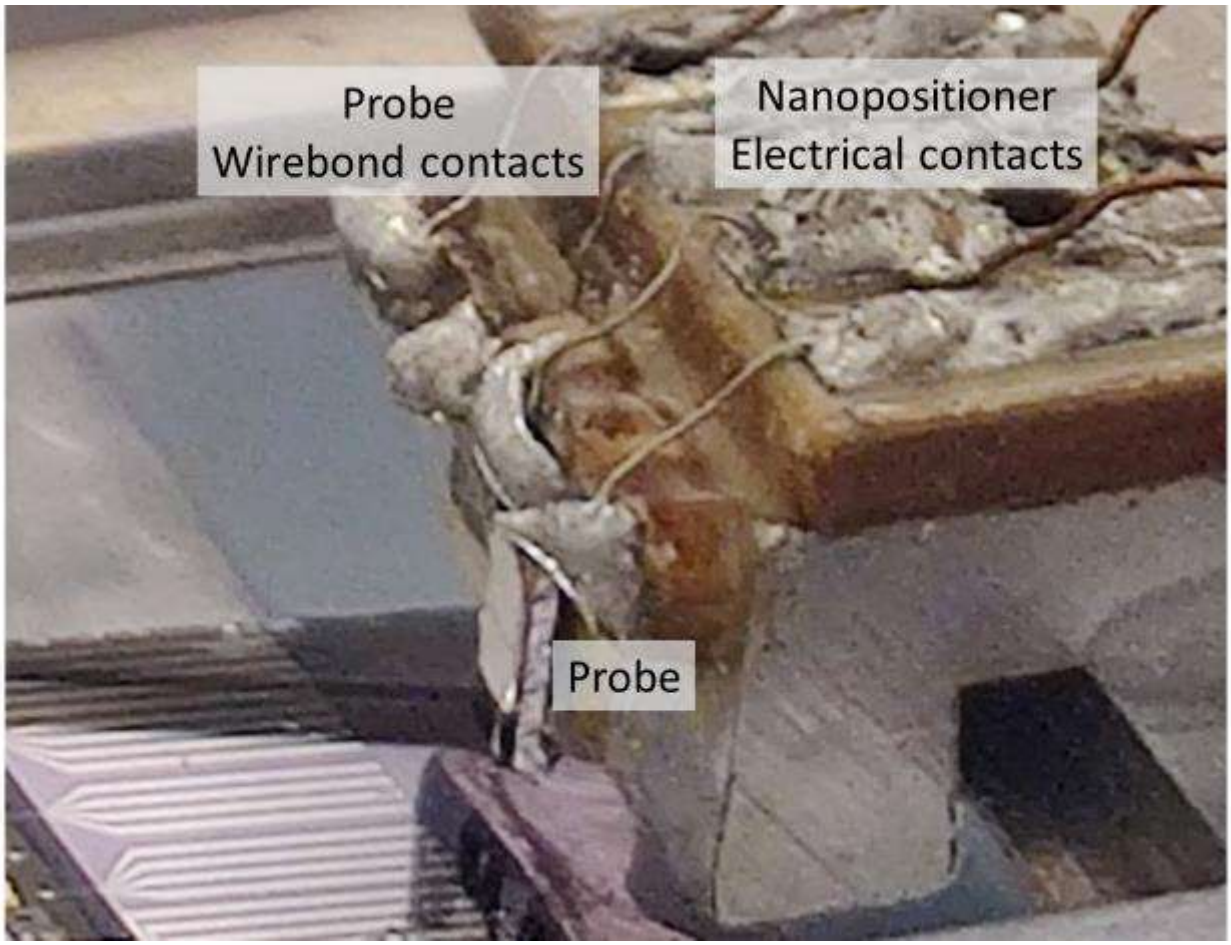

Figure 9: First prototype, L-shaped probe holder for vertically aligned measurements.

Instead, a version was made with an altered DIP chip as shown in Figure 10, and bonding was done in two parts. Connections were made to the probe by wirebonding before FIB attachment of the sphere. Subsequent wirebonding was found to often dislodge the sphere, and any wires that became detached were re-attached with silver paste. Conductive epoxy was originally attempted, but the baking temperature and time caused the 50-nm-thick platinum resistor on the probe to be removed at sharp corners, creating an open circuit between contacts. On the L-shaped holder side, the other end of the gold wire attached to the probe was originally soldered to the pins on the underside of the DIP chip, however this represented difficulties because gold wire dissolves almost instantly on contact with melted solder. Instead, this bond is

made with silver paste also, and solely the top side of the DIP chip connections are soldered, to the electrical connections on the positioner.

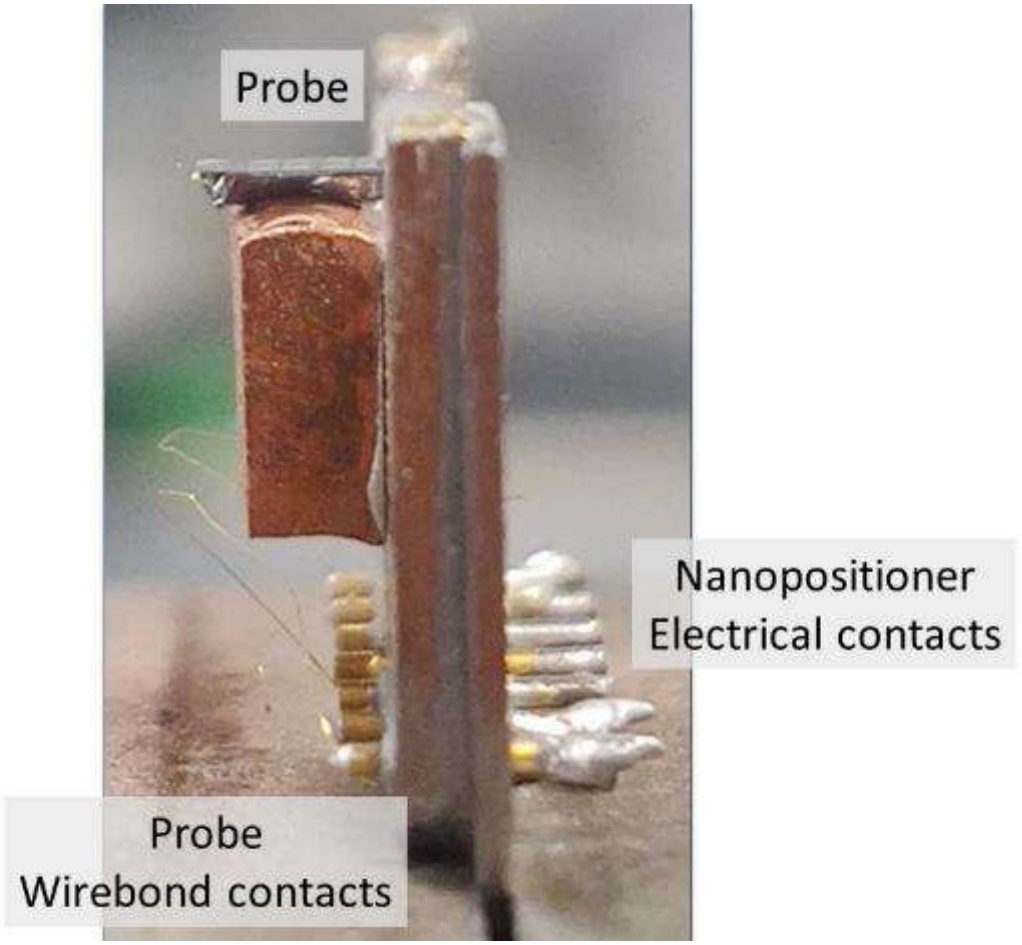

Figure 10: Final iteration, L-shaped probe holder for vertically aligned measurements.

2.3.2.2 Sensing Self-Heating

For determining the self-heating of the receiver probe during AC sensing, a 3ω measurement scheme is used. In this case, the scheme is AC heating and AC sensing on the same device, with only the resultant temperature input on the top device being measured.

$$I_s = I_f \sin(\omega t) \quad \text{Eq. 23}$$

$$\Delta V = \Delta T \cdot \alpha \cdot R_0 \cdot I_s = I_s^3 \cdot \alpha \cdot \frac{R_0^2}{G} \quad \text{Eq. 24}$$

$$I_S^3 = \frac{1}{4} I_f^3 [3\sin(\omega t) - \sin(3\omega t)] \quad \text{Eq. 25}$$

$$\Delta V_{3\omega} = \frac{1}{4} I_f^3 \cdot \alpha \cdot \frac{R_0^2}{G} \quad \text{Eq. 26}$$

$$\Delta T = I_S^2 \cdot \alpha \cdot \frac{R_0^2}{G} = \frac{I_f^2}{2} [1 - \cos(2\omega t)] \cdot \alpha \cdot \frac{R_0^2}{G} \quad \text{Eq. 27}$$

$$\Delta T_{2\omega} = \frac{I_f^2}{2} \cdot \alpha \cdot \frac{R_0^2}{G} \quad \text{Eq. 28}$$

$$\Delta T_{2\omega} = \frac{2 \cdot \Delta V_{3\omega}}{I_f} \quad \text{Eq. 29}$$

We use this measurement and calculation to consider the correct temperature for the receiver device when calculating the temperature differential, as the receiver device will not be identical to the chamber temperature.

2.3.3 Electrical Measurement of Thermal Voltage Signal

The change in resistance of the receiver probe's platinum serpentine resistor is captured with common-mode rejection of the far-field signal. This signal includes the room temperature resistance of the receiver probe's resistor and the far-field contributions to the receiver temperature. The input of one amplifier is adjusted using a potentiometer to be identical to the output of the receiver at the farthest point, such that V_{out} is as close to zero as possible (see Figure 11). This output is connected to a lock-in amplifier which is locked-in to the input AC current frequency, which decreases noise and increases sensitivity.

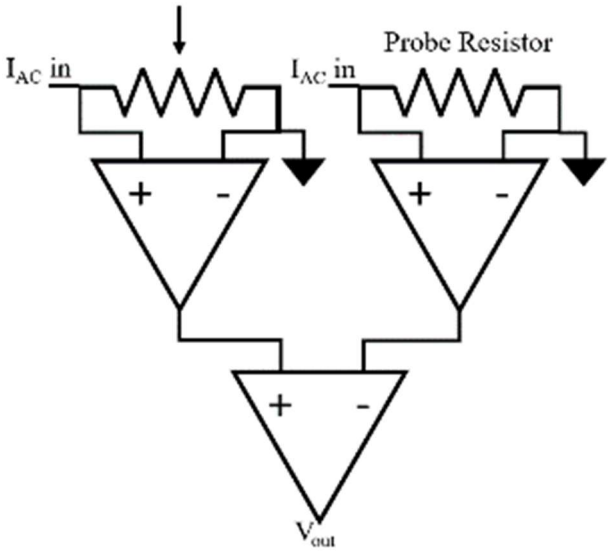

Figure 11: Half-Wheatstone bridge used for measurement of the signal change.

2.4 Data Analysis

The near-field experiments outlined in future chapters are carried out by measuring the locked-in voltage change during discrete piezo "steps". These steps are defined by applying a step-wise increasing voltage bias to the piezoelectric actuator and holding this position for a given length of settling time (10s) and then averaging time (30s). During the averaging time, the piezo input bias and the lock-in voltage are both measured at a set sampling frequency (100 Hz), and both the raw data and the averaged data are stored. As the thermal signal increases, indicating that contact is near, steps are decreased in size to avoid violently crashing the two bodies together, with a minimum approach step size of 1.76 nm. The experiment is halted when a sharp and distinct rise in the thermal signal is measured, indicating a conduction route and therefore contact. This point is referred to as the "snap-in" point, due to most experimental configurations having compliant devices which bend in the near-field and physically snap the gap closed to initiate contact.

2.4.1 Distance calculation

The piezoelectric actuator has a known size-bias relationship of 1.76 nm to 1 mV. All distances asserted for these measurements are relative distances, back-calculated from the contact point as determined by the thermal signal spike. This contact point is not set to 0 nm, due to the existence of sample roughness and particle contamination that prevents a perfectly clean meeting of devices. In other experiments with more compliant devices, the contact point must also include a calculation of the distance at which attractive forces between samples will overwhelm the device beams. In our case using the vertical configuration, this component is ignored, and only particles are considered as the overwhelming source of increased contact distance.

Establishing the piezo voltage bias immediately before the bias at the contact point as the minimum un-contacted distance, all other distances prior to the contact event are calculated by the bias difference from the pre-contact point · 1.76 nm / 1 mV.

2.4.2 Thermal conductance of probe beams

The DC thermal conductance is measured for each new probe used for measurements and is around 0.4 μW/K. It is also known to be ~1.6 μW/K for the AC thermal conductance .The DC value is used in calculation of the temperature change given the measured thermal voltage, given that the experiments use DC heating of the emitter. A full AC thermal conductance measurement is not needed for each new probe for calculations, but the rapid roll-off is indicative of an intact sphere-connection, given the large thermal capacitance of the sphere, and is therefore used during measurements to check for sphere loss after contact.

2.4.3 Temperature change calculation

The temperature change at each step is calculated using known constants and the voltage-temperature relationship derived in 2.2.3. Given a known average voltage measured on the lock-

in at each step, the voltage first has any amplified gain removed and is multiplied by $\sqrt{2}$ to obtain the RMS voltage. Then the equation is applied:

$$\Delta T = \frac{\Delta V_{1\omega} \cdot I_f}{\alpha \cdot G_{DC}} \quad \text{Eq. 30}$$

For this set of measurements, unless otherwise stated, $I_f = 10\ \mu A, \alpha = 1.85e-3$, and $G_{DC} = 0.4\ \mu W/K$.

2.5 Conclusions

The combined strategies of 1) a custom-built nW-scale resolution calorimetric probe that is 2) arranged in a vertical configuration and 3) mounted in a nanopositioner, with a 4) separated DC heating, AC sensing scheme were characterized and determined to be suitable for the measurements described in chapters 3 and 4. We anticipate that this system will continue to be highly useful for precision measurements of NFRHT with exacting alignment, thermal resolution, and mechanical strength constraints.

Chapter 3 NFRHT between Two Highly Curved Surfaces

3.1 Introduction

For a complete understanding of the NFRHT regime, experimental investigations must be conducted on a diverse range of materials and geometries. To date, the majority of studies have focused on sphere-plane[11,28,32–36] and plane-plane[21,62–64] geometries. Despite analytical studies predicting the heat transfer between a range of curved and arbitrary surfaces[23–27,69,70] and an experimental study on the Casimir force between two spheres[67], there is as yet no work experimentally determining the relationship between distance and heat transfer for two curved bodies in the near-field regime.

Experimental verification is important because of the interesting physical properties predicted for NFRHT between two spheres. The impact of the changing distance to radius ratio for two matched spheres[25] results in a near field thermal conductance vs distance slope that can be tuned by the choice of sphere diameter[23]. Additionally, there is growing interest in hyperbolic metamaterials (HMM) for enhanced NFRHT, and the choice of sphere size may be matched to the design of the HMM layers to add a resonance also at a target gap size[69,71].

Experiments between a sphere and a relatively large plane have historically been favored over sphere-sphere experiments due to the difficulty in ensuring precision alignment between very small spheres. In a nanopositioner style of measurement, which is necessary for such a geometry that does not permit spacers, misalignment on the order of tens of micrometers can result in drastic changes to the relative and absolute thermal conductance versus distance

measured between spheres or cause the two bodies to pass each other entirely in the axis of travel without ever entering the near field regime. The system used must also be highly sensitive to small changes in temperature, considering the reduction in heat transfer anticipated for two-sphere versus two-plane geometries, and yet stiff enough to prevent a premature snap-in between the devices.

This chapter begins to address the knowledge gap pertaining to spheres in NFRHT studies by detailing an experiment in which two ~20μm radius silicon dioxide spheres were gradually brought together, permitting measurement of the NFRHT at discrete steps from a distance of 9μm to 80nm. This was possible by utilizing a sensitive custom-fabricated thermal probe arranged in a vertical position for high-stiffness and a custom-built nanopositioner with micrometer resolution on alignment. Additionally, a similar sphere-plane experiment was conducted and compared with existing work, to validate the methodology within the literature existing for such a configuration[11,28,32–36].

We found that despite the relatively low absolute magnitude of thermal conductance for a dual-sphere configuration compared with planar geometries, there is still significant near-field enhancement. We measured a 15X increase in the average conductance measured, as the distance between two silicon dioxide spheres is systematically reduced from 5 μm to 80 nm. Our findings validate the feasibility of future experimental sphere studies and confirm the success of currently available numerically exact calculations in predicting NFRHT for this configuration.

3.1.1 Key Questions

In this chapter, I endeavor to answer the following questions:

- What is the measured NFRHT between two spheres?
- Do existing models sufficiently predict the NFRHT between two spheres?

3.2 Theoretical Methods for Prediction of NFRHT between Two Spheres

The experimental measurements of NFRHT in sphere geometries were subjected to a thorough evaluation to determine the congruence of different theoretical projections with the results. This was achieved by conducting a comparative analysis of four models: the proximity force approximation (PFA), a fluctuational electrodynamics solution using spherical Green's functions, and a boundary-element method calculation using SCUFF-EM. Previous work comparing the scattering matrix method to experimental data is also considered.

3.2.1 Modelling Spheres with the Proximity Force Approximation

The PFA model was begun by first employing the semi-analytical equation for the heat transfer coefficient between semi-infinite planes, which is rooted in fluctuational electrodynamics[72] and is discussed more thoroughly in section 1.2[11]:

$$h = \int_0^\infty \frac{d\omega}{4\pi^2} \frac{\delta\left[\hbar\omega / \left(e^{\hbar\omega/k_B T} - 1\right)\right]}{\delta T} \times \int_0^\infty dk k \cdot \tau(\omega, k) \qquad \text{Eq. 31}$$

Where $\tau(\omega,k)$ represents the sum of evanescent (τ_e) and propagating (τ_p) modes, for both transverse electric (s) and transverse magnetic (p) polarization, such that:

$$\begin{cases} \int_{\omega/c}^\infty \left[\frac{\left(1-|r_h^\eta|^2\right)\left(1-|r_c^\eta|^2\right)}{\left|1-r_h^\eta r_c^\eta \, exp(2ik_z d)\right|^2}\right] k_x dk_x, & \tau_p \\ \int_0^{\omega/c} 4\, exp(-2ik_z d) \left[\frac{Im\{r_h^\eta\} Im\{r_c^\eta\}}{\left|1-r_h^\eta r_c^\eta \, exp(2ik_z d)\right|^2}\right] k_x dk_x, & \tau_e \end{cases} \qquad \text{Eq. 32}$$

r_h is the "heated" side and r_c is the "cold" side. η=s,p, with both summed together so as to cover all polarization modes. The wavevector in the vacuum between two bodies, k_z, is found by:

$k_z(\omega)=(k_0^2-k_x^2)^{1/2}$, where $k_0=\omega/c$. d is the vacuum gap distance between the two semi-infinite planes.

Given this distance-dependent heat transfer coefficient, a thermal conductance prediction was calculated for sphere-plane or sphere-sphere configurations by decomposing each sphere into a collection of ring-shaped planes with finite surface area. Heat transfer coefficients were assigned to each ring based on their respective adjusted distances and multiplied by the ring surface area[73], as follows:

$$G_{PFA}(d_{pp}) = \int_0^R dr 2\pi r \cdot h(d_{pp}) \cdot A(d_{pp}) \quad \text{Eq. 33}$$

R is the outermost radius of the sphere, r is the changing evaluated radius of the circular area, and A is the area of the ring considered. The distance d_{pp} is the calculated closest point-to-point distance between the two bodies for a given annulus on the sphere:

$$d_{pp} = d + R - \sqrt{R^2 - r^2} \quad \text{Eq. 34}$$

For a sphere, d is the minimum distance from the sphere to the other body. Figure 12 provides an intuitive depiction of why larger radius circles with lower curvature are more plane-like. Within a +/- 0.5µm lateral distance from the apex of a 40 µm sphere, there is only ~6nm adjustment to the distance from the sphere to an adjacent body.

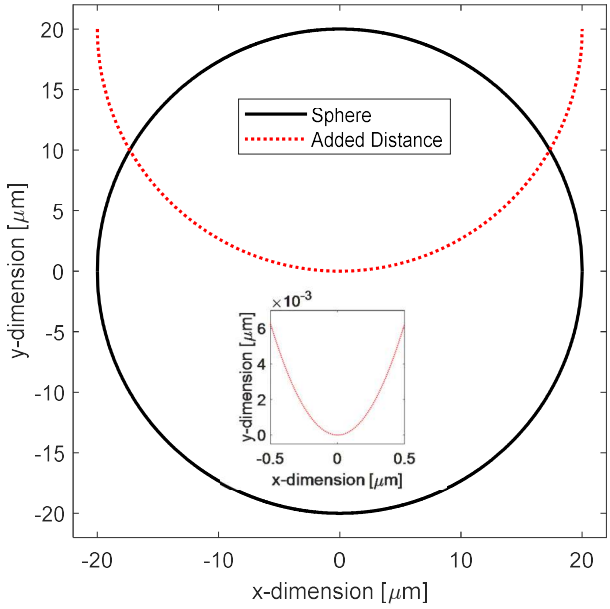

Figure 12: Constructed sphere representation used for distance adjustments. The inset shows the minimal increase in distance of 6 nm for a 1 μm diameter area.

3.2.1.1 NFRHT Relationship with Sphere/Plane Geometries and Size Variations

The impact of this conversion is outlined in Figure 13, demonstrating the predicted NFRHT for two fixed area planes for comparison with a PFA NFRHT prediction between a 45μm sphere and a semi-infinite plane. It is noteworthy that the plane-plane thermal conductance is significantly higher, owing to the varying distance of the ring areas in the sphere cases. This phenomenon is due to the swift escalation of thermal conductance with distance. Only a small portion of the 45 μm sphere's surface area is within the very near-field of the plane, representing a similar radiative thermal conductance to two circular silica planes of only 2 μm radius. The sphere-plane scenario is demonstrated also for spheres with radii of 15 μm and 75 μm, highlighting the impact of increased radius on thermal conductance. A larger radius results in a more plane-like structure with reduced curvature, and the larger surface area therefore in close proximity enhances thermal conductance. With these relationships in mind, the PFA prediction for NFRHT between two 40 μm diameter spheres is shown.

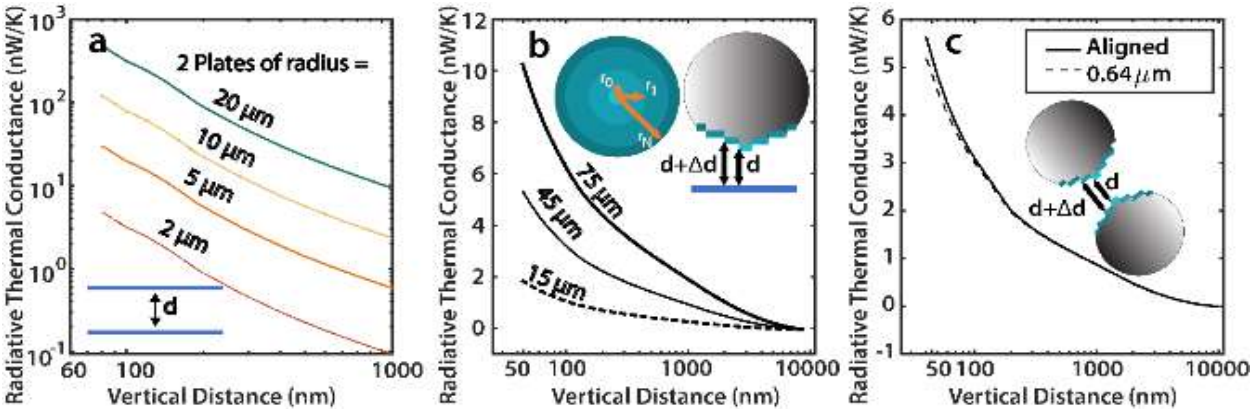

Figure 13: Comparison of near-field radiative thermal conductance in different geometries. This comparison uses PFA theory based in 2-plane Green's function formalism, plotted against the vertical motion of the piezo. a) Calculated plane-plane radiative conductance between two circular plates of varying surface area, up to the radius of a studied sphere. The inset shows two plates at a given gap distance equal to the vertical distance. From this, we can interpret naively that the two orders of magnitude change in conductance over 1 μm of travel would cause only a small portion of a 40 μm sphere to dominate the contribution. b) A PFA extrapolation of plane-plane theory to sphere-plane geometry, for different sphere diameters. The calculation is performed for N concentric rings of a given area and corresponding adjusted distances. The inset shows the varying inner and outer radii of the rings and adjusted distance from the plane, at a minimum gap distance equal to the vertical distance. c) Further PFA extrapolation of plane-plane theory to a sphere-sphere configuration, such that the adjustment to the gap distance is now caused by the arc of both spheres. For an imperfect alignment as shown in the inset and the dashed curve, the minimum distance used for calculation incorporates both a lateral shift and the minimum vertical distance between spheres, leading to a small difference in the predicted very near-field regime from the curve for two perfectly aligned spheres.

The small anticipated change due to misalignment is also compared, and the two misaligned spheres are depicted, for a clearer understanding of the approximation being made. In both two-sphere cases, the minimum distance between rings is calculated using the changing center-to-center distance of the spheres as the vertical position of one sphere is changed, less the radii of both spheres.

3.2.2 Spherical Green's Function Formulation

A more exact calculation can be performed than the PFA still using a solution method similar to Polder and Hove. Rather than calculating the heat transfer coefficient from fluctuating currents using Green's functions for two planes and then approximating the change for spheres, the calculation can be directly constructed for two spheres by using spherical Green's functions as

described in detail in reference [23]. The authors of the paper explain that the results are not identical, in particular, the far-field estimate using PFA is too low.

A downside to using this solution method is the considerable computation time. Direct solution for 10's of micron-scale spheres takes a considerable amount of time to converge that increases with decreasing distance/radius ratio, even as high as for 100's of nanometer-scale gaps the time may be prohibitive. There is not a semi-analytical solution method yet determined for this geometry that could simplify solution. As a partial workaround, the authors produced an analytical solution via curve fitting for extrapolation beyond the calculated range. The fitting parameters were developed over a range from 0.2 to 8μm. Figure 14 shows the differing range between the total extrapolated range used for comparison with experimental data in this study and the original range covering exact data.

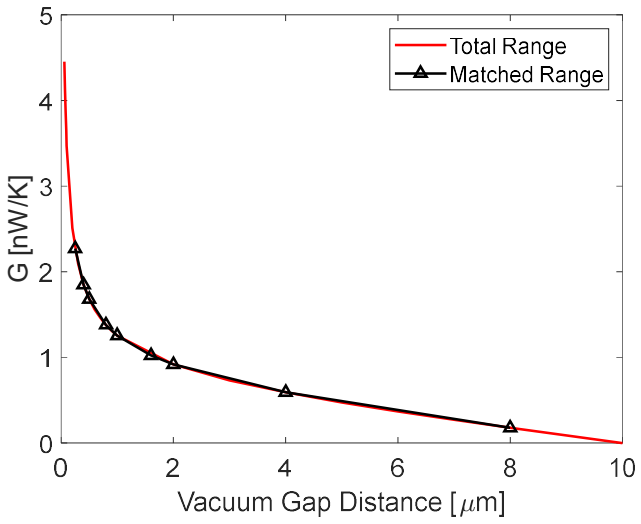

Figure 14: Data range used for development of analytical equation vs total range the equation was used.

3.2.3 Boundary element method calculation with SCUFF-EM

The second model compared is an analytical function fitted to a numerically exact calculation of heat transfer using a fluctuating surface current formulation[25] combined with the boundary-

element method. This calculation employed the open-source SCUFF-EM solver[74] to calculate the NFRHT between two 20 μm radius spheres. This solver discretizes the surfaces of the bodies under study into a mesh of triangular elements and then treats the surface currents in each element as piecewise low-degree polynomials, in the RWG method[75]. Similar to the Green's function method, this computation was highly time-intensive for distances at which the radius to vacuum gap ratio was high. Therefore, the SCUFF-EM calculations were carried out within the distance range of 0.5 to 10 μm and extrapolated to smaller distances by determining a least-squares fit to an analytical model of similar form used by Narayanaswamy et al as discussed above. The form of both analytical functions is:

$$G = A_1 d^{-n} + A_2 x + A_3 \qquad \text{Eq. 35}$$

The analytical curve is compared to the calculated data points used for fitting in Figure 15. For this model, the parameters are shown in Table 1 for a fitting with $r^2 > 99\%$.

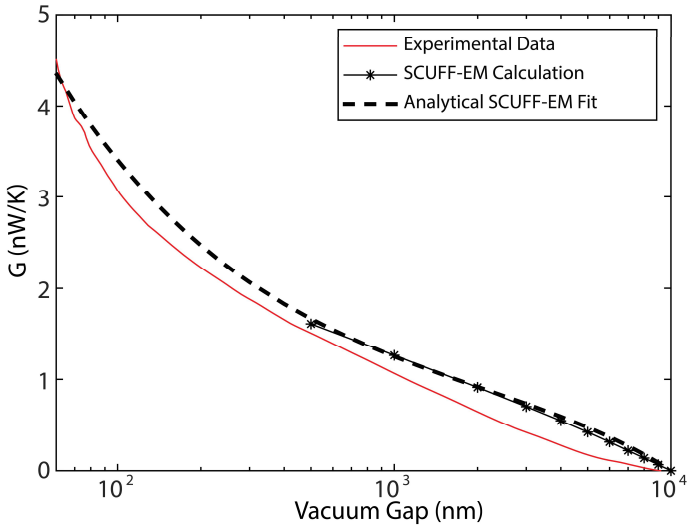

Figure 15: Analytical curve fit to SCUFF-EM data.

Table 1: Parameters for SCUFF-EM Fitting Model. x is the gap distance in μm. The output is conductance in W/K.

A_1	A_2	A_3	n
0.7999	-0.07457	0.4935	0.56

A comparison between the described analytical function and the SCUFF-EM prediction is demonstrated in Figure 16, and a strong agreement is found. To compare the sphere-plane data with SCUFF-EM predictions, a factor of two was multiplied by the two-sphere theoretical result, based on the PFA relationship between the configurations.

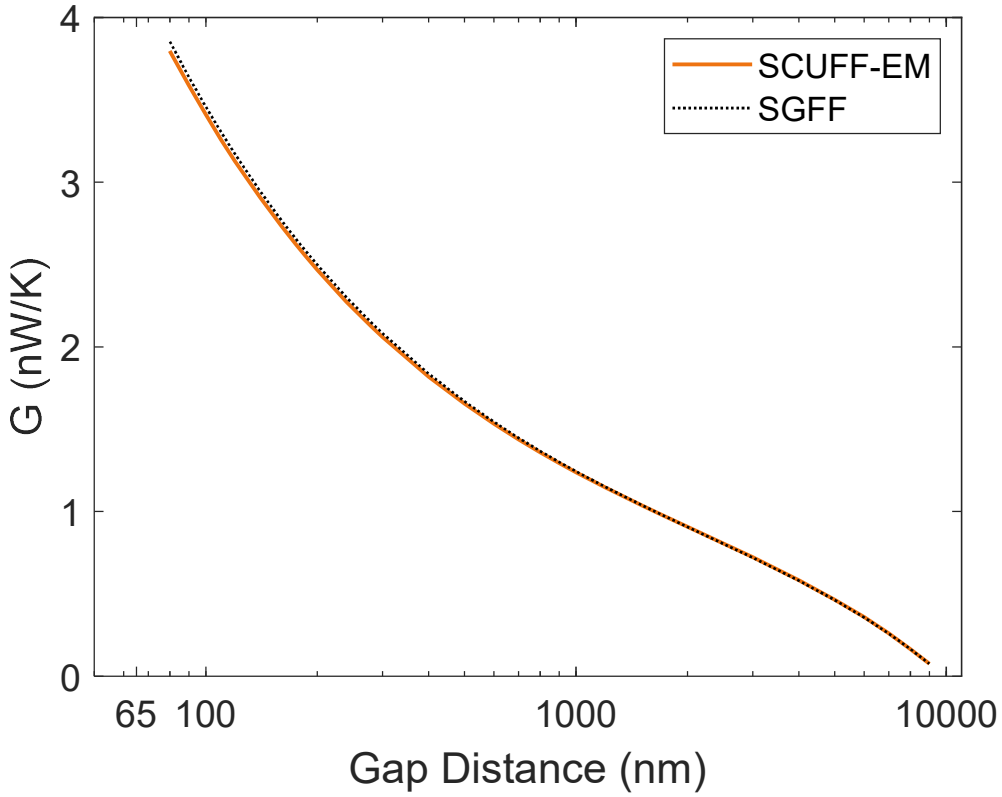

Figure 16: Comparison of analytical functions for SCUFF-EM and Spherical Green's Function Formalism calculations

3.2.4 Scattering matrix method

One solution method suitable for arbitrary geometries is the scattering matrix method. This technique employs formulas that are not directly linked to any specific wave basis, instead relying on scattering operators that encode an object's geometry and optical properties, as well as using Green's function for the free space[25,30].

In a work by Otey and Fan[28], the scattering matrix method is used to compare numerically exact results to popular approximations, for a sphere-plane configuration. We

compare their results, shown in Figure 17 qualitatively with the SCUFF-EM computational results for radiation between two identical spheres.

Their findings are as follows. The dipole approximation (DA), which is not compared to our experimental results here due to unsuitability, is an approximation treating a sphere as a point-like source. Intuitively we may suspect this is most accurate when the sphere is smallest, and the results bear out this expectation, with larger sphere sizes displaying good approximation under DA for larger gap sizes. For a sphere of radius 20 μm, this calculation predicts that the PFA will underestimate the heat flux at every gap size, and we will find when we compare experimental data to the PFA, that this is the case.

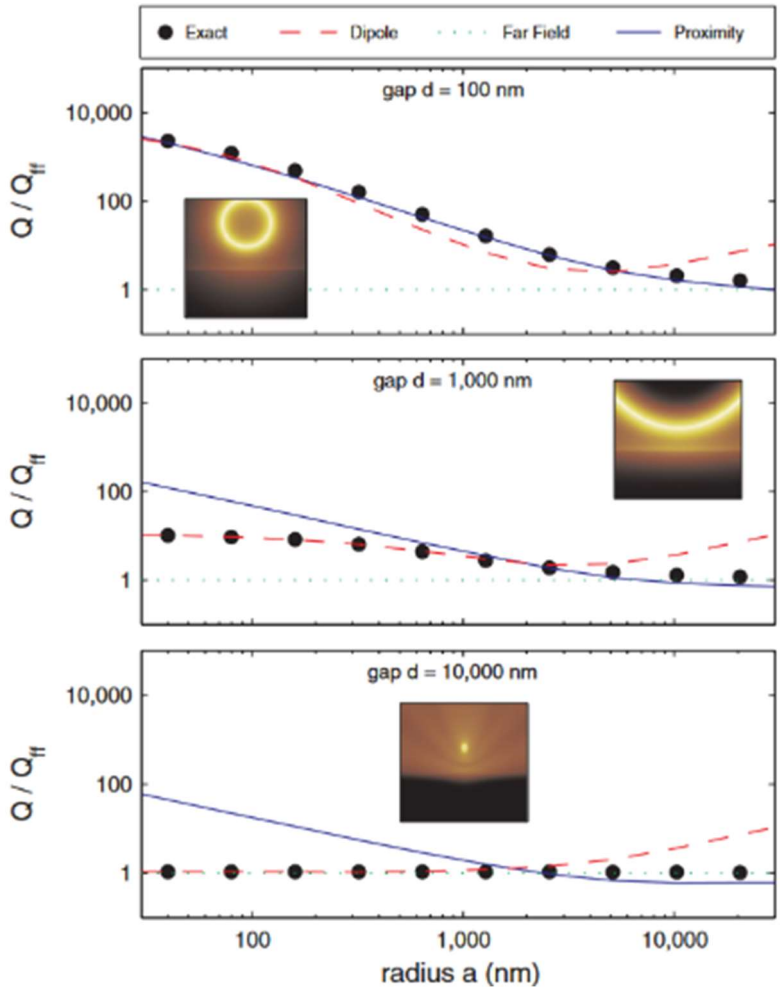

Figure 17: Heat flux between a sphere and a plane for varying sphere radius and gap sizes. Copied with permission from reference 28.

3.3 Experimental Configuration

The present study employs two samples supporting silica spheres for measurement of the NFRHT, which will be referred to as the emitter (heated bottom device) and receiver (room temperature top device), as presented in Figure 18.

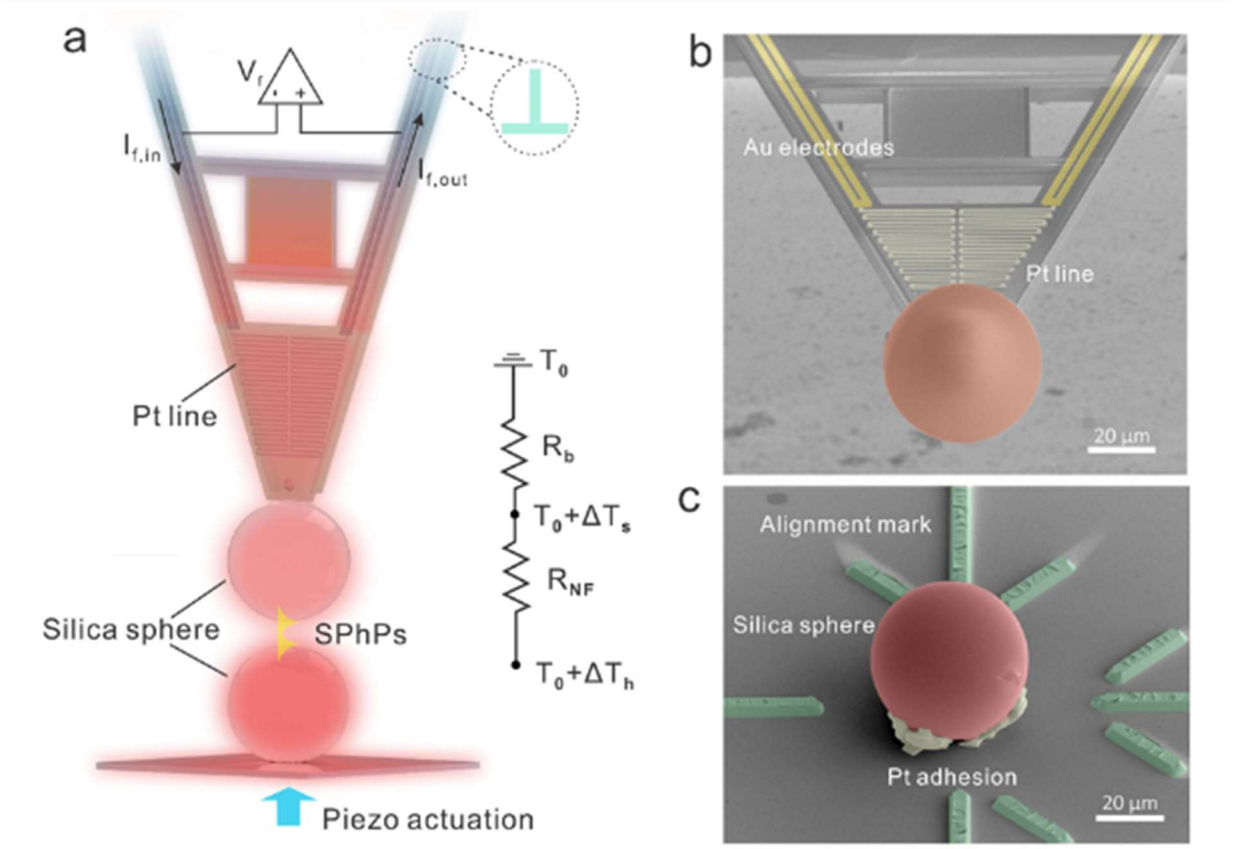

Figure 18: Experimental configuration for two-sphere study. Diagram of the experimental setup for measurement of the NFRHT between two silica spheres. Resistive heating below the emitter substrate is tracked with a thermistor. The probe tip on the top device uses a 4-point AC measurement and a lock-in amplifier to detect small changes in the platinum serpentine resistance. The inset details the thermal resistance circuit. b) A colorized SEM image of the top/receiver device. c) A colorized SEM image of the bottom/emitter device.

The emitter was heated above the receiver temperature by passing a DC current through the embedded heating resistor, targeting a temperature rise of 10-30K with the exact rise measured by the embedded thermistor. The corresponding temperature rise of the receiver due to radiative heat transfer was determined by passing a sinusoidal current (*I*) of frequency *f* through the top probe's platinum serpentine resistor and measuring the resultant voltage (V_f). This variation in voltage is converted to the change in the receiver temperature (ΔT_c) using the known TCR of the thin film platinum (α) and the room-temperature resistance of the serpentine (R_0) through the relation: $\Delta T_c = \Delta V_f / I \alpha R_0$.

3.3.1 Emitter (Bottom) Device

The emitter sphere is attached to a silicon substrate that is coated with 500 nm of e-beam evaporated gold, using an electron/ion dual beam system and procedures described elsewhere[76]. The gold film contributes little to the NFRHT because the matched phonon-polariton modes from the silicon dioxide spheres dominate in comparison to the relatively weak Au-SiO_2 transfer[11], thus eliminating the possibility that the measured significant near-field enhancement originates from the supporting substrate. Two resistors are secured to the borosilicate glass capillary tubes supporting the substrate, providing heating and temperature monitoring for the emitter. For the sphere-plane study, the bottom substrate and sphere are replaced by a silicon substrate coated with 2μm of thermally grown SiO_2. For the control sphere-plane study, the bottom substrate and sphere are replaced by a silicon substrate coated with 2μm of thermally grown SiO_2. Two resistors are secured to the borosilicate glass capillary tubes supporting the substrate, providing heating and temperature monitoring for the emitter.

3.3.1.1 Emitter Temperature Data

The emitter temperature is found using interpolation from a table of resistance to temperature values provided by the manufacturer of the thermistor sensor (US Sensor). The value of resistance for the thermistor was recorded for every measurement, and the value was used in computation of the thermal differential for each measurement. Table 2 below details the measured average temperature differences for the nominal temperatures as well as the range for each measurement set.

Table 2: Emitter temperature recordings for each data set.

Nominal δT	*Average R of Em. (Ω)*	*Average δT (°C)*	*Range(°C)*
10 (S-P)	7377	7.6974	N/A
10 (S-S)	7020	9.0329	0.1000 (1.11%)
15 (S-S)	5810	14.0470	0.0275 (0.20%)
20 (S-S)	4865	18.8553	0.0281 (0.15%)
25 (S-S)	4107	23.5580	0.0479 (0.20%)
30 (S-S)	3376	29.1471	0.0688 (0.24%)

3.3.2 Receiver (Top) Device

The receiver sphere (46 μm diameter) is mounted onto a stiff custom-fabricated thermal probe using similar procedures, similar to those used in other studies[68] and discussed in further detail in section 2.3.2, which is mounted to the top of a custom-built nanopositioner[66], outlined in section 2.3. An SEM image was shared in Figure 18b.

3.3.2.1 Thermal Conductance of the Receiver

Thermal conductance of the receiver probe beams was measured using DC current without heating on the emitter as a necessary component of the heat transfer calculation and is shown in Figure 19. For these measurements, $\delta T = {\Delta R}/{\alpha * R_0}$, and $Q = I^2R$. α is the thermal coefficient of resistance of the platinum resistor. $G = Q/\delta T$, a relationship which is established using a line of best fit. The DC thermal conductance was found to be 0.44μW/K.

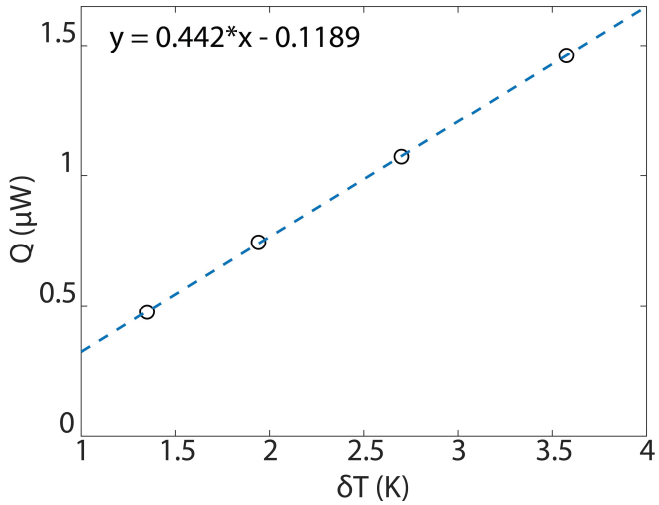

Figure 19: DC thermal conductance of receiver probe beams

3.3.2.2 Frequency Dependence of Self-Heating of Receiver

The self-heating effect for our measurement conditions was measured by sweeping the frequency of the applied 10μA current and detecting the temperature rise with a 3ω lock-in measurement, shown in Figure 20. For this measurement, $\delta T = {}^{2V_{3\omega}}/_{I_{1\omega}\alpha R}$. At our chosen frequency of 5Hz, the self-heating is 1.23K above the temperature of the temperature-controlled chamber.

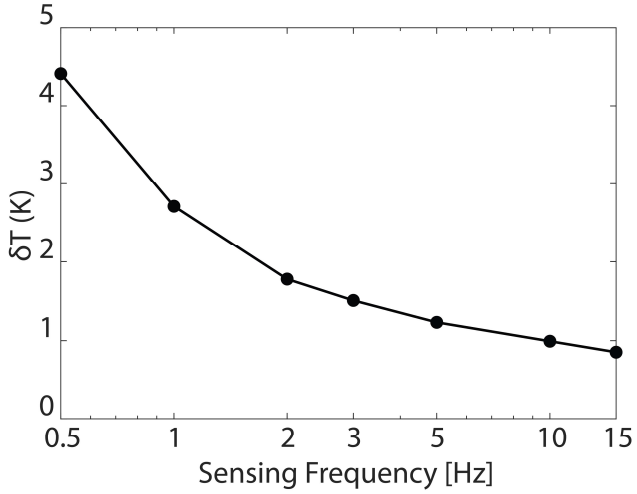

Figure 20: Frequency dependent self-heating of receiver probe.

3.3.2.3 Receiver Temperature Calculation

To calculate the radiative thermal conductance, the heat flux is divided by the difference in temperature between the receiver and the emitter. The emitter temperature was varied for each temperature dataset as discussed in the next portion, while the receiver temperature remained nominally equal to the chamber temperature plus self-heating due to the sensing current in the platinum serpentine.

Self-heating for a 10μA, 5Hz AC sensing current was found in the frequency-dependent characterization to be 1.23°C. The temperature of the chamber is controlled to be a constant 23.7°C. In total the receiver temperature is considered to be 24.93°C.

3.3.3 Alignment Method

The lateral alignment of two spheres is achieved by using imaging software to arrange the spheres along the microscope's focal axis, which is aligned with the axis of travel for the emitter using a differential micromanipulator stage. The process is depicted in Figure 21and involves

bringing the receiver sphere into focus, drawing a red box around the sphere area in the imaging software, and then refocusing the microscope downwards onto the emitter sphere. The emitter sphere is then manually moved using a precision displacement stage to locate it exactly within the red square.

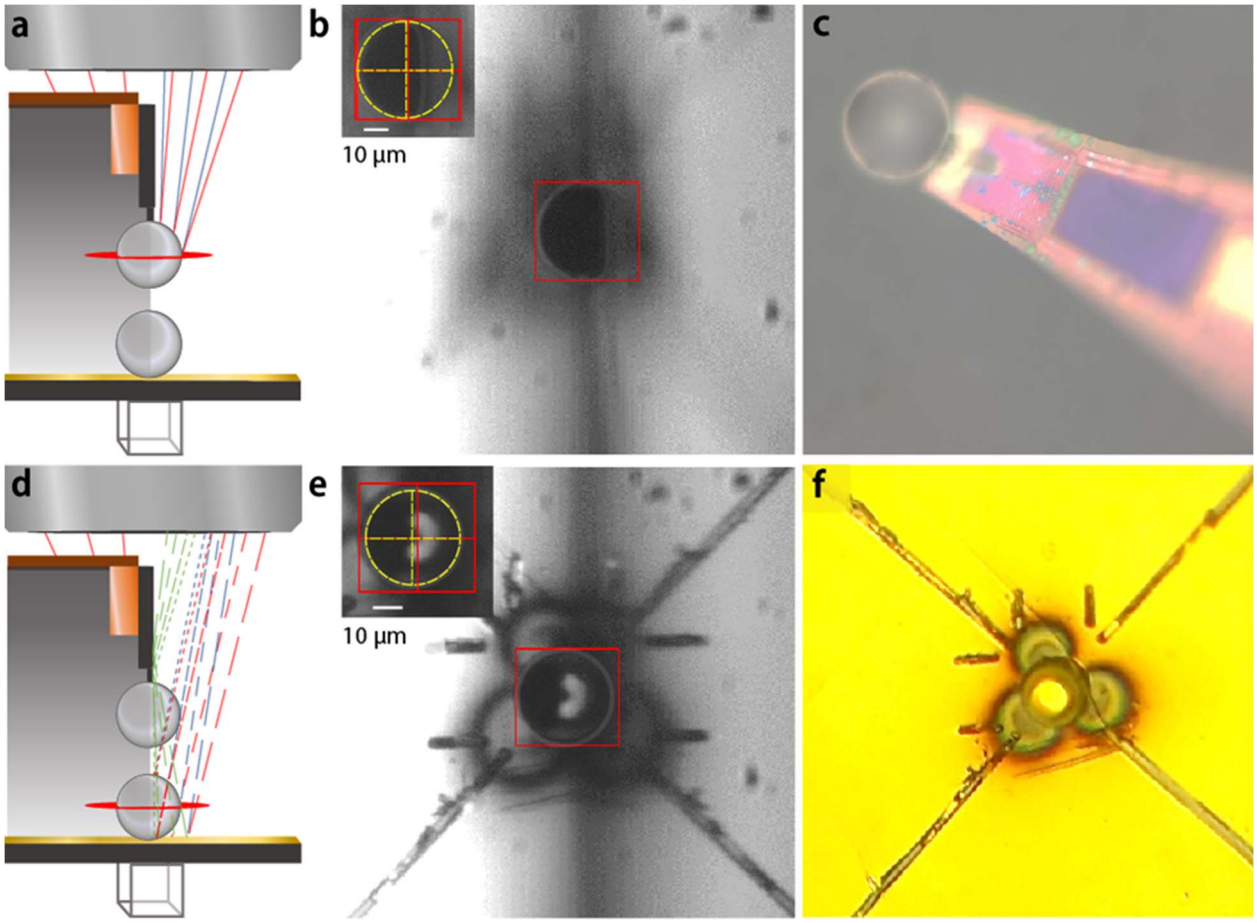

Figure 21: Alignment method and offset measurement for two-sphere measurement. Red lines show incident light, dark blue and light green represent light reflected once and twice, respectively. Circles drawn around spheres are to guide the eye. a) The top sphere is chosen as the plane of focus. Part of the view is obscured by the apparatus used to mount the sphere. b) An image taken at the focus point shown in (a), with a red square drawn in imaging software. Inset shows an offset measurement. c) Full-color image of the probe tip with the mounted sphere. d) The bottom sphere is chosen as the plane of focus. A reflected image is expected from the underlying plane as shown in the ray diagram. e) An image taken in at the focus point shown in (c), with the bottom sphere centered inside the red square drawn in (b). Inset shows an offset measurement. f) Full-color image of the bottom substrate. Arrows patterned in the gold help locate the sphere. The three-leaf clover pattern below the sphere is caused by incidental ion beam removal of gold during FIB platinum bonding to the substrate.

The alignment process is limited to repeatable movements of 1 μm by the differential movement of the stage. A quantitative measure of the misalignment was achieved using images captured during the setup. Offsets were calculated by counting pixels from the center of the red box to the centers of the spheres, and the total offset was found to be 0.64μm. Alignment on a nanometer scale is not critical due to the minor impact on the predicted heat flow. It is, however, essential that the piezo stage is confirmed to be flat in the optical plane in advance of these measurements, which was achieved by tilting a 15mmX15mm silicon piece under an objective lens until all corners were resolved at the same focusing distance. For this objective with a magnification of 50X and a numerical aperture of 0.55, the depth of field is ~2 μm, the angular deviation was limited by the angular resolution for the positioner (250 μrad). For the 9 μm distance traveled, this corresponds to a maximum negligible additional horizontal shift of 2.25nm between the spheres.

3.3.3.1 Misalignment Impact on Heat Transfer

Error in the alignment quantification was not presented due to the negligible impact of even a few micrometers on the relationship between the thermal conductance and the gap distance determined using piezo stepper voltage data. This is because horizontally shifting the spheres primarily changes the absolute gap, rather than drastically changing the relationship between vertical travel and the gap distance. Because the gap distance is assessed in a relative manner, back-calculated from the point of snap-in, the absolute change is inconsequential. For this calculation the motion of the piezo is assumed to be directly vertical, and we can consider a vertical distance between the lowest point of the top sphere and the highest point of the bottom sphere, z. The minimum distance between the spheres, d, will be equal to z in the ideal case of

two spheres with perfectly aligned centers and no horizontal displacement between the two sphere centers, h. These parameters are shown in the inset of Figure 22a.

In Figure 22a, the minimum distance is plotted against the vertical distance for several horizontal displacements, with an indistinguishable difference for the displacements plotted. In the inset, the vicinity of the snap-in distance of d = 80nm is shown. A negative number on the x-axis represents the top point of the bottom sphere moving above the lowest point of the bottom sphere, but the snap-in point will be considered to be 80nm in the direction of minimum distance between the two spheres and all previous distances adjusted accordingly). We can see that the difference in minimum distance between spheres for horizontal displacements of 0.64 µm to 5 µm (~24% of the smaller sphere's radius) is less than 0.5 nm for the same vertical distance input. Likewise, the inset of Figure 22b for the same vertical distance range shows that near snap-in, the change in predicted thermal conductance for horizontal displacement distances 0.64 µm to 5 µm is less than 1% of one nanowatt per Kelvin.

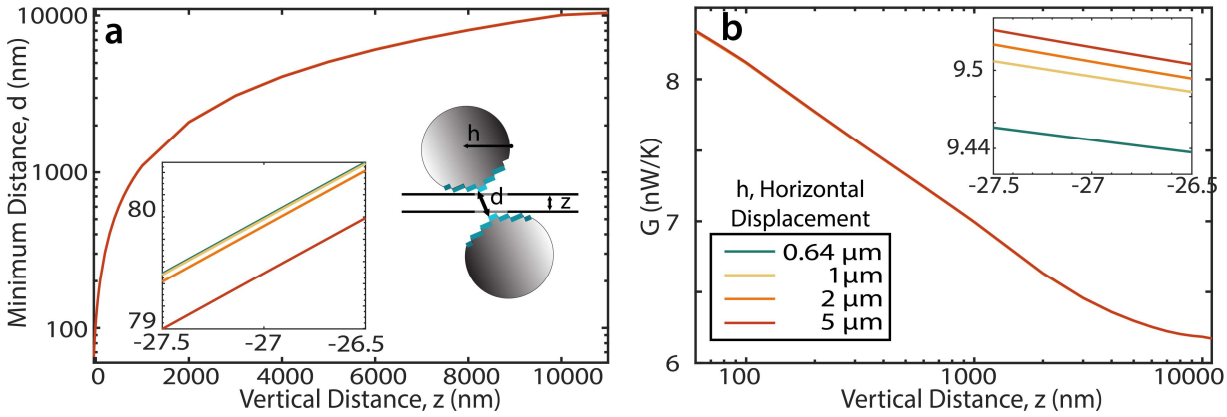

Figure 22: Negligible impact of horizontal displacement. Negligible impact of horizontal displacement on the relationship between both (a) the vertical distance between two spheres and the minimum distance between two spheres and (b). the vertical distance between two spheres and the predicted thermal conductance The S13a insets depict a zoomed-in view of the first relationship near the snap in distance (left) and the parameters discussed for this calculation (right). The legend in (b) represents the horizontal displacements considered for both a and b. b's inset depicts the <0.01nW/K difference in thermal conductance caused by a 0.64 µm up to a 5 µm horizontal displacement between the two sphere centers, indicating the disproportionately low error in thermal conductance calculation for even a few micrometers of error in the alignment calculation.

3.3.4 Repeatability Considerations

Both spheres are fastened to their respective apparatus using focused ion beam (FIB)-deposited platinum and are assumed to be in perfect thermal contact with their respective substrates. All measurements were conducted in a high-vacuum environment below 2 μTorr and followed a minimum stabilization period of two hours prior to conducting each set of measurements after adjusting the emitter temperature. Five measurements were repeated at each temperature differential with a 30 minute delay between for the two-sphere configuration, and the maximum result was used for comparison. One measurement was taken for the sphere-plane measurement shown due to available verification data in the literature, confirming a reasonable result. The stability of the alignment between spheres was verified by removing the goniometer from the microscope area to the high-vacuum setup and back and checking that the alignment had not shifted. Additionally, the emitter was moved away from the microscope objective a total travel distance of 30 μm without any visible shift relative to the imaged box, confirming that the travel axis and microscope axis were in alignment.

3.4 Raw Data and Calculation Methodology

The results shown for this experiment are plotted in terms of heat flux or thermal conductance versus distance, however the raw data is collected entirely in terms of the lock-in voltage measured and verification of the piezoelectric motor voltage applied. This raw data is shown below along with explanation of the parameters and calculations used for extracting the results from the raw data.

3.4.1 Raw Data from a Single Approach

The two samples are moved closer together by increasing the voltage of the piezoelectric nanostepper underneath the emitter. Figure 23 shows the change in piezo voltage applied and the resulting measured RMS voltage on the lock-in (V_{out}), which is allowed to settle for 10s, then measured for 30 seconds, and then averaged at each step over the 30 second measurement. From these data, a temperature change can be derived as a function of distance since the piezo distance vs. voltage is known. This dataset is representative of a single distance sweep taken for each temperature.

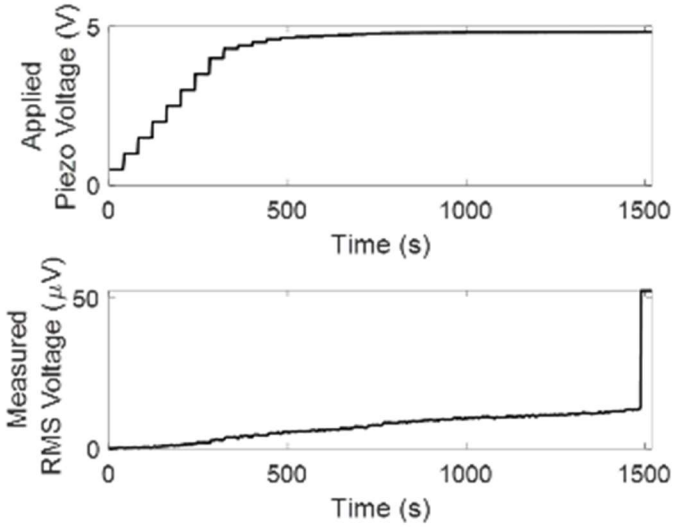

Figure 23: Relationship between piezo voltage and RMS *Vout*, here both displayed as a function of time. The sharp rise in the measured signal during the final time period indicates snap-in.

Without the contact at the end, the relationship between the piezo steps becomes clearer, as shown in Figure 24. This is indicative of a near-field enhancement.

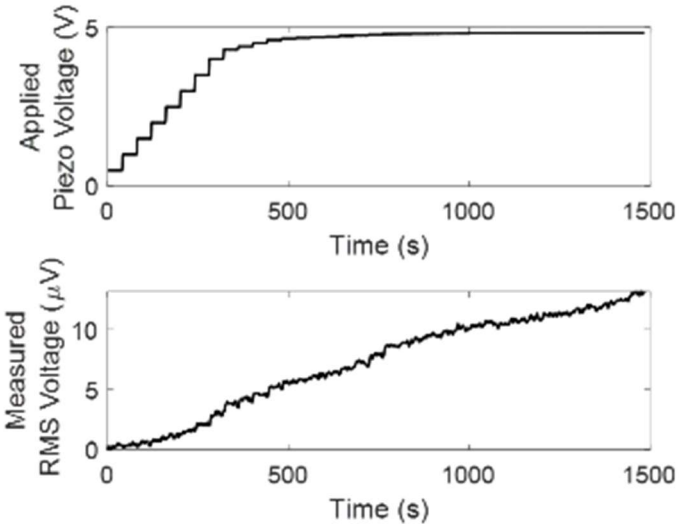

Figure 24: Relationship between piezo voltage and RMS *Vout* as a function of time, without contact point. The time period is clipped to exclude snap-in, to better illustrate the near-field signal enhancement.

3.4.2 Temperature Change Calculation

The basis for calculating the temperature change was discussed in further detail in section 2.2.3, and uses known constants or parameters measured within the experiment, such as the temperature coefficient of resistance for thin film platinum, α, and the room temperature four-point-probe resistance of the receiver probe, R_0.

3.4.2.1 Temperature Change from Voltage

The temperature coefficient of resistance (α) for the receiver platinum line has been measured in a previous study to be α=1.85e-3/K at room temperature[77]. Given the change in voltage measured on the lock-in, the temperature change then is:

$$\delta T = \frac{V_{out} \cdot \sqrt{2}}{I \cdot \alpha \cdot R_0} \qquad \text{Eq. 36}$$

The heat flux can be obtained from the known DC thermal conductance of the beams, such that:

$$Q_{DC} = \delta T \cdot G_{DC} \quad \text{Eq. 37}$$

Both the temperature change during this measurement and the heat flux are plotted in Figure 25.

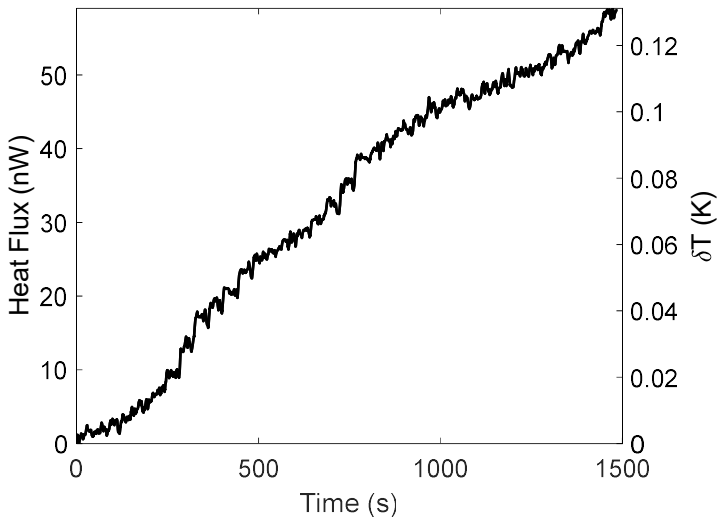

Figure 25: Heat flux and *dT* calculated from the above voltage measurement, as the two spheres approach each other.

3.4.3 Snap-In Distance Calculation

Previous studies have shown that it is critical to measure AFM data on any devices after the experiment, as additional particles may be introduced into the system after initial inspection. For this paper, we obtained sphere AFM data and found that there is a maximum particle size of 40nm, as shown in Figure 26.

Due to the presence of many particles, and repeated contact first with the planar device and then the second sphere, it is interpreted that this particle distribution is similar across all devices. Stiffness of the probe is not considered, as the probe is mounted vertically and parallel to the axis of contact. Therefore, an estimated snap-in distance of 40nm + 40nm + 0 is used. An exact prediction is difficult as it is not possible to simultaneously align the devices and view particles, due to differences in the objective lenses needed.

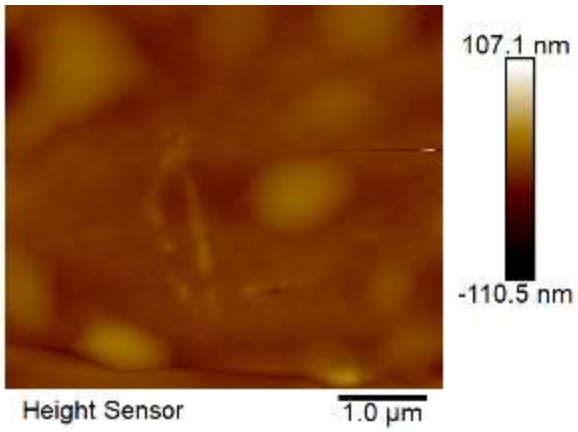

Figure 26: AFM study of sphere device, showing the particles used for estimation of the snap-in distance. Due to difficulties in precision alignment and the presence of other particle sizes in the AFM data, we estimate that the snap-in distance could vary by ± 20nm.

3.5 Results and Analysis

The results of the experimental measurement are shared and discussed below in comparison with the theoretical methods outlined above. A sphere-plane experiment is discussed first, to validate the methodology, given the availability of sphere-plane experiments in the literature for comparison. Following, we discuss the data collected for two-spheres.

3.5.1 Two-Sphere NFRHT

Figure 27 shows the average and range of thermal radiative conductances measured at each distance, compared with theoretical predictions. The SCUFF-EM computation results compared with the 2-sphere analytical extrapolation from Narayanaswamy et al.[23] so closely match that it is difficult to discern them when plotted together, as shown in section 3.2.3. The range of radiative thermal conductance values was found to be broad, with higher values positively correlated with delay time between successive studies (not shown).

These previous studies have also shown that the far-field component for two-spheres is underestimated by PFA calculation, but that component has been removed here, for analysis of only the near-field.

The predictions for the two-sphere study diverge by ~20% at the minimum distance studied and are qualitatively different in the 1-10 μm range. A majority of the temperature differential curves examined fall between these two predictions, with one approach aligning quite well with the SCUFF-EM prediction. We found that the average of all thermal conductances falls short of predictions, and the total range is large: ~1.1nW/K at 2 μm and ~1.7nW/K at 100nm. We hypothesize that measurements conducted in succession need significant time to fully allow the receiver sphere to cool in vacuum for accurate quantification of the temperature differential. For these studies, a minimum receiver cooling time of 30 minutes was used, however, a correlation between successive measurements and decreasing peak near-field heat flux was still observed . This may also illuminate the cause of previous sphere-plane

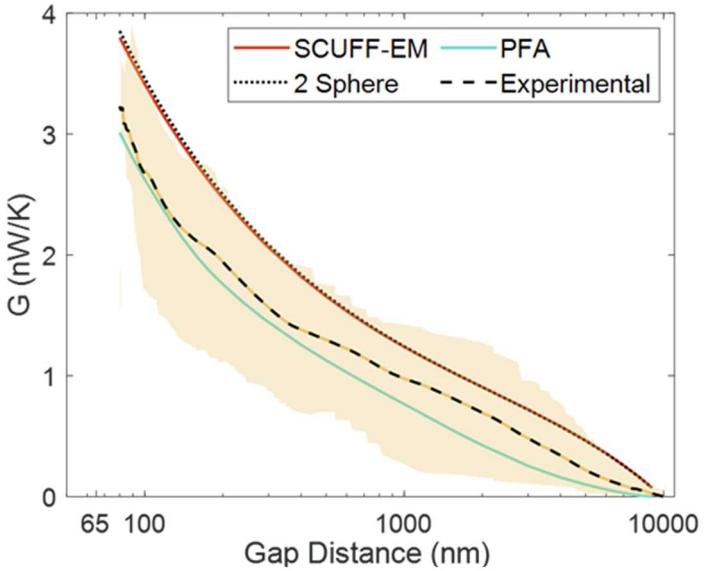

Figure 27: Analytical models of computational predictions, together with the PFA model and experimental data. The yellow highlighted area depicts the range of experimental data around the average.

studies with results below those expected from exact computations, particularly in studies using devices with very low thermal conductance.

These previous studies have also shown that the far-field component for two-spheres is underestimated by PFA calculation, but that component has been removed here, for analysis of only the near-field.

For this reason, Figure 28 shows the maximum conductance/flux measured at each temperature differential, as compared with the PFA and SCUFF-EM calculation.

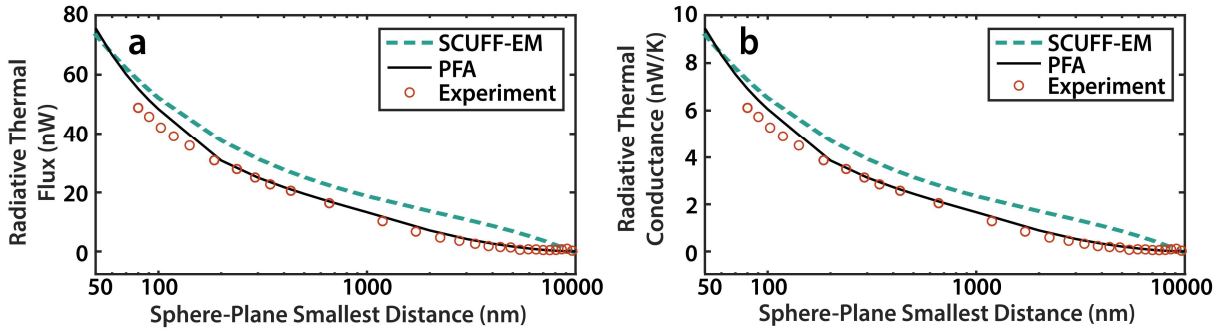

Figure 28: Comparison between experimental data and theoretical models for near-field radiative heat flux and conductance for the sphere-plane geometry. a) Thermal flux for the sphere-plane system. b) Sphere-plane conductance measurement.

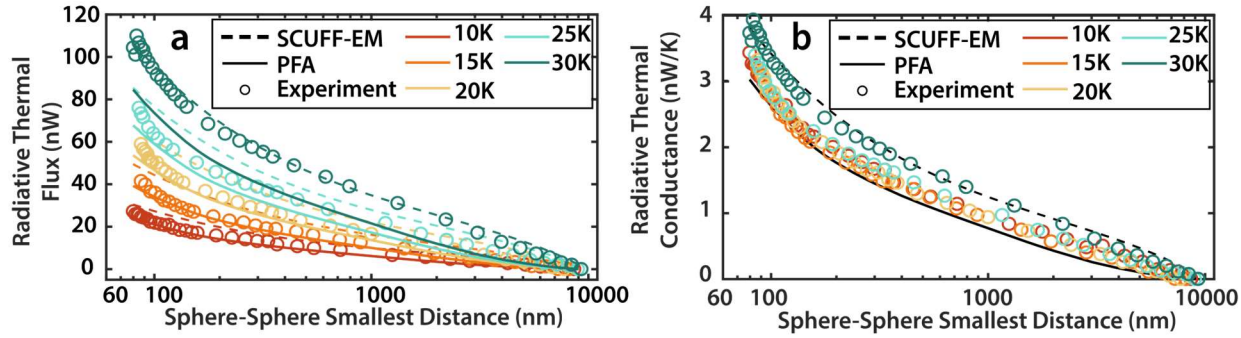

Figure 29: Comparison between experimental data and theoretical models for near-field radiative heat flux and conductance for two-sphere geometry. a) Temperature dependence of sphere-sphere measurement, for a 42 µm sphere and a 46 µm diameter sphere, showing a linear increase with increasing temperature. b) Temperature independent sphere-sphere measurement, showing clearer agreement with computational results.

3.5.2 Sphere-Plane NFRHT

The experimental result compared with the proximity force approximation and boundary element method calculations for a 40 μm sphere to an effectively infinite plane is shown in Figure 29. This study was conducted at a nominally 10 K temperature differential and has about twice the radiative thermal conductance of a two-sphere measurement conducted under the same conditions, as predicted by the PFA. We can see that there is not a large discrepancy between the PFA and the experimental results, although the PFA does slightly underestimate the radiation as predicted by our boundary element solution. The difference between the two theoretical predictions will be seen to not be as large as the two-sphere configuration, because the approximation is only applied to one side of the system.

3.6 Conclusions

In order to achieve a more complete understanding of super-Planckian radiative heat transfer it is essential to perform experimental investigations of NFRHT from a diverse range of materials and geometries. Until now, studies on near-field radiative heat transfer (NFRHT) have primarily concentrated on sphere-plane (i.e., a sphere and a plane separated by a nanoscale gap) and plane-plane (i.e., two plane parallel surfaces separated by a nanoscale gap) configurations. However, practical applications may necessitate the consideration of different designs, including curved surfaces.

We have presented an experiment that systematically explored NFRHT between two spherical surfaces. In order to accomplish this challenging measurement, I utilized custom probes that were developed previously in my group that were capable of detecting heat flows with nanowatt resolution using platinum resistor thermometers embedded in the calorimetric probe. To perform the desired experiments smooth silica spheres (~40 μm diameter) were first integrated into these probes to create the cold body, or receiver device. For the emitter, a second

body was created, which consists of a planar silicon device into which a smooth silica sphere was integrated, and which could be independently heated in a controlled manner via embedded heating and sensing resistors on the thermally-isolating capillary tubes.

We probed the NFRHT between the two silica spheres by embedding the emitter and receiver devices into a custom-built nanopositioner (with six degrees of freedom) that enables both relative alignment of the two spheres as well as control of the gap size between them. We measured the heat flow between the two spheres when the emitter was heated by ~10-30 K above the receiver temperature and the gap size between the spheres was systematically reduced from ~5 μm to 10s of nm. During this process a significant enhancement was observed, increasing ~15-times as the distance is varied from 5 μm to 80 nm. The peak value in the measured thermal conductance (i.e., when the gap size is smallest, at 80 nm) was ~3.82 nW/K. It is to be noted that, as expected from the theory of fluctuational electrodynamics, this measured value is approximately two orders of magnitude lower than the predicted value for plate-plate heat transfer between two circular silica plates with a diameter of 40 μm but was still successfully measured with the high-resolution calorimetric probes. I note that the measured, lower sphere-sphere near-field thermal conductances are expected and in excellent agreement with numerical simulations performed using fluctuational electrodynamics.

The presented data validate the suitability of boundary-element method calculation for predicting the maximum heat flux between two spheres with high accuracy. We note that the popular proximity-force approximation is of use qualitatively, particularly below a distance of 2 μm, in which regime the criterion r >> d holds true. However, the PFA underestimates the maximum thermal conductance by ~20% and must be adjusted for a quantitative prediction. This range of best usage for the PFA is notable, due to the high time requirement for calculation in this regime

for more accurate methods. A combined prediction strategy is recommended for calculation of the expected NFRHT between two 10's of micron scale, highly-curved surfaces.

3.7 Contributions

The results presented in this chapter were produced with collaboration from my colleagues. Z. Wang made the top holder and led sphere mounting. I fabricated the bottom device and bottom holder. J.W. Lim assisted me with troubleshooting the experiment. K. Panda prototyped device holder configurations. Y. Luan fabricated the top probe. A. Majumder completed the SCUFF-EM analysis. I conducted the experiments and PFA analysis. The work was conceived by E. Meyhofer and P. Reddy.

Chapter 4 NFRHT in Two-Dimensional Material-Mediated Systems

4.1 Introduction

Graphene was first separated from bulk graphite using mechanical exfoliation via scotch tape in 2004[78]. This was possible because only Van der Waals forces bind together adjacent sheets of graphene in graphite, and because the choice of substrate for this separation attempt (~300nm SiO_2 on Si) made possible optical recognition of monolayer flakes due to optical interference. Extraordinary properties of the two-dimensional "honeycomb lattice" structure[79] have been predicted since the first postulate of its existence within graphite[80], but it had been presumed to be a purely academic material due to instability relative to other carbon allotropes[81]. The authors of this groundbreaking paper demonstrated one of the highly anticipated features of graphene, very high room temperature carrier mobilities up to 10,000 cm/V-s.

Not long after, the same group verified other exciting electronic properties of graphene[82], such as demonstrating that charge carriers in graphene are quasiparticles called Dirac fermions with an effective mass of zero, traveling at the Fermi velocity 10^6 m/s. It was also shown in this work that the conductance of graphene is quantized, with a minimum nonzero value. This minimum conductance value is observed when the Fermi level of graphene is brought to the Dirac point, a point which can be described either as a semiconductor bandgap of zero or as a semi metallic overlap of zero.

As discussed in the introduction, graphene is the real material with the closest fit to the ideal NFRHT limit in a computational study of two-dimensional and three-dimensional

materials[45]. Graphene has also been proposed as a material for thermal rectification with high potential for large tuning ratios or when paired with other complementary materials[29,51–54]. Unfortunately, existing experimental studies[57–60] have been conducted at fixed distances and with few data points for changing Fermi levels. Additionally, the Fermi level has previously been estimated on the basis of matching with the radiative thermal conductance measured, rather than calculated with the input gate capacitance and a known Dirac point.

4.1.1 Tunable NFRHT using Two-Dimensional Materials

A nascent technology at this time is thermal control through electrically-analogous devices, such as thermal switches and diodes. These thermal control devices have broad application potential in providing solutions in some of the key fields of our day, including in heating and cooling, data storage, and heat management in electronics[83]. Super-Planckian radiative heat transfer offers one route of tunable heat transport devices, through a variety of mechanisms.

4.1.1.1 Tuning NFRHT Mechanically

A good deal of the ideas for thermal modulation or active thermal switching is some type of movement of one of the involved bodies. For example, highly doped silicon, which is inexpensive and supports plasmonic modes in the infrared regime[84,85], can add a strong near-field enhancement at distances less than 100 nm. This material system can be strategically tuned in advance via the doping of the silicon bodies. Such a technique has been demonstrated as an effective thermal rectifier[20], which could also be used as a thermal switch by moving the bodies apart to switch the radiation “off”. The percent change between modes is dependent on the minimum vacuum gap achieved and the “off” position chosen, but as a limiting example we may choose a minimum gap on the order of 10’s of nanometers, and a movement to 100 nm gap size,

which the authors of [20] predict analytically would have a two order of magnitude decrease in the radiated heat flux.

There has been an experimentally demonstrated strategy for modulation of near field heat transfer between two, three-dimensional bodies by controlling the distance of a third, mediating body. This multi-body effect strategy is predicted to be capable of up to a 5 times switching ratio, and is effective even in the far-field case[86].

A system consisting of materials with radiative heat flux that is highly directional could be expected to have very effective thermal switching with rotation of one body, disrupting the alignment necessary for a high level of heat transfer. Some two-dimensional materials such as hBN[87], black phosphorus[88], and nano-structured graphite[89] support directional hyperbolic surface modes, which would enable such a highly directional heat transfer. Patterning can also be critical. In a study that further examines the impact of patterning hBN into nanoparticles, the on/off ratio can be as high 1500[90], a ratio which is in contrast with hyperbolic planar films or a nanostructured grating of nondirectional material, with ratios of 12.46[91] and 2[92], respectively.

4.1.1.2 Tuning NFRHT Statically

It is in the interests of optimal switching to consider options that do not require movement as well. Each proposed technique has pros and cons, and these methods may be preferred in some applications, for example for durability of parts. Also, it is possible to combine both, such that the transfer is reduced synergistically.

One such option is to change the temperature of a surface made up of a phase changing material, such as VO_2. VO_2 can support much larger NFRHT in the insulating phase than in the metallic phase. One way this can be used is in conjunction with other materials, such as highly-doped silicon[93]. In a completely VO_2-based system, computations lead to the conclusion that the

near-field radiative heat transfer can be reduced by 80% at sub-30-nm vacuum gaps or 50% at 1 μm, using the phase change capability of the material[94].

Finally, we can alter the optical properties of the material of emitter and/or receiver by applying an external electric or magnetic field. This option may be faster than modulation using a phase-change material because there is no thermal inertia. In one study, the NFRHT is tuned by 16.5% using an external magnetic field, which impacts the surface phonon polariton modes of the chosen ferroelectric system[95].

The electric-field tunable plasmonic response of graphene offers another solid-state thermal switching method in the near-field regime. This capability can be exploited in suspended graphene, which is commonly used in simulation due to the removal of substrate effects on the dielectric function of graphene. Alternatively, we can consider graphene in conjunction with another material that would be a suitable substrate for an application. An analytical work by Ilic et al does both, predicting a switching ratio for graphene on SiC of up to 40 at a 25nm distance and for very high carrier concentration of graphene[96].

Separately and for more moderate carrier concentration values, graphene on SiC has been theoretically predicted to have a switching ratio at 100nm of about 2.5. This paper also exemplifies the idea of combining electric field tuning with a motion based method. The movement from a 10nm vacuum gap to a 100nm vacuum gap causes a ~100X decrease in the heat transfer coefficient. Combined with the electric field switching ratio, this represents ~250X switching ratio[97]. Similarly, the twisting method for anisotropic systems mentioned before could be employed using graphene gratings, as explored here[98], but with the addition of electric field tuning the graphene strips.

In the following section, we predict the tunability of an SiO2 system mediated by one-sided application of graphene, towards a graphene-based thermal switching device.

4.1.2 Key Questions

In this chapter, I propose a study to answer the following questions:

- How can a second Fermi level estimate be added to graphene-mediated NFRHT measurements?
- Can electric field tuning via the dielectric function of graphene produce a measurable change in the NFRHT between two silicon dioxide samples?

4.2 Modelling Two-Dimensional Materials for NFRHT

Planar structures with two-dimensional materials can be modelled using the semi-analytical equation discussed in section 1.2, with some adjustments. First, the Fresnel reflection coefficients are calculated differently for layers of extreme thinness. While a bulk two-layer system was explained previously to have the reflection coefficient calculated according to[58]:

$$r_{il} = \frac{r_{ij}+r_{jl}e^{2ik_{zj}t_j}}{1-r_{ij}r_{lj}e^{2ik_{zj}t_j}}, \text{where } \begin{matrix} j = i+1 \\ l = i+2 \end{matrix} \quad \text{Eq. 38}$$

$$r_{im} = \frac{r_{il}+r_{lm}e^{2ik_{zl}t_l}}{1-r_{il}r_{ml}e^{2ik_{zl}t_l}}, \text{where } m = i+3 \quad \text{Eq. 39}$$

In these equations, *i* is the vacuum gap layer. For a three-layer system with graphene as the top layer, the formulas for the reflection coefficients would instead be [58]:

$$r_{il,s} = \frac{r_{ij}+r_{jl}(1+r_{ij}+r_{ji})e^{2ik_{zj}t_j}}{1-r_{ij}r_{lj}e^{2ik_{zj}t_j}} \quad \text{Eq. 40}$$

$$r_{il,p} = \frac{r_{ij}+r_{jl}(1-r_{ij}-r_{ji})e^{2ik_{zj}t_j}}{1-r_{ij}r_{lj}e^{2ik_{zj}t_j}} \quad \text{Eq. 41}$$

$$r_{im} = \frac{r_{il}+r_{lm}e^{2ik_{zl}t_l}}{1-r_{il}r_{ml}e^{2ik_{zl}t_l}} \quad \text{Eq. 42}$$

This is the format used for the example configuration of graphene on a thin film of silicon dioxide on bulk silicon. Rather than considering the thickness of single or few atom-thick materials, we treat these materials as a modification to their substrate's reflection properties, modelling them as an additional source of dipole oscillators on the surface.

4.2.1 Conductivity and Dielectric Function of Graphene

The dielectric function of graphene can be constructed from its complex conductivity, such that:

$$\epsilon = 1 + \frac{k_z \sigma}{2\epsilon_0 \omega} \quad \text{Eq. 43}$$

For suspended graphene. Towards calculating the conductivity of graphene, two methods are presented and compared. The first method, by You-Chia Chang et al[99], also provides experimental data for comparison.

The equation for conductivity as a function of frequency calculated in this work from non-linear response theory is:

$$\sigma = \sigma_{interband} + \sigma_{intraband} \quad \text{Eq. 44}$$

$$\sigma_{interband} = \frac{\sigma_0}{2}\left(\tanh\frac{\hbar\omega+2\mu}{4k_BT} + \tanh\frac{\hbar\omega-2\mu}{4k_BT}\right) - \frac{i\sigma_0}{2\pi}\log\left[\frac{(\hbar\omega+2\mu)^2}{(\hbar\omega-2\mu)^2+(2k_BT)^2}\right] \quad \text{Eq. 45}$$

$$\text{(Drude) } \sigma_{intraband} = \frac{i4\sigma_0}{\pi}\,\frac{\mu}{\hbar\omega+i\hbar\tau} \quad \text{Eq. 46}$$

$$\sigma_0 = \frac{e^2}{4\hbar} \quad \text{Eq. 47}$$

μ is the Fermi level of graphene (277 meV), and τ is the damping constant (54 meV).

The complect optical conductivity measured in this paper is shown in Figure 29, which was used also to obtain the Fermi level and damping constant.

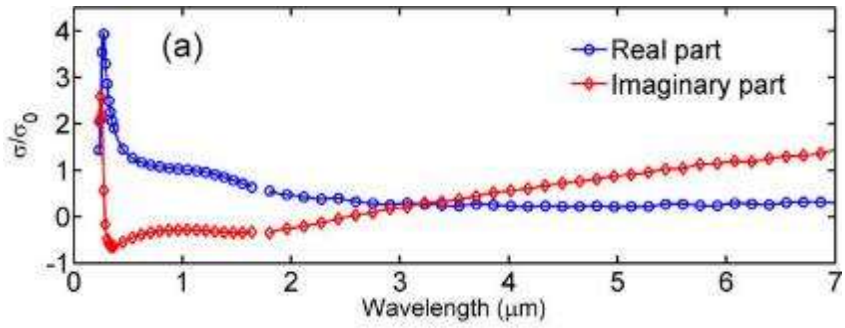

Figure 30: The extracted optical conductivity of a monolayer CVD graphene sample. Figure copied with permission from reference 99.

The second calculation used is from Ilic et al, in a paper on the plasmonic functions of graphene[100]. Other reproduced images from this work were also calculated (not shown) for validation of the simulation process. Both of the simulations for conductivity are shown in Figure 30.

$$\text{(Drude) } \sigma_{intraband} = \frac{i\sigma_0}{\omega+\frac{i}{\tau}} \frac{8k_BT}{\pi\hbar} \ln\left[2\cosh\frac{\mu}{2k_BT}\right] \quad \text{Eq. 48}$$

$$\sigma_{interband} = \sigma_0[G\left(\frac{\hbar\omega}{2}\right) + i\frac{4\hbar\omega}{\pi}\int_0^{\infty} \frac{G(\mathcal{E})-G\left(\frac{\hbar\omega}{2}\right)}{(\hbar\omega)^2-4\mathcal{E}^2} d\mathcal{E} \quad \text{Eq. 49}$$

Where:

$$G(\mathcal{E}) = \frac{\sinh\left(\frac{\mathcal{E}}{k_BT}\right)}{\left[\cos\left(\frac{\mu}{k_BT}\right)+\cosh\left(\frac{\mathcal{E}}{k_BT}\right)\right]} \quad \text{Eq. 50}$$

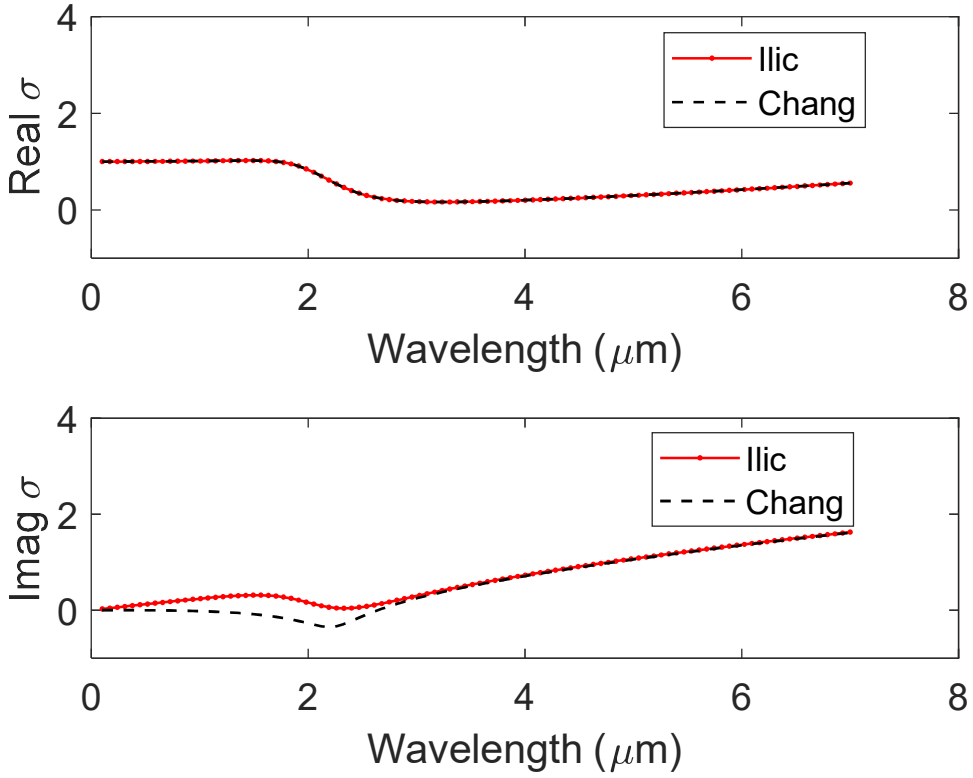

Figure 31: Simulated real and imaginary graphene conductivity for μ=277 meV and τ = 54 meV.

Both methods show excellent agreement with each other and with the experimental data. Either is suitable for use in calculating the conductivity of graphene for use in NFRHT simulations.

4.2.1.1 Impacts of Substrate on Dielectric Function of Two-Dimensional Materials

If the desired solution method involves representing a two-dimensional material of infinitesimal, but non-zero thickness, rather than the surface-current method with altered reflection coefficient calculation, the substrate screening effects on the dielectric function of the two-dimensional material should be considered in addition to the conductivity. For a two-dimensional material between two bulk materials:

$$\epsilon = 1 + \frac{k_z \sigma}{2\epsilon_0(\epsilon_1+\epsilon_2)\omega} \qquad \text{Eq. 51}$$

Where the two dielectric functions from the substrates are denoted with separate subscripts. In the case that both sides are vacuum or air, the equation simplifies back to the original equation for suspended graphene.

4.2.2 Theoretical predictions of tunability in the SiO_2-graphene/SiO_2 system

These methods allow us to make predictions for the NFRHT of different systems using graphene on one or both sides as a mediator. Existing works in the literature regarding electric-field tunability of near-field radiative heat transfer devices with graphene are promising but have not yielded high ratios of tunability or explored a wide range of applied biases and distance gaps. Here, we consider the possibility that a higher ratio of tuning is yet possible using computational predictions, which we will seek to compare in 4.4 to our experimental results.

4.2.2.1 Graphene Plasmonics for NFRHT

An encouraging route of NFRHT tunability for a graphene device is plasmonic tuning through electric-field gating. Plasmonic tuning is possible in highly-doped silicon systems[101], and the plasmonic resonance of noble metals may be chosen in advance via shaping[102], but two-dimensional materials are unusually easy to tune because the single layer is fully in contact with the gate. Graphene is also notable in the plasmonics field for its ability to support plasmons from mid-infrared to terahertz regimes[103,104], whereas other materials are limited to smaller ranges.

An applied electric field changes the doping level of the graphene layer, creating more or fewer free carriers in the graphene. The plasmonic resonance frequency of a material is proportional to its carrier density. We can observe this in the case of graphene, as we can calculate the poles of the dielectric function at which a plasmonic resonance is expected by setting the permittivity equal to 0, such that:

$$\epsilon = 1 + \frac{k_z \sigma}{2\epsilon_0(\epsilon_1+\epsilon_2)\omega} \rightarrow \omega_p = -\frac{k_z \sigma}{2\epsilon_0(\epsilon_1+\epsilon_2)} \quad \text{Eq. 52}$$

$$\omega_p \propto \sigma = ne\mu \rightarrow \omega_p \propto n \quad \text{Eq. 53}$$

Where μ in this case is the mobility of graphene, rather than the Fermi level.

The dispersion relation for plasmons in graphene with a damping constant $\tau = 1e-13$ Hz and Fermi level $\mu = 0.5\ eV$ is shown in Figure 31. We can see that a broad range of frequencies are supported for plasmons over a range of wavevector values parallel to the graphene plane.

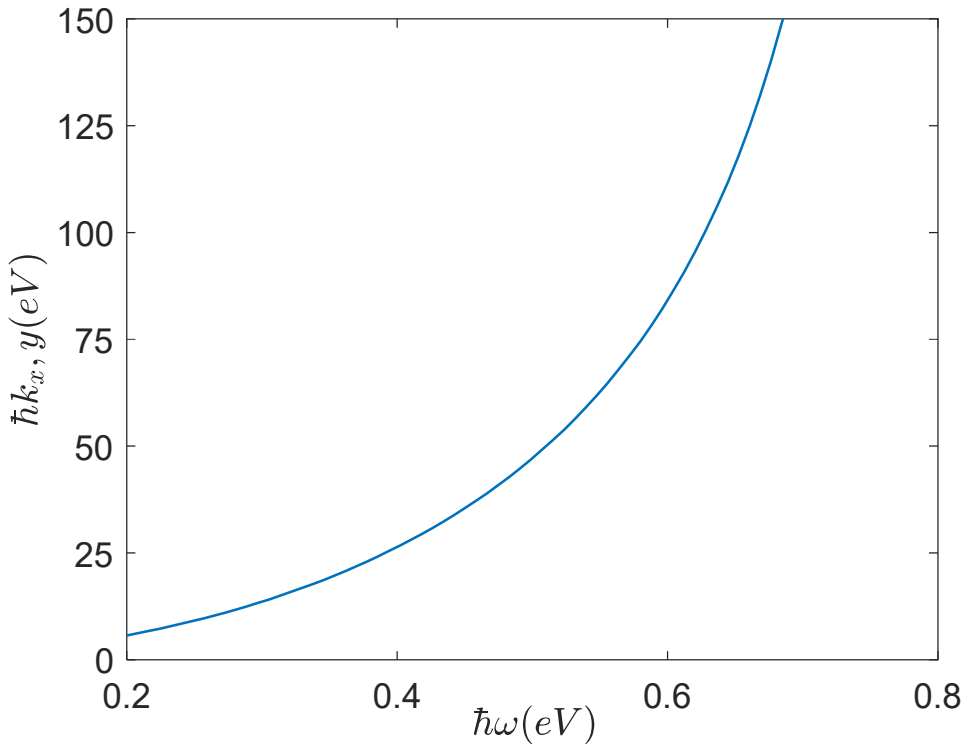

Figure 32: Graphene dispersion relation.

As a consequence of shifting the Fermi level of graphene and changing the plasmonic resonance frequency, we will also change the reflection coefficient at the vacuum-graphene/SiO_2. We can see the impact this has on the real and imaginary reflection coefficients for three different Fermi levels shown in Figure 32. The impact of the graphene conductivity on the reflection coefficient is increased as the Fermi level is raised, as the plasmonic effect is

stronger for a higher carrier concentration. This is only the reflection coefficient for a single wavevector chosen as an example, however, and does not make up the full picture alone.

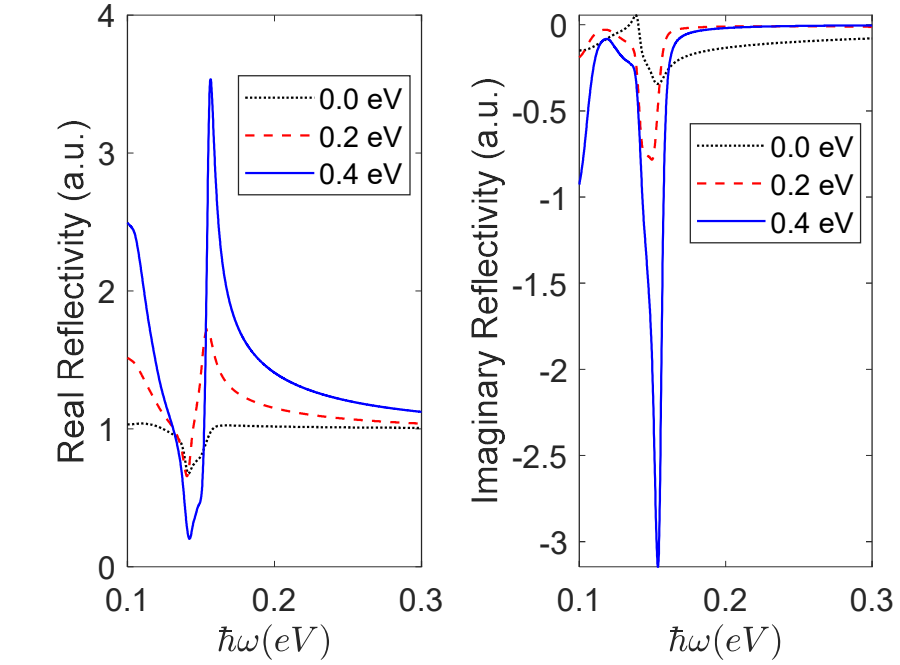

Figure 33: Tuning reflectivity of the SiO_2 surface with graphene plasmons

4.2.2.2 Graphene-Mediated NFRHT in an SiO_2 System

The highest NFRHT between materials with peaks in the dielectric functions occurs when these peaks are aligned in the frequency domain. The spectral heat transfer between an SiO_2 surface and graphene on an SiO_2 substrate is shown in Figure 33 for varying values of the Fermi level of graphene. The change in carrier concentration shifts and broadens the plasmonic resonant frequency of the graphene layer, causing the maxima of the spectral heat transfer to shift away from the frequencies of the original SiO_2-characteristic peaks.

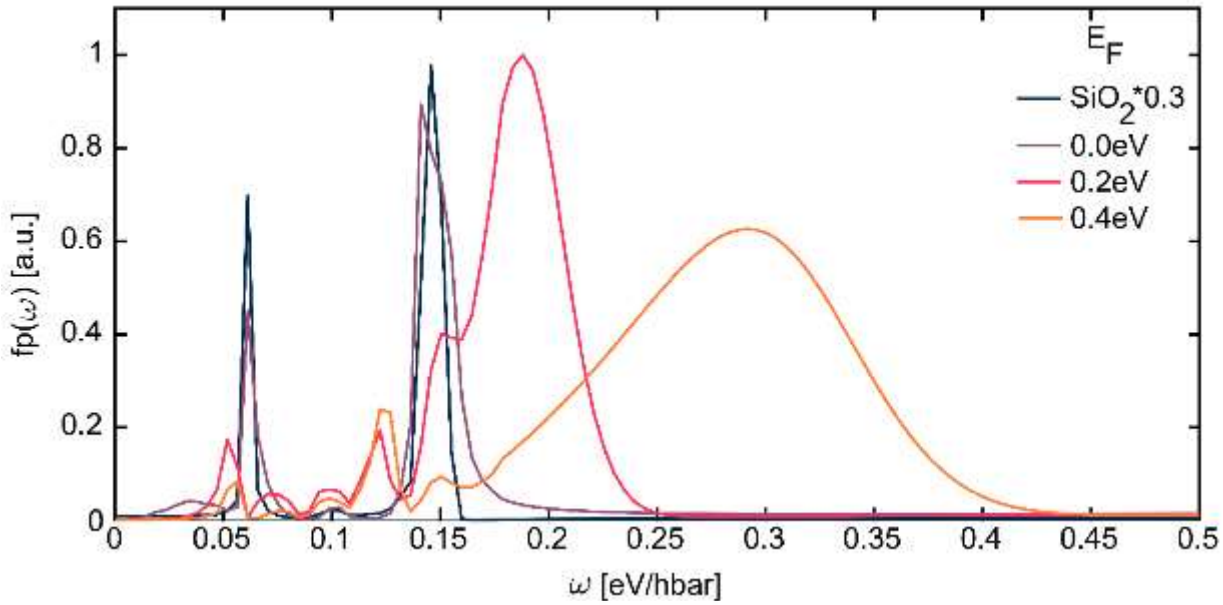

Figure 34: Simulation results for the spectral heat transfer of SiO_2-Graphene/SiO_2/Si at a 10nm distance. The spectral heat transfer is also plotted for a fully SiO_2 system, for comparison. It can be seen that increases in the Fermi level of graphene shift and broaden peaks of the function, resulting in a lower total heat transfer coefficient at this distance.

This change results in differences in the thermal conductance of the system, which are distance-dependent. Because plasmons have relatively short wavelengths[105], the effect is most noticeable around 100nm and continues to grow stronger as the distance reduces. Figure 34 shows the predicted transmitted power between an SiO_2 sphere and graphene on a 285nm SiO_2/Si substrate for varying Fermi levels of the graphene layer for 10K difference in temperature. The change is quite strong at an aspirational gap distance of 10nm, with a halving of the power anticipated for a significant change in the Fermi level. At a more realistic distance of 30nm, the decrease is ~30%.

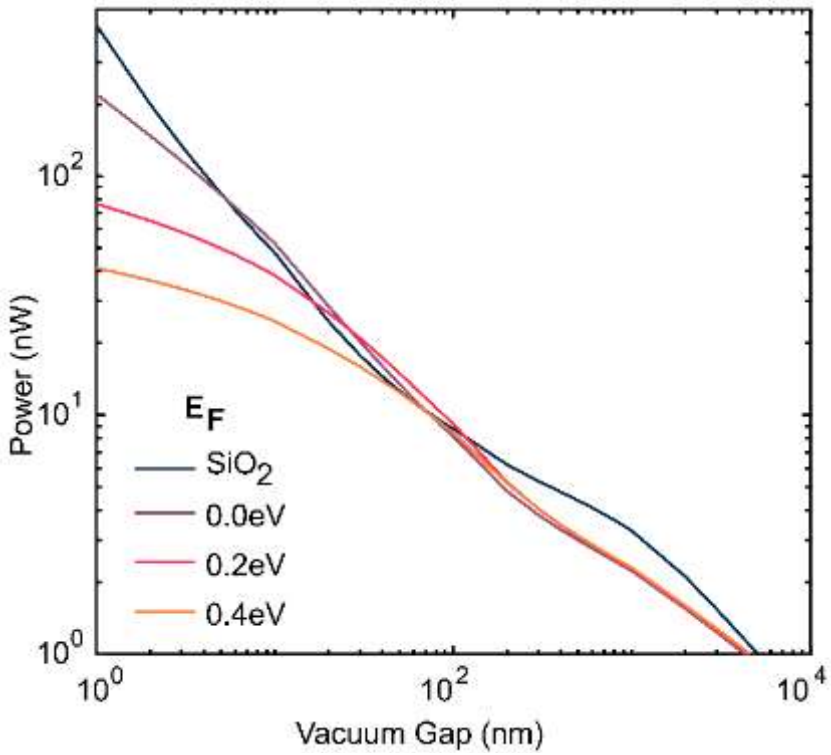

Figure 35: Simulated power transfer between a silica sphere and a graphene-coated SiO_2/Si substrate for a 10K temperature difference. A decrease is seen at 10s of nm gap sizes for any doping level of graphene compared to the pure SiO_2-SiO_2 transfer. A maximum switching level of 64% is predicted, with decreasing but still substantial switching ratios possible for more realistic gaps.

4.3 Experimental Configuration

The experimental configuration is largely similar to that described in section 3.3, with the exception that the bottom device, still the heated body or emitter, consists of a graphene on 300nm silicon dioxide, backgated field-effect transistor. A few additional connections exist for this reason, the graphene strip is contacted on either side to provide a source and drain contact for electrical characterization, and there is a double-bond to the backgate through a via etched in the oxide and the backside of the sample. A three-dimensional diagram of the layout for this configuration is shown in Figure 35.

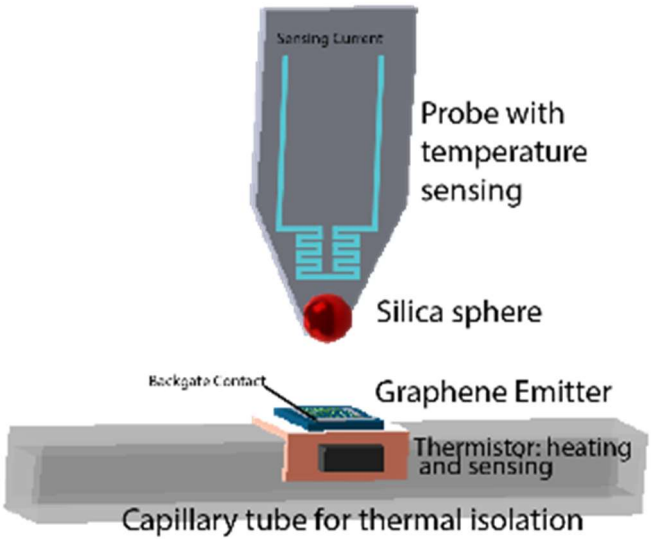

Figure 36: SiO_2 sphere-graphene/SiO_2 plane experimental configuration

4.3.1 Emitter (Bottom) Device

The emitter for this experiment differs primarily from the setup used for chapter 3 in the need for three additional connections on the emitter device. These connections serve to permit backgating of the field-effect graphene device and detect the conductivity change during electrical characterization. The source and drain contacts also frame the graphene strip, making alignment easier. A microscope view of a ~2.5X2.5 mm chip is shown in Figure 36.

The electrical connections for the bottom device were limited by availability of connections exiting the vacuum. As a results, the source, heating thermistor ground, and sensing thermistor ground shared a bond and were connected to the outputs via the electrical contacts at the top of the device. Source, drain, and backgate connections were made to the device on the device-side using wirebonding, and on the capillary side using silver paste. All connections were tested for high conductivity before beginning the measurements.

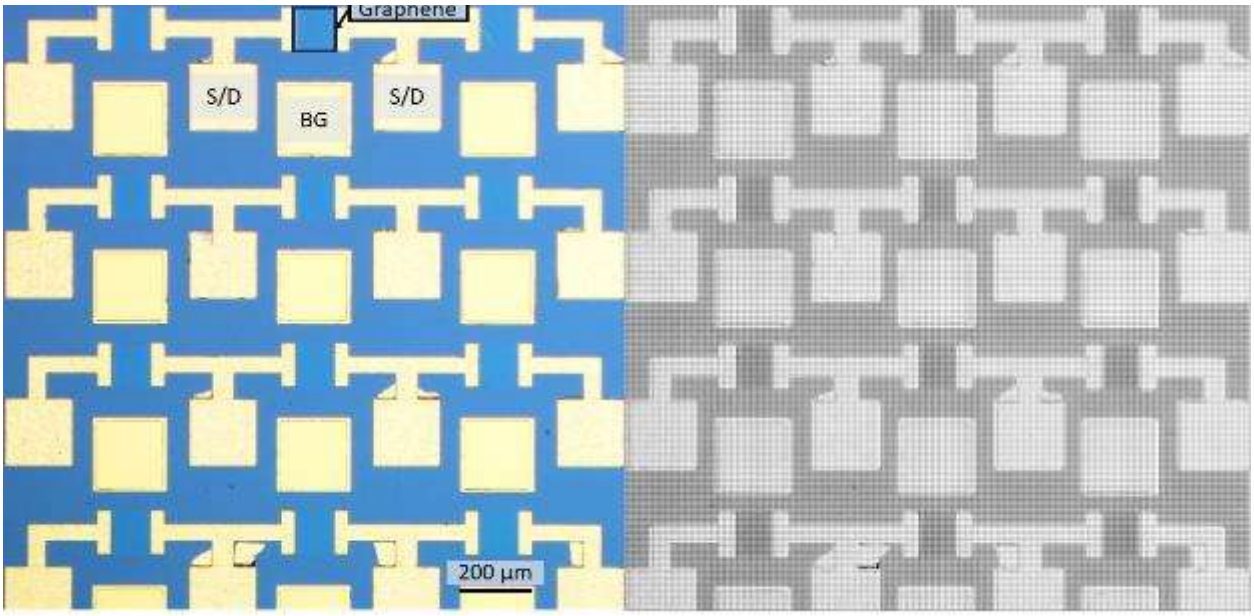

Figure 37: Microscope image of graphene device, with labels. Left: S/D indicates contacts that can be used as source or drain, they are symmetric. BG denotes the backgate contact, and the label graphene marks the active, graphene-coated area of this device. Right: a grayscale version of this image, selected in contrast and binning such that the graphene-to-substrate contrast would appear sharper, for colorblind accessibility.

4.3.1.1 Fabrication of the Graphene Emitter

Fabrication of the graphene devices was completed as follows. (1) To begin, due to availability, a lightly p-doped silicon wafer with 500 nm silicon dioxide was (2) wet-etched back to 300 nm thickness using a buffered hydrofluoric acid solution. The thickness of the remaining oxide was verified using the Nanospec ellipsometer (within 5 nm). (3) Next, access was gained to the silicon underlayer by etching areas of the silicon dioxide film using a C_4F_8 reactive-ion etch chemistry. Elimination of the oxide was confirmed, again with the Nanospec ellipsometer. With the same lithography mask, 100 nm of aluminum was deposited in the etched area as a backgate contact pad. (4) Chrome/gold wirebond pads were deposited at 5/300 nm thickness, both for wirebonding to the source, drain, and gate contacts, and also to cover the aluminum backgate pad for piranha cleaning. (5) A thinner chrome/gold deposition of 3/50 nm was used for contacting the graphene before piranha cleaning. (6) Graphene was then prepared and transferred onto chips

using a standard wet transfer process[106].and the graphene shape was etched using traditional photolithography methods and an oxygen etch chemistry. A diagram of the fabrication steps is shown in Figure 37.

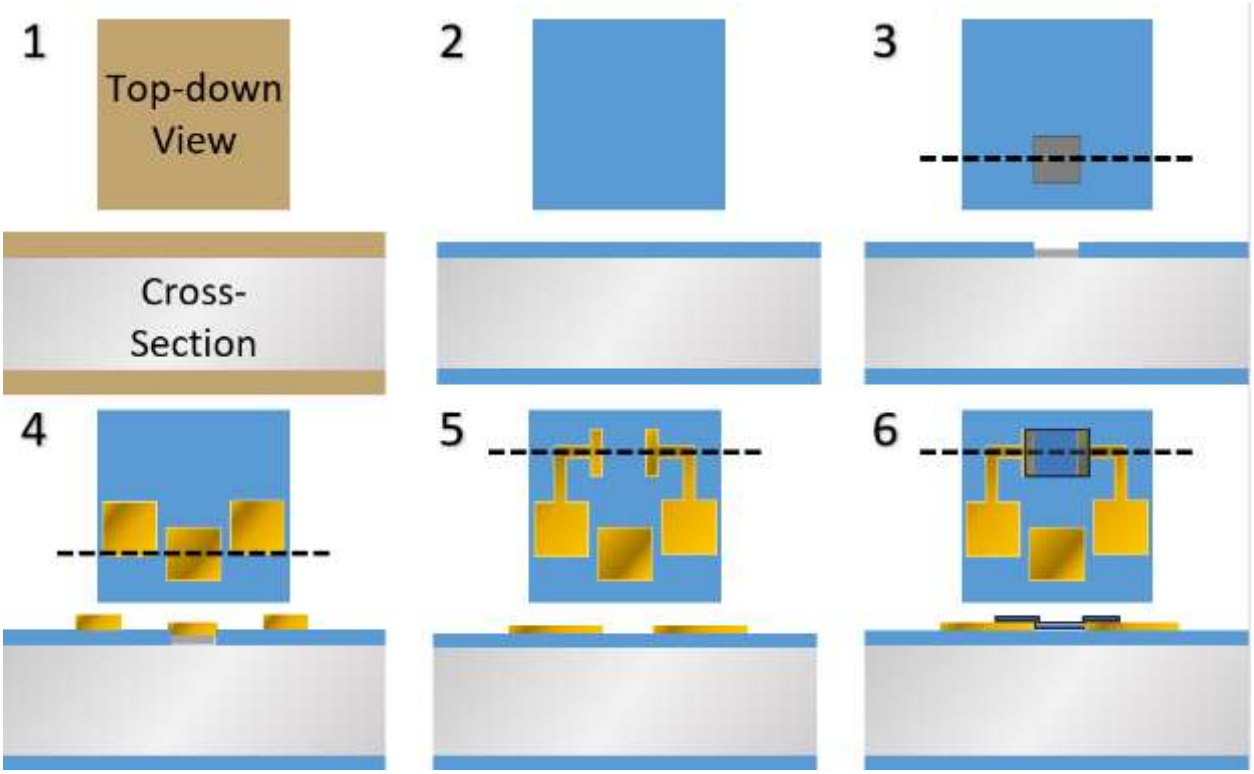

Figure 38: Graphene device fabrication diagram.

4.3.1.2 Electrical Characterization of the Graphene Emitter

The graphene samples were first characterized as electrical devices. The backgate was swept between ±130V while a resistance measurement was taken across the source and drain. From this data, a conductivity curve was obtained (Figure 38), yielding estimates of the Dirac point and the mobility. The Fermi level is calculated in the conventional way, by considering the Dirac point equal to 0 eV and predicting the shift from there using the expected capacitance to calculate the change in work function. This shows that it is possible to independently measure the anticipated Fermi level of graphene, as discussed in 4.1.2, enabling a new level of certainty in comparisons to measured NFRHT.

For a 300nm silicon dioxide layer, we can calculate the carrier density, which changes linearly in this region with the backgate voltage:

$$n(V_{BG}) = \frac{Ctot}{q} \cdot (V_{BG} - V_{Dirac}) = \frac{\epsilon_r \epsilon_0}{t_{ox} q} \cdot (V_{BG} - V_{Dirac}) \quad \text{Eq. 54}$$

$$\frac{\Delta n}{\Delta V_{BG}} = 7.1840e10\ /cm^2/V \quad \text{Eq. 55}$$

The Fermi level is linked to the carrier density with a square root relationship, with v_F, the Fermi velocity, known to be 1.1e6 m/s in graphene:

$$E_F = \hbar v_F \sqrt{\pi n} = 3.44e-2 \cdot \sqrt{(V_{BG} - V_{Dirac})}\ eV \quad \text{Eq. 56}$$

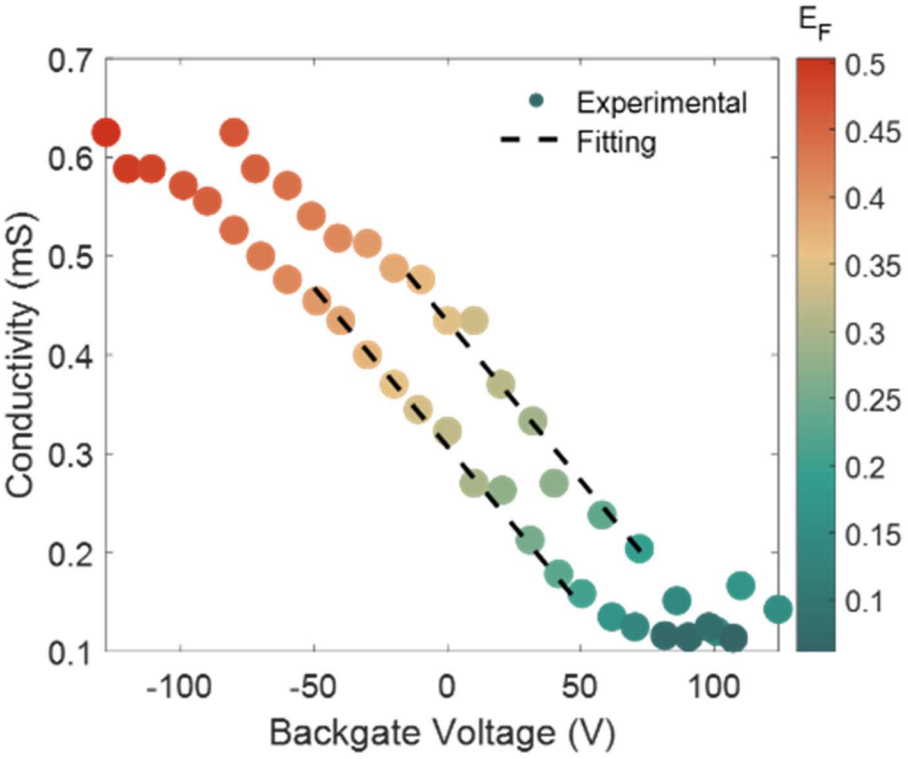

Figure 39: Measured conductivity versus backgate voltage for a representative graphene sample. The estimated Fermi level of each point is indicated by color code. The fitting line shows the lines used to extract mobility characteristics from these data. The linear region is used for the calculation and the hysteresis is adjusted before averaging the curves.

4.3.2 Receiver (Top) Device

The receiver sphere (70 µm diameter) is fixed to the tip of a probe, similar to those used in other studies[68] and discussed in further detail in section 2.3.2, which is mounted to the top of a custom-built nanopositioner[66], outlined in section 2.3. An SEM image is shown in Figure 39.

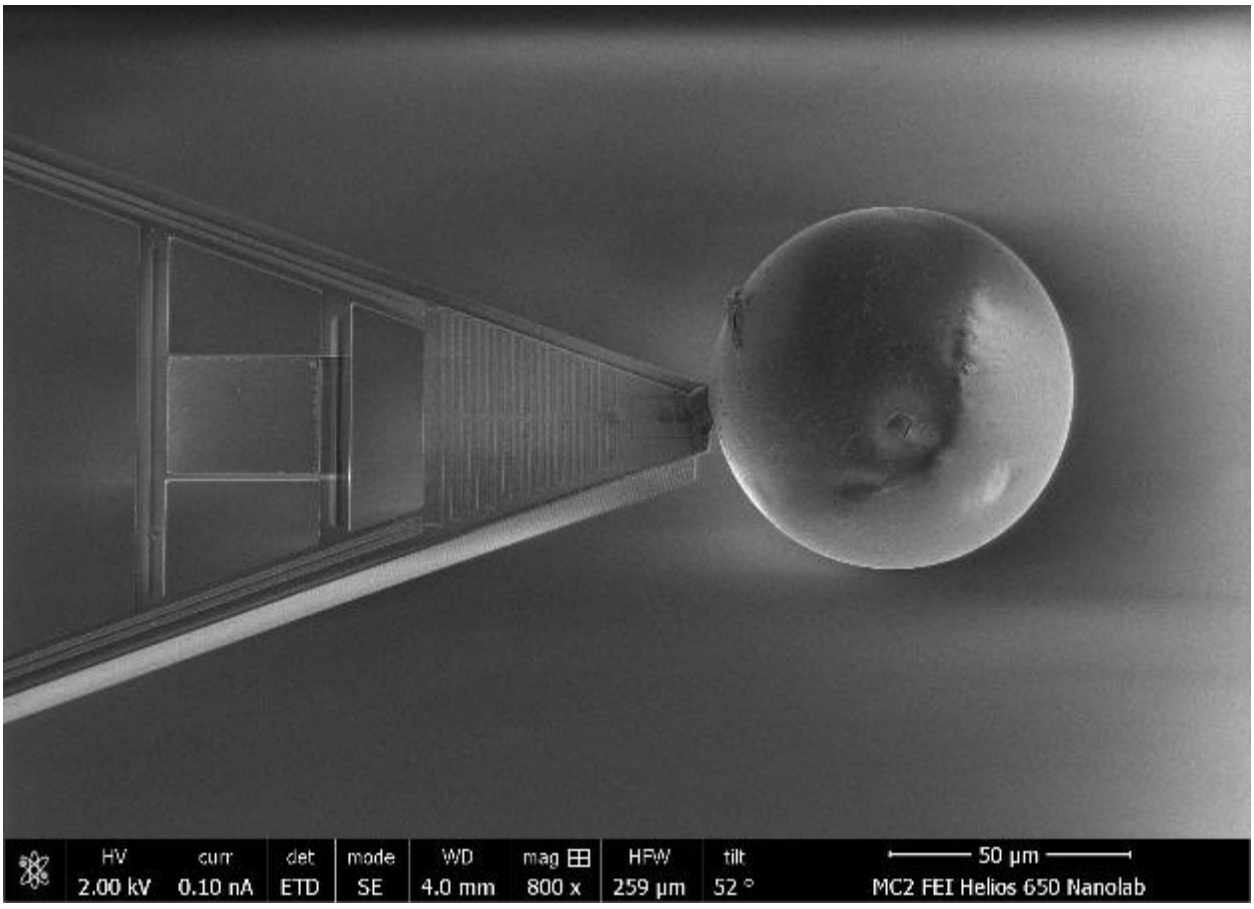

Figure 40: SEM image of receiver probe for graphene experiment.

4.3.2.1 DC Thermal Conductance

The receiver probe has a DC thermal conductance is ~0.4 µW/K and is the same design and fabrication batch as the probe from the two-sphere experiment.

4.3.2.2 Self-Heating of the Receiver

Self-heating at 10 µA, 1 Hz AC sensing signal input is anticipated to be ~1.2 K and is the same design and fabrication batch as the probe from the two-sphere experiment.

4.3.3 Alignment of Silica Sphere over Graphene Sample

An image of the graphene sample under 50X magnification in dark-field was taken to determine the cleanest region of the chosen sample, as shown in Figure 40.

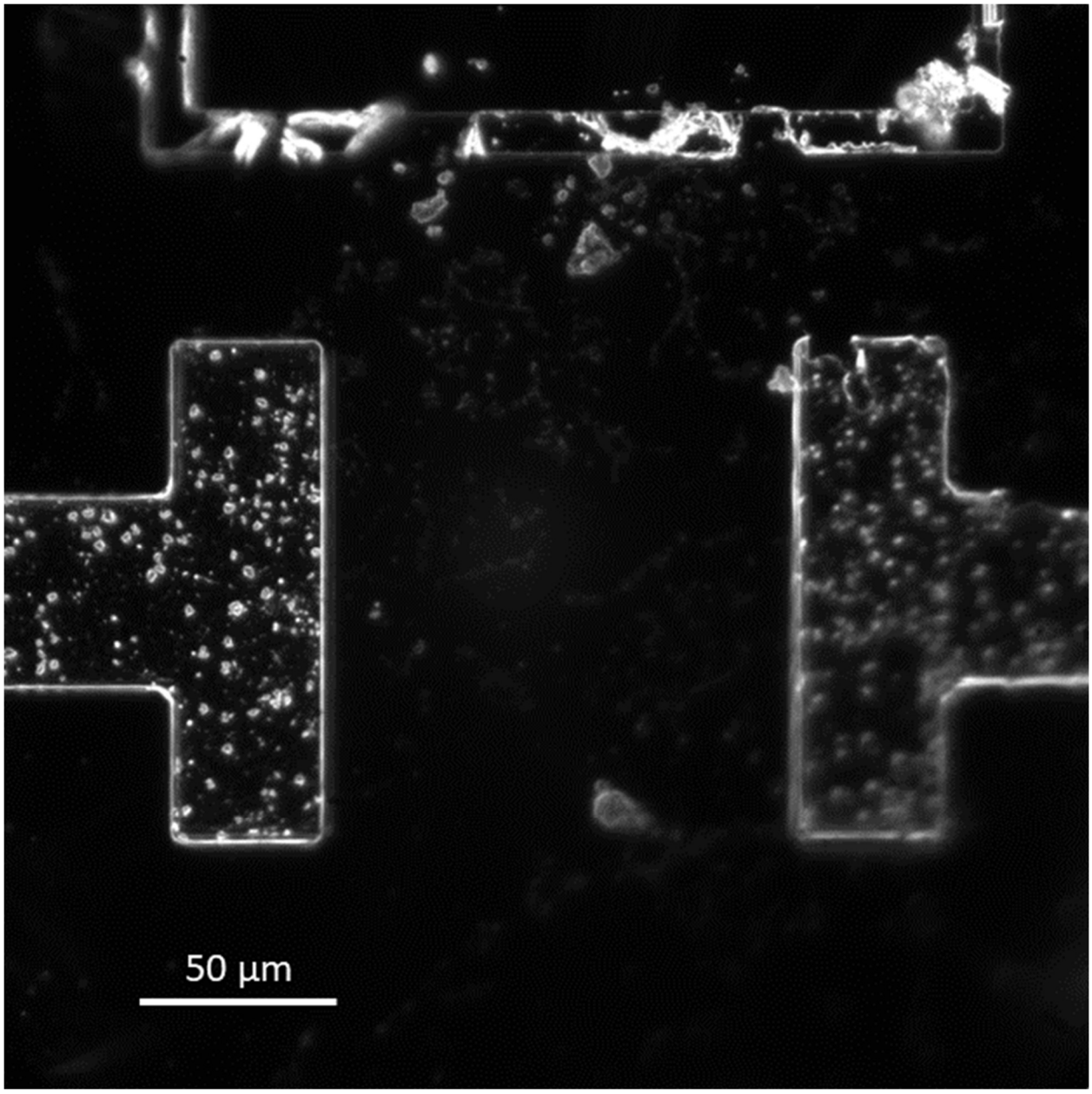

Figure 41: Dark field image of a single graphene device. An apparent large contaminant is present in the bottom right corner, which should be avoided during alignment.

Subsequently, the 10X magnification objective lens was used to center the receiver sphere, and a mechanism similar to that of 3.3.3 was used to position the sphere over the preferred area of the graphene sample. Alignment images are shown in Figure 41.

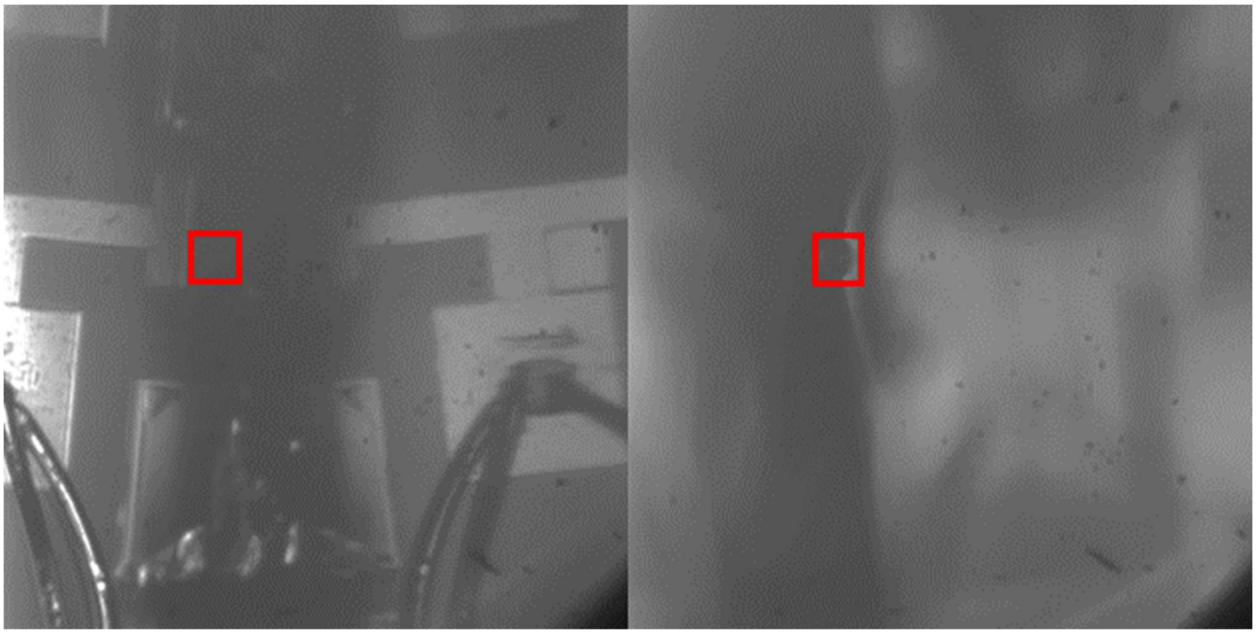

Figure 42: Alignment images for graphene device and SiO_2 sphere. On the right, the image for the receiver sphere is boxed in red. On the left, the same box is used under a different plane of focus to move the cleanest location of the emitter device directly below the receiver sphere.

4.3.4 Repeatability Considerations

Graphene samples were also checked for conductance between the backgate contact and source contact after the sweep, to rule out the possibility that the measured conductance may contain a confounding leakage factor.

All experiments are conducted after the vacuum pressure stabilizes at or below 2e-6 Torr and $\geq$ 2 hours after the temperature controllers for the vacuum chamber and bottom sample have been completed. Time between experiments is one hour minimum to allow the receiver to fully cool, following the lessons learned in Chapter 3.

4.4 Results and Analysis

The following results are consistent qualitatively with predictions, but high backgate voltages were found to be incompatible with the current setup, preventing significant signal switching at nearest distances Additional efforts were taken to ensure a relatively stiff and highly vertical probe to ideally permit higher switching voltages in future measurements. Considerations for future experiments are discussed further in 4.5.Fermi Level Dependence of Conductance

The graphene-mediated thermal conductance is dependent on both the distance and the Fermi level. There is a best Fermi level for each distance, which is not always the same, as discussed in reference [45] and shown in Figure 43 for the calculated heat flux on the distance range from 100 to 350 nm.

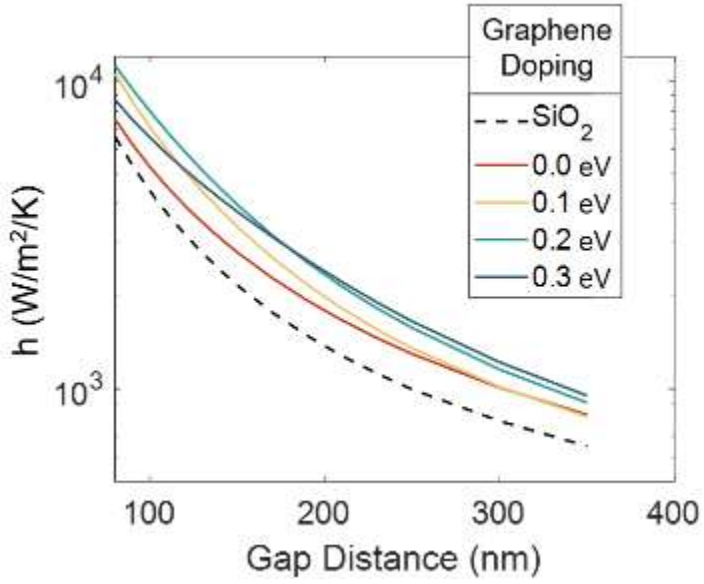

Figure 43: Heat flux for an SiO_2 plane to a G/300 nm SiO_2 plane
The best Fermi level at 100 nm is 0.2 eV, but it is 0.3 eV at 350 nm.
The relative positions of the others change as well.

For a single distance of 100nm, we can straightforwardly view the expected dependence of the heat flux on the Fermi level of graphene for the studied system, as shown in Figure 44. The electrical sweep showed us that the Fermi level at 0V gate bias is ~0.32 eV, which is close to the

peak on the decreasing side. Figure 44 also indicates a possible switching ratio at this distance of ~2.3 times from 0 to 0.5 eV as the Fermi level of the graphene sample..

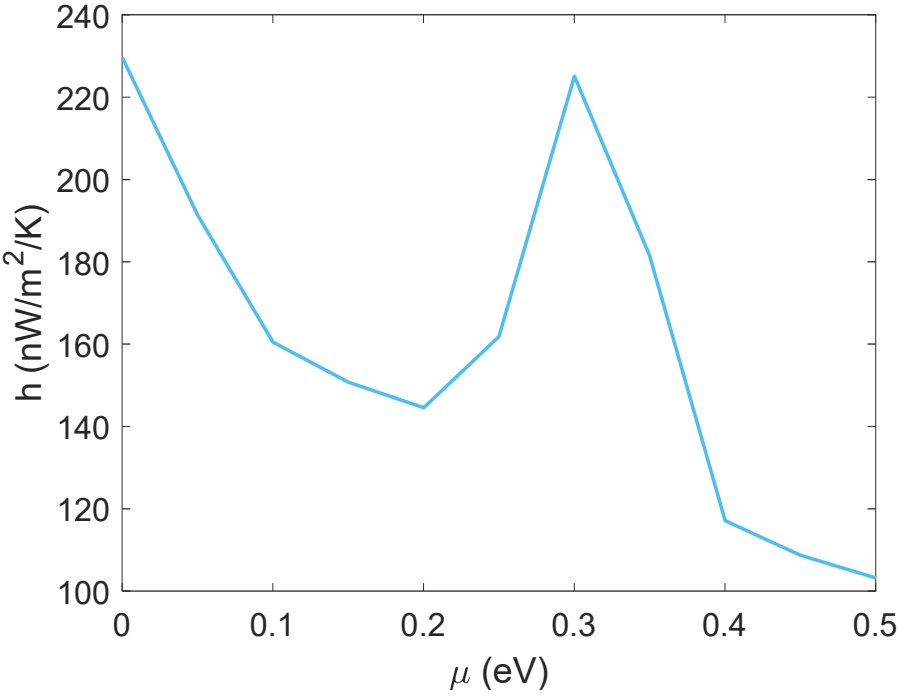

Figure 44: Predicted heat flux vs Fermi level in graphene-mediated SiO_2 system.

4.4.1 Single Backgate Voltage Change

We measured the SiO_2-graphene/SiO_2 NFRHT at a fixed distance estimated to be about 100 nm while changing the applied backgate voltage. We observed a noticeable shift in the NFRHT due to applied back gate voltage as shown in Figure 45.

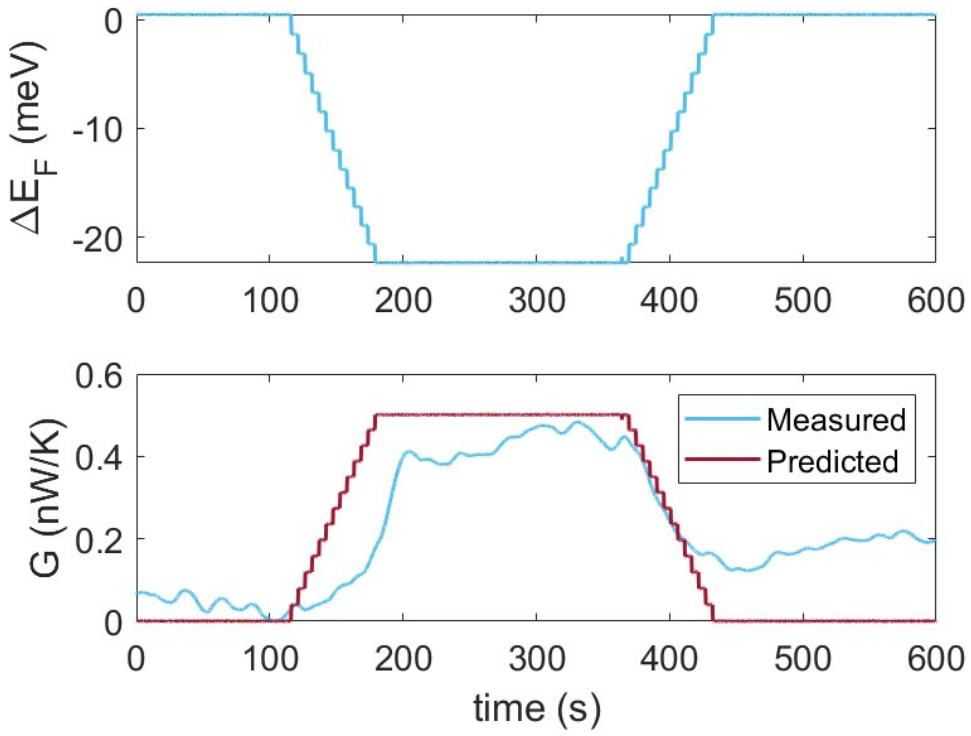

Figure 45: Electric field tuning of thermal capacitance with graphene. Top: Change in calculated Fermi level by backgate voltage. Bottom: Change in thermal conductance as measured and as anticipated.

Because the behavior shown in Figure 45 could be a greater capacitive force bending the probe tip towards the substrate, we also conducted a bipolar backgate change, as shown in Figure 46. In this case, the system exhibits a change in NFRHT only in one direction of applied backgate. This is promising for a phenomenon that is not just mechanical bending, as the capacitive force exhibited should be similar in either direction and we might expect to see an increase either way if this were the case. Because the thermal conductance has a peak when the Fermi level is 0.3 eV and the 0V applied bias corresponds to a Fermi level of ~0.32 eV, we anticipate that for small changes in the voltage bias, we can expect to see decreasing Fermi level lead to an increase in the thermal conductance, and vice versa. . It is likely that because the total heat transfer for 20 K heating of the emitter was still close to our resolution limit of 1 nW, that decreases in the thermal conductance were not able to be seen. However, we cannot eliminate

mechanical bending as a potential mechanism, as weobserved snap-in behavior for larger backgate voltages, as the devices suddenly displayed conductance-level heat transfer when higher back gate voltages were applied.

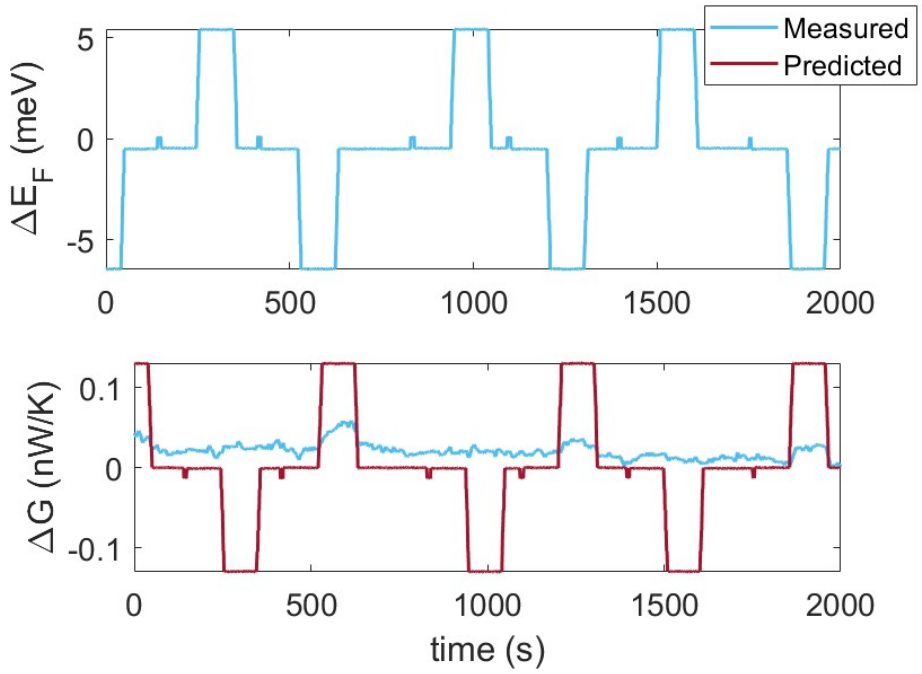

Figure 46: Variation in thermal signal under bipolar back gate switching. At a fixed vacuum gap distance estimated to be ~100nm, the SiO_2-Graphene/SiO_2/Si thermal conductance was measured while the backgate was changed by ±5 meV – larger changes resulted in premature snap-in. A significant and repeatable difference in the thermal voltage signal is noted only for decreasing Fermi level. This is promising for the ability to impact the heat transfer with graphene doping.

4.5 Conclusions and Future Work

These data are very promising for measurable signal change in graphene-mediated systems under even a small bias and a very small shift in the doping. We observe, at a ~100 nm gap distance between devices, a nanowatt-scale change in the NFRHT between a silicon dioxide sphere and a plane of graphene on a silicon dioxide thin film with a 20 K temperature differential, when the graphene's dielectric function is tuned electrostatically via backgate. A switching ratio of 230% is predicted for a device with a full range of back gate voltage available. However, the possibility still remains that the measured signal change is due to mechanical bending under the capacitive

force caused by the back gate voltage. A strategy is therefore proposed for an improved measurement with more conclusive results.

First, the earlier version of the probe used for the preliminary measurements, has since been replaced with a high-stiffness version, such as that used in the two-sphere measurements and described in 2.3.2. Second, the L-shaped holder for the probe was corrected from a rounded mount to a flat mount for the probe-sample body, to facilitate a 90° angle with the substrate. Third, the temperature differential of the measurements should be increased, such that the total difference in signal might more strongly be measured, 30 K is a safe temperature for the emitter setup as it exists now. Finally, should experiments still have difficulties, the thickness of the back gate can be reduced, so that the back gate control can be improved.

If the final strategy is taken, care should be taken that the thickness of the silicon dioxide is larger than the anticipated gap distance at which switching differences are anticipated to be measured. This is because the thickness of the SiO_2 must exceed the gap distance to respond as a bulk material, and the high predicted switching ratio for the graphene-mediated study depends on the high NFRHT yielded between bulk-like silicon dioxide samples.

4.6 Contributions

The results presented in this chapter were produced with collaboration from my colleagues. Z. Wang made the top holder and led sphere mounting. I fabricated the graphene device and bottom holder. J.W. Lim assisted me in troubleshooting experiments. K. Panda prototyped device holder configurations. Y. Luan fabricated the top probe. I conducted the experiments and PFA analysis. The work was conceived by E. Meyhofer and P. Reddy.

Chapter 5 Conclusions and Outlook

5.1 Conclusions

Several analytical and experimental studies have been conducted to explore the field of NFRHT studies for real-world applications. Analytical studies aim to answer important questions related to heat transfer between two significantly curved surfaces and arbitrary shapes, but without an experimental counterpart. Additionally, a knowledge gap exists for tunable graphene-mediated NFRHT, in that existing studies present a limited scope in terms of distances and doping levels measured. In this dissertation, a vertical sensing scheme was outlined which enabled new experiments. The first experimental demonstration of NFRHT between two spheres has been discussed, representing a significant step towards understanding varying geometries for radiative thermal studies.

Second, the preliminary data obtained from the graphene system is promising and suggests that further studies across a variety of distances and doping levels may lead to information that is useful in the developing field of thermal transistors. To expand the available knowledge on this material for applications in thermal rectification, a more thorough investigation of graphene as a tunable mediator of NFRHT between two silica bodies is ongoing.

5.2 Future Directions

5.2.1 NFRHT between Two Spheres

The successful theoretical prediction, comparing plate-plate and sphere-plate or sphere-sphere configuration experiments justifies further sphere-plane experiments for the testing of novel materials without parallelization needs. Such materials may include:

- Materials for thermal switching, ex: VO_2, graphene
- Thin-film layered materials

5.2.2 NFRHT Mediated by Graphene

This early data encourages future work in this line:

- Conducting experiments under stronger bias
- Mediating different materials with graphene
- Patterned graphene

To facilitate measurements at a stronger bias, a stiffer probe is in use, and additional caution has been taken to mount the probe perfectly vertically to avoid a bending-induced premature snap-in. A higher temperature differential of 30 K or higher is also expected to help in detection of a decrease in signal, which would confirm that the measured changes in NFRHT are not due to mechanical bending.

Theoretical predictions have indicated that graphene on a non-polar substrate such as silicon can facilitate heat transfer with a polar body, such as SiO_2[52]. Similarly, graphene can be used as one or two mediating layers to significantly enhance the NFRHT between two dissimilar polar materials[56]. This is promising for real-world systems in which one material is fixed and may not be ideal for heat transfer, potentially we can still engineer more efficient emission to a heat sink by coating non-ideal materials with graphene.

It should also be considered that interference effects prevent full sheets of graphene from meeting the whole possibility of NFRHT from plasmonic 2D materials. Instead, graphene should be patterned, such as into dipolar circles, to better approach the 2D plasmonic material bound in the near-field [107,108]. This change may allow a larger total peak heat transfer and therefore facilitate highly-efficient TPV devices as well as increasing the total power of switching when graphene is used.

Appendix: Dielectric Functions

This appendix contains calculated or tabulated dielectric functions reproduced for implementation in the theoretical predictions of NFRHT in this thesis.

A.1 Dielectric Function of Bulk Silicon (Si)

The dielectric function of lightly doped Si is compiled using data from literature sources[109]. The reconstructed real and imaginary parts of the dielectric function are shown in Figure 48.

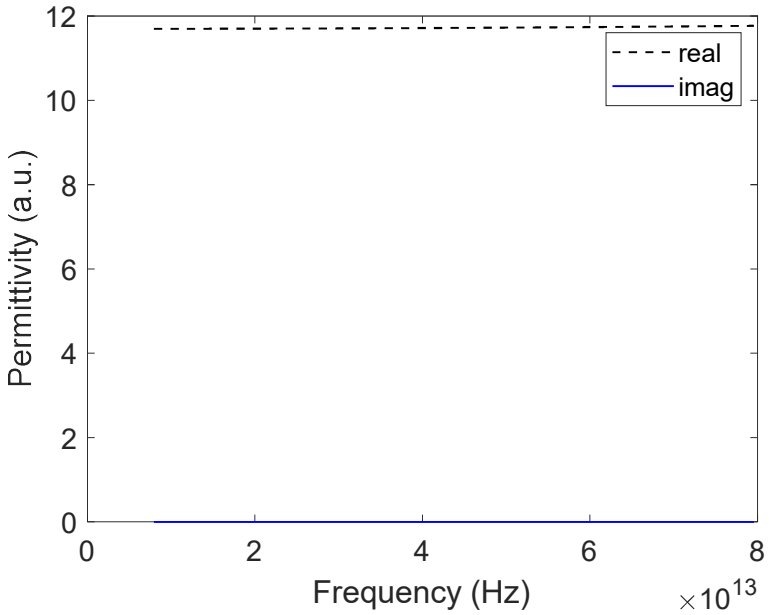

Figure 47: Real and imaginary components of the permittivity of Si.

A.2 Dielectric Function of Bulk Gold (Au)

The dielectric function of Au is compiled using data from literature sources[110]. The reconstructed real and imaginary parts of the dielectric function are shown in Figure 49.

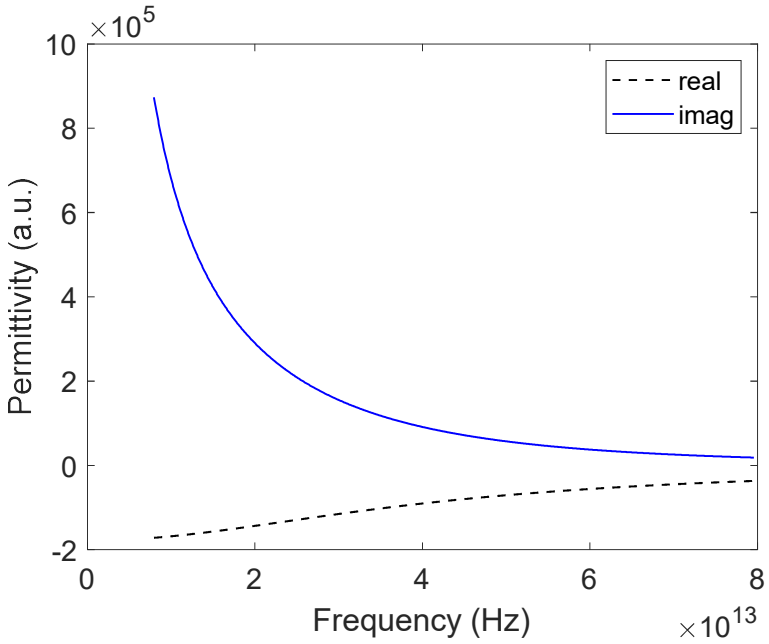

Figure 48: Real and imaginary components of the permittivity of Au.

A.3 Dielectric Function of Bulk Silicon Dioxide (SiO_2)

The dielectric function of SiO_2 is compiled using experimental data from literature sources[111,112].

The reconstructed real and imaginary parts of the dielectric function are shown in Figure 50.

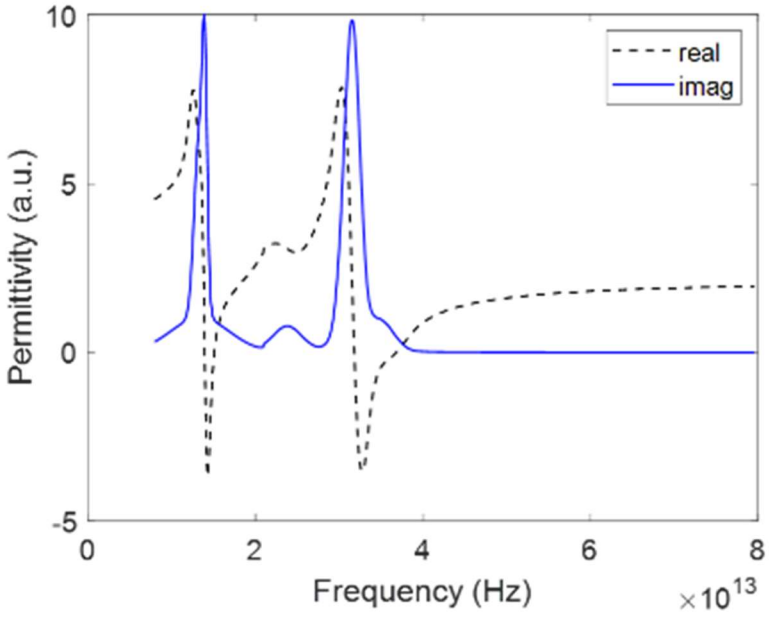

Figure 49: Real and imaginary components of the permittivity of SiO_2.

Bibliography

1. Kittel, A. Probing near-field thermal radiation. *Nat. Photonics* **3**, 492–494 (2009).
2. Jackson, J. D. *Classical Electrodynamics*. (John Wiley & Sons, 2021).
3. Bohm, D. *Quantum Theory*. (Courier Corporation, 2012).
4. Planck, M. K. E. L. Zur Theorie des Gesetzes der Energieverteilung im Normalspectrum. *Verhandl Dtsc Phys Ges* **2**, 237 (1900).
5. Planck, M. *The Theory of Heat Radiation*. (Blakiston, 1914).
6. Emslie, A. G. *Symposium on Thermal Radiation of Solids*. (Scientific and Technical Information Division, National Aeronautics and Space Administration, 1965).
7. Rytov, S. M. *THEORY OF ELECTRIC FLUCTUATIONS AND THERMAL RADIATION*. https://apps.dtic.mil/sti/citations/AD0226765 (1959).
8. Callen, H. B. & Welton, T. A. Irreversibility and Generalized Noise. *Phys. Rev.* **83**, 34–40 (1951).
9. Polder, D. & Van Hove, M. Theory of Radiative Heat Transfer between Closely Spaced Bodies. *Phys. Rev. B* **4**, 3303–3314 (1971).
10. Song, B., Fiorino, A., Meyhofer, E. & Reddy, P. Near-field radiative thermal transport: From theory to experiment. *AIP Adv.* **5**, 053503 (2015).
11. Song, B. *et al.* Enhancement of near-field radiative heat transfer using polar dielectric thin films. *Nat. Nanotechnol.* **10**, 253–258 (2015).

12. Perot, A. & Fabry, C. On the Application of Interference Phenomena to the Solution of Various Problems of Spectroscopy and Metrology. *Astrophys. J.* **9**, 87 (1899).
13. Biehs, S.-A. Thermal heat radiation, near-field energy density and near-field radiative heat transfer of coated materials. *Eur. Phys. J. B* **58**, 423–431 (2007).
14. Cuevas, J. C. & García-Vidal, F. J. Radiative Heat Transfer. *ACS Photonics* **5**, 3896–3915 (2018).
15. Chapuis, P.-O., Volz, S., Henkel, C., Joulain, K. & Greffet, J.-J. Effects of spatial dispersion in near-field radiative heat transfer between two parallel metallic surfaces. *Phys. Rev. B* **77**, 035431 (2008).
16. Laroche, M., Carminati, R. & Greffet, J.-J. Near-field thermophotovoltaic energy conversion. *J. Appl. Phys.* **100**, 063704 (2006).
17. Lucchesi, C. *et al.* Near-Field Thermophotovoltaic Conversion with High Electrical Power Density and Cell Efficiency above 14%. *Nano Lett.* **21**, 4524–4529 (2021).
18. Mittapally, R. *et al.* Near-field thermophotovoltaics for efficient heat to electricity conversion at high power density. *Nat. Commun.* **12**, 4364 (2021).
19. Mittapally, R., Majumder, A., Reddy, P. & Meyhofer, E. Near-Field Thermophotovoltaic Energy Conversion: Progress and Opportunities. *Phys. Rev. Appl.* **19**, 037002 (2023).
20. Basu, S. & Francoeur, M. Near-field radiative transfer based thermal rectification using doped silicon. *Appl. Phys. Lett.* **98**, 113106 (2011).
21. St-Gelais, R., Guha, B., Zhu, L., Fan, S. & Lipson, M. Demonstration of Strong Near-Field Radiative Heat Transfer between Integrated Nanostructures. *Nano Lett.* **14**, 6971–6975 (2014).
22. Li, M. *et al.* Electrically gated molecular thermal switch. *Science* **382**, 585–589 (2023).

23. Narayanaswamy, A. & Chen, G. Thermal near-field radiative transfer between two spheres. *Phys. Rev. B* **77**, 075125 (2008).

24. Sasihithlu, K. & Narayanaswamy, A. Proximity effects in radiative heat transfer. *Phys. Rev. B* **83**, 161406 (2011).

25. Rodriguez, A. W., Reid, M. T. H. & Johnson, S. G. Fluctuating-surface-current formulation of radiative heat transfer: Theory and applications. *Phys. Rev. B* **88**, 054305 (2013).

26. Rodriguez, A. W., Reid, M. T. H. & Johnson, S. G. Fluctuating-surface-current formulation of radiative heat transfer for arbitrary geometries. *Phys. Rev. B* **86**, 220302 (2012).

27. Biehs, S.-A. & Greffet, J.-J. Phys. Rev. B 81, 245414 (2010) - Near-field heat transfer between a nanoparticle and a rough surface. https://journals.aps.org/prb/abstract/10.1103/PhysRevB.81.245414 (2010).

28. Otey, C. & Fan, S. Numerically exact calculation of electromagnetic heat transfer between a dielectric sphere and plate. *Phys. Rev. B* **84**, 245431 (2011).

29. Messina, R., Ben-Abdallah, P., Guizal, B. & Antezza, M. Graphene-based amplification and tuning of near-field radiative heat transfer between dissimilar polar materials. *Phys. Rev. B* **96**, 045402 (2017).

30. Krüger, M., Bimonte, G., Emig, T. & Kardar, M. Trace formulas for nonequilibrium Casimir interactions, heat radiation, and heat transfer for arbitrary objects. *Phys. Rev. B* **86**, 115423 (2012).

31. Nguyen, K. L., Merchiers, O. & Chapuis, P.-O. Near-field radiative heat transfer in scanning thermal microscopy computed with the boundary element method. *J. Quant. Spectrosc. Radiat. Transf.* **202**, 154–167 (2017).

32. Narayanaswamy, A., Shen, S. & Chen, G. Near-field radiative heat transfer between a sphere and a substrate. *Phys. Rev. B* **78**, 115303 (2008).

33. Rousseau, E. *et al.* Radiative heat transfer at the nanoscale. *Nat. Photonics* **3**, 514–517 (2009).

34. Shen, S., Narayanaswamy, A. & Chen, G. Surface Phonon Polaritons Mediated Energy Transfer between Nanoscale Gaps. *Nano Lett.* **9**, 2909–2913 (2009).

35. van Zwol, P. J., Ranno, L. & Chevrier, J. Tuning Near Field Radiative Heat Flux through Surface Excitations with a Metal Insulator Transition. *Phys. Rev. Lett.* **108**, 234301 (2012).

36. Shi, J., Li, P., Liu, B. & Shen, S. Tuning near field radiation by doped silicon. *Appl. Phys. Lett.* **102**, 183114 (2013).

37. Xu, J. B., Läuger, K., Dransfeld, K. & Wilson, I. H. Thermal sensors for investigation of heat transfer in scanning probe microscopy. *Rev. Sci. Instrum.* **65**, 2262–2266 (1994).

38. Xu, J. -B., Läuger, K., Möller, R., Dransfeld, K. & Wilson, I. H. Heat transfer between two metallic surfaces at small distances. *J. Appl. Phys.* **76**, 7209–7216 (1994).

39. Müller-Hirsch, W., Kraft, A., Hirsch, M. T., Parisi, J. & Kittel, A. Heat transfer in ultrahigh vacuum scanning thermal microscopy. *J. Vac. Sci. Technol. A* **17**, 1205–1210 (1999).

40. Kittel, A. *et al.* Near-Field Heat Transfer in a Scanning Thermal Microscope. *Phys. Rev. Lett.* **95**, 224301 (2005).

41. Altfeder, I., Voevodin, A. A. & Roy, A. K. Vacuum Phonon Tunneling. *Phys. Rev. Lett.* **105**, 166101 (2010).

42. Worbes, L., Hellmann, D. & Kittel, A. Enhanced Near-Field Heat Flow of a Monolayer Dielectric Island. *Phys. Rev. Lett.* **110**, 134302 (2013).

43. Kim, K. *et al.* Radiative heat transfer in the extreme near field. *Nature* **528**, 387–391 (2015).

44. Cui, L. *et al.* Study of radiative heat transfer in Ångström- and nanometre-sized gaps. *Nat. Commun.* **8**, 14479 (2017).
45. Lang, Z. & Miller, O. Optimal Materials for Maximum Large-Area Near-Field Radiative Heat Transfer | ACS Photonics. *ACS Photonics* **7**, 3116–3129 (2020).
46. Mechanically Tunable Near-Field Radiative Heat Transfer between Monolayer Black Phosphorus Sheets | Langmuir. https://pubs.acs.org/doi/full/10.1021/acs.langmuir.0c02449.
47. T. Debu, D., Hasan Doha, M., H. Churchill, H. O. & B. Herzog, J. Gate voltage and doping effects on near-field radiation heat transfer in plasmonic heterogeneous pairs of graphene and black phosphorene. *RSC Adv.* **9**, 29173–29181 (2019).
48. Zhang, Y., Yi, H.-L. & Tan, H.-P. Near-Field Radiative Heat Transfer between Black Phosphorus Sheets via Anisotropic Surface Plasmon Polaritons. *ACS Photonics* **5**, 3739–3747 (2018).
49. Ge, L. *et al.* Magnetically tunable multiband near-field radiative heat transfer between two graphene sheets. *Phys. Rev. B* **100**, 035414 (2019).
50. Iqbal, N., Zhang, S., Choudhury, P. K., Jin, Y. & Ma, Y. Super-Planckian thermal radiation between 2D phononic hBN monolayers. *Int. J. Therm. Sci.* **172**, 107315 (2022).
51. Svetovoy, V. B., van Zwol, P. J. & Chevrier, J. Plasmon enhanced near-field radiative heat transfer for graphene covered dielectrics. *Phys. Rev. B* **85**, 155418 (2012).
52. Liang, W., Zheng, Z., Wang, L. & Yu, W. Electronically tunable near-field radiative heat transfer between doped silicon and graphene-covered silicon dioxide. *J. Quant. Spectrosc. Radiat. Transf.* **261**, 107485 (2021).
53. Landrieux, S., Ben-Abdallah, P. & Messina, R. Graphene-based enhancement of near-field radiative-heat-transfer rectification. *Appl. Phys. Lett.* **120**, 143502 (2022).

54. Yang, J. *et al.* Observing of the super-Planckian near-field thermal radiation between graphene sheets. *Nat. Commun.* **9**, 4033 (2018).

55. Liu, R. *et al.* Near-field radiative heat transfer in hyperbolic materials. *Int. J. Extreme Manuf.* **4**, 032002 (2022).

56. Zhang, W. B., Wang, B. X. & Zhao, C. Y. Active control and enhancement of near-field heat transfer between dissimilar materials by strong coupling effects. *Int. J. Heat Mass Transf.* **188**, 122588 (2022).

57. Thomas, N. H., Sherrott, M. C., Broulliet, J., Atwater, H. A. & Minnich, A. J. Electronic Modulation of Near-Field Radiative Transfer in Graphene Field Effect Heterostructures. *Nano Lett.* **19**, 3898–3904 (2019).

58. Shi, K., Chen, Z., Xu, X., Evans, J. & He, S. Optimized Colossal Near-Field Thermal Radiation Enabled by Manipulating Coupled Plasmon Polariton Geometry. *Adv. Mater.* **33**, 2106097 (2021).

59. Shi, K. *et al.* Near-Field Radiative Heat Transfer Modulation with an Ultrahigh Dynamic Range through Mode Mismatching. *Nano Lett.* **22**, 7753–7760 (2022).

60. Luo, F. *et al.* Graphene Thermal Emitter with Enhanced Joule Heating and Localized Light Emission in Air. *ACS Photonics* **6**, 2117–2125 (2019).

61. Lu, L. *et al.* Enhanced Near-Field Radiative Heat Transfer between Graphene/hBN Systems. *Small* **18**, 2108032 (2022).

62. Fiorino, A. *et al.* Nanogap near-field thermophotovoltaics. *Nat. Nanotechnol.* **13**, 806–811 (2018).

63. Lim, M., Lee, S. S. & Lee, B. J. Near-field thermal radiation between doped silicon plates at nanoscale gaps. *Phys. Rev. B* **91**, 195136 (2015).

64. Bernardi, M. P., Milovich, D. & Francoeur, M. Radiative heat transfer exceeding the blackbody limit between macroscale planar surfaces separated by a nanosize vacuum gap. *Nat. Commun.* **7**, 12900 (2016).

65. Klimchitskaya, G. L., Mohideen, U. & Mostepanenko, V. M. The Casimir force between real materials: Experiment and theory. *Rev. Mod. Phys.* **81**, 1827–1885 (2009).

66. Ganjeh, Y. *et al.* A platform to parallelize planar surfaces and control their spatial separation with nanometer resolution. *Rev. Sci. Instrum.* **83**, 105101 (2012).

67. Garrett, J. L., Somers, D. A. T. & Munday, J. N. Measurement of the Casimir Force between Two Spheres. *Phys. Rev. Lett.* **120**, 040401 (2018).

68. Reihani, A. *et al.* Quantifying the temperature of heated microdevices using scanning thermal probes. *Appl. Phys. Lett.* **118**, 163102 (2021).

69. Czapla, B. & Narayanaswamy, A. Near-field thermal radiative transfer between two coated spheres. *Phys. Rev. B* **96**, 125404 (2017).

70. Fernández-Hurtado, V., Fernández-Domínguez, A. I., Feist, J., García-Vidal, F. J. & Cuevas, J. C. Super-Planckian far-field radiative heat transfer. *Phys. Rev. B* **97**, 045408 (2018).

71. Bai, Y., Jiang, Y. & Liu, L. Enhanced near-field radiative heat transfer between a nanosphere and a hyperbolic metamaterial mediated by coupled surface phonon polaritons. *J. Quant. Spectrosc. Radiat. Transf.* **158**, 61–68 (2015).

72. Francoeur, M. & Mengüç, M. P. Role of fluctuational electrodynamics in near-field radiative heat transfer - ScienceDirect. https://www.sciencedirect.com/science/article/pii/S0022407307002427 (2007).

73. V. Derjaguin, B., I. Abrikosova, I. & M. Lifshitz, E. Direct measurement of molecular attraction between solids separated by a narrow gap. *Q. Rev. Chem. Soc.* **10**, 295–329 (1956).

74. Reid, M. T. H. & Johnson, S. G. Efficient Computation of Power, Force, and Torque in BEM Scattering Calculations. *IEEE Trans. Antennas Propag.* **63**, 3588–3598 (2015).

75. Rao, S., Wilton, D. & Glisson, A. Electromagnetic scattering by surfaces of arbitrary shape. *IEEE Trans. Antennas Propag.* **30**, 409–418 (1982).

76. Yan, S. *et al.* Surface Phonon Polariton-Mediated Near-Field Radiative Heat Transfer at Cryogenic Temperatures. *Phys. Rev. Lett.* **131**, 196302 (2023).

77. Thompson, D. Exploration of Radiative Thermal Transport at the Nanoscale Using High-Resolution Calorimetry. (2018).

78. Novoselov, K. S. *et al.* Electric Field Effect in Atomically Thin Carbon Films. *Science* **306**, 666–669 (2004).

79. McClure, J. W. Band Structure of Graphite and de Haas-van Alphen Effect. *Phys. Rev.* **108**, 612–618 (1957).

80. Wallace, P. R. The Band Theory of Graphite. *Phys. Rev.* **71**, 622–634 (1947).

81. Fradkin, E. Critical behavior of disordered degenerate semiconductors. I. Models, symmetries, and formalism. *Phys. Rev. B* **33**, 3257–3262 (1986).

82. Novoselov, K. S. *et al.* Two-dimensional gas of massless Dirac fermions in graphene. *Nature* **438**, 197–200 (2005).

83. Wehmeyer, G., Yabuki, T., Monachon, C., Wu, J. & Dames, C. Thermal diodes, regulators, and switches: Physical mechanisms and potential applications. *Appl. Phys. Rev.* **4**, 041304 (2017).

84. Basu, S., Lee, B. J. & Zhang, Z. M. Infrared Radiative Properties of Heavily Doped Silicon at Room Temperature. *J. Heat Transf.* **132**, (2009).

85. Ginn, J. C., Jarecki, R. L., Jr., Shaner, E. A. & Davids, P. S. Infrared plasmons on heavily-doped silicon. *J. Appl. Phys.* **110**, 043110 (2011).

86. Thompson, D., Zhu, L., Meyhofer, E. & Reddy, P. Nanoscale radiative thermal switching via multi-body effects. *Nat. Nanotechnol.* **15**, 99–104 (2020).

87. Liu, X. & Xuan, Y. Super-Planckian thermal radiation enabled by hyperbolic surface phonon polaritons. *Sci. China Technol. Sci.* **59**, 1680–1686 (2016).

88. Liu, X., Shen, J. & Xuan, Y. Near-Field Thermal Radiation of Nanopatterned Black Phosphorene Mediated by Topological Transitions of Phosphorene Plasmons. *Nanoscale Microscale Thermophys. Eng.* **23**, 188–199 (2019).

89. Shen, J., Liu, X. & Xuan, Y. Near-Field Thermal Radiation between Nanostructures of Natural Anisotropic Material. *Phys. Rev. Appl.* **10**, 034029 (2018).

90. Ott, A., Hu, Y., Wu, X.-H. & Biehs, S.-A. Radiative Thermal Switch Exploiting Hyperbolic Surface Phonon Polaritons. *Phys. Rev. Appl.* **15**, 064073 (2021).

91. Wu, X. & Fu, C. Near-field radiative modulator based on dissimilar hyperbolic materials with in-plane anisotropy. *Int. J. Heat Mass Transf.* **168**, 120908 (2021).

92. Biehs, S.-A., Rosa, F. S. S. & Ben-Abdallah, P. Modulation of near-field heat transfer between two gratings. *Appl. Phys. Lett.* **98**, 243102 (2011).

93. Fiorino, A. *et al.* A Thermal Diode Based on Nanoscale Thermal Radiation. *ACS Nano* **12**, 5774–5779 (2018).

94. Yang, Y., Basu, S. & Wang, L. Vacuum thermal switch made of phase transition materials considering thin film and substrate effects. *J. Quant. Spectrosc. Radiat. Transf.* **158**, 69–77 (2015).

95. Huang, Y., Boriskina, S. V. & Chen, G. Electrically tunable near-field radiative heat transfer via ferroelectric materials. *Appl. Phys. Lett.* **105**, 244102 (2014).

96. Ilic, O. *et al.* Active Radiative Thermal Switching with Graphene Plasmon Resonators. *ACS Nano* **12**, 2474–2481 (2018).

97. Yang, Y. & Wang, L. Electrically-controlled near-field radiative thermal modulator made of graphene-coated silicon carbide plates. *J. Quant. Spectrosc. Radiat. Transf.* **197**, 68–75 (2017).

98. He, M., Qi, H., Ren, Y., Zhao, Y. & Antezza, M. Active control of near-field radiative heat transfer by a graphene-gratings coating-twisting method. *Opt. Lett.* **45**, 2914–2917 (2020).

99. Chang, Y.-C., Liu, C.-H., Liu, C.-H., Zhong, Z. & Norris, T. B. Extracting the complex optical conductivity of mono- and bilayer graphene by ellipsometry. *Appl. Phys. Lett.* **104**, 261909 (2014).

100. Ilic, O. *et al.* Near-field thermal radiation transfer controlled by plasmons in graphene. *Phys. Rev. B* **85**, 155422 (2012).

101. Glassner, S. *et al.* Tuning Electroluminescence from a Plasmonic Cavity-Coupled Silicon Light Source. *Nano Lett.* **18**, 7230–7237 (2018).

102. González, A. L., Noguez, C., Beránek, J. & Barnard, A. S. Size, Shape, Stability, and Color of Plasmonic Silver Nanoparticles. *J. Phys. Chem. C* **118**, 9128–9136 (2014).

103. Low, T. & Avouris, P. Graphene Plasmonics for Terahertz to Mid-Infrared Applications. *ACS Nano* **8**, 1086–1101 (2014).

104. Huang, S., Song, C., Zhang, G. & Yan, H. Graphene plasmonics: physics and potential applications. *Nanophotonics* **6**, 1191–1204 (2017).

105. Frank, B. *et al.* Short-range surface plasmonics: Localized electron emission dynamics from a 60-nm spot on an atomically flat single-crystalline gold surface. *Sci. Adv.* **3**, e1700721 (2017).

106. Zang, W. *et al.* A Microcolumn DC Graphene Sensor for Rapid, Sensitive, and Universal Chemical Vapor Detection. *Nano Lett.* **21**, 10301–10308 (2021).

107. Miller, O. D. *et al.* Limits to the Optical Response of Graphene and Two-Dimensional Materials. *Nano Lett.* **17**, 5408–5415 (2017).

108. Ramirez, F. V., Shen, S. & McGaughey, A. J. H. Near-field radiative heat transfer in graphene plasmonic nanodisk dimers. *Phys. Rev. B* **96**, 165427 (2017).

109. Edwards, D. F. & Ochoa, E. Infrared refractive index of silicon. *Appl. Opt.* **19**, 4130–4131 (1980).

110. Ordal, M. A., Bell, R. J., Alexander, R. W., Long, L. L. & Querry, M. R. Optical properties of Au, Ni, and Pb at submillimeter wavelengths. *Appl. Opt.* **26**, 744–752 (1987).

111. Kischkat, J. *et al.* Mid-infrared optical properties of thin films of aluminum oxide, titanium dioxide, silicon dioxide, aluminum nitride, and silicon nitride. *Appl. Opt.* **51**, 6789–6798 (2012).

112. Kitamura, R., Pilon, L. & Jonasz, M. Optical constants of silica glass from extreme ultraviolet to far infrared at near room temperature. *Appl. Opt.* **46**, 8118–8133 (2007).